AFRL-AFOSR-UK-TR-2023-0065

Fundamental Non-Equilibrium Experiments for Hypersonic Flight

McGilvray, Matthew
THE UNIVERSITY OF OXFORD
UNIVERSITY OFFICES
OXFORD, ,
GB

06/20/2023
Final Technical Report

Air Force Research Laboratory
Air Force Office of Scientific Research
European Office of Aerospace Research and Development
Unit 4515 Box 14, APO AE 09421

REPORT DOCUMENTATION PAGE

PLEASE DO NOT RETURN YOUR FORM TO THE ABOVE ORGANIZATION.

1. REPORT DATE	2. REPORT TYPE	3. DATES COVERED	
20230620	Final	START DATE 20190701	END DATE 20221231

4. TITLE AND SUBTITLE
Fundamental Non-Equilibrium Experiments for Hypersonic Flight

5a. CONTRACT NUMBER	5b. GRANT NUMBER	5c. PROGRAM ELEMENT NUMBER
	FA9550-19-1-7020	
5d. PROJECT NUMBER	**5e. TASK NUMBER**	**5f. WORK UNIT NUMBER**

6. AUTHOR(S)
Matthew McGilvray

7. PERFORMING ORGANIZATION NAME(S) AND ADDRESS(ES)
THE UNIVERSITY OF OXFORD
UNIVERSITY OFFICES
OXFORD
GB

8. PERFORMING ORGANIZATION REPORT NUMBER

9. SPONSORING/MONITORING AGENCY NAME(S) AND ADDRESS(ES)	10. SPONSOR/MONITOR'S ACRONYM(S)	11. SPONSOR/MONITOR'S REPORT NUMBER(S)
EOARD UNIT 4515 APO AE 09421-4515	AFRL/AFOSR IOE	AFRL-AFOSR-UK-TR-2023-0065

12. DISTRIBUTION/AVAILABILITY STATEMENT
A Distribution Unlimited: PB Public Release

13. SUPPLEMENTARY NOTES

14. ABSTRACT
This report summarises the non-equilibrium and equilibrium spectral radiance data gathered in the Oxford T6 Stalker Tunnel while operating in Aluminium Shock Tube mode, from 1st July 2019 to 31st December 2022. Experiments were performed with two gas mixtures: synthetic air (20.78% O2 and 79.22% N2) and pure nitrogen. The data for each gas has been/ is to be presented at the Scitech Forum conference 2022 and 2024, respectively. The papers that have been submitted for which, form the main body of this report. Each paper includes a summary of conditions achieved, experimental and optical setups, and both spatially and spectrally resolved radiance profiles.

15. SUBJECT TERMS

16. SECURITY CLASSIFICATION OF:			17. LIMITATION OF ABSTRACT	18. NUMBER OF PAGES
a. REPORT U	b. ABSTRACT U	c. THIS PAGE U	SAR	65

19a. NAME OF RESPONSIBLE PERSON	19b. PHONE NUMBER *(Include area code)*
DOUGLAS SMITH	314 235 6013

Standard Form 298 (Rev.5/2020)
Prescribed by ANSI Std. Z39.18

Fundamental Non-Equilibrium Experiments for Hypersonic Flight

Alex Glenn

Dr Peter Collen

Prof. Matthew McGilvray

Grant no.: FA9550-19-1-7020

Period of Performance: 1st July 2019 - 31st December 2022

Report no.: OX-HYP-NEQ-003

Introduction

During a Low Earth Orbit return mission, an entry vehicle will be travelling at speeds between 5 and 8 km/s for a large portion of the trajectory. The bow shock ahead of the vehicle provides a mechanism to convert the kinetic energy of the vehicle to the internal energy of the gas species. This raises the energy states of the species, leading to dissociation and ionisation reactions, resulting in a partially ionised plasma sheath around the forebody of the vehicle. In air, the post-shock equilibrium temperature roughly scales with the speed of the vehicle, e.g. at 7 km/s it will be ~7000 K. Though the non-equilibrium region immediately behind the shock, where reactions are still occurring, can have considerably higher temperatures.

One way the excited species relax to a new equilibrium state is by radiation emission. Since only distinct energy states are allowed, the wavelengths of the emitted photons are predictable. Hence, this provides a means to identify species present in the post-shock gas via optical techniques. Though radiative heating itself is negligible compared to convective heating at these speeds, radiation measurements allow species number densities to be identified, as well as energy state distributions and reaction rates. These high temperature phenomena have important consequences for entry vehicle design:

1. Convective heating – strong function of species and temperatures present at the vehicle boundary layer edge
2. Communications blackout – due to radio frequency radiation absorption by free electrons
3. Aerothermodynamic coupling – the high temperature effects influence the pressure distribution and thus forces on vehicle surface
4. Observability – both from the vehicle and the ground, dependent on which wavelengths are emitted

This report summarises the non-equilibrium and equilibrium spectral radiance data gathered in the Oxford T6 Stalker Tunnel while operating in Aluminium Shock Tube mode, from 1st July 2019 to 31st December 2022. Experiments were performed with two gas mixtures: synthetic air (20.78% O_2 and 79.22% N_2) and pure nitrogen. The data for each gas has been/ is to be presented at the Scitech Forum conference 2022 and 2024, respectively. The papers that have been submitted for which, form the main body of this report. Each paper includes a summary of conditions achieved, experimental and optical setups, and both spatially and spectrally resolved radiance profiles.

Conditions nominally with a 1 bar post-shock pressure were selected, with shock speeds varying from ~5.5 to 7.2 km/s, relevant to Low Earth Orbit return trajectory speeds. The 1 bar post-shock was selected to allow comparisons of spectra against atmospheric plasma torch data. Such facilities are known to be in local thermodynamic equilibrium and thus a reliable source of equilibrium radiance, and additionally operate at temperatures comparable to the post-shock temperatures in these shock tube experiments. The relatively high pressure also improves signal-to-noise ratio, which decreases at lower speed conditions.

Spectrally and spatially resolved, calibrated absolute spectral radiance measurements are provided in two wavelength regions: UV/Vis (210 to 440 nm for air and 290 to 520 nm for nitrogen) and Vis/NIR (600-840 nm). The former predominantly measures transitions between

energy states of N2 and N2+ molecules, while the latter looks at atomic O and N lines, with a background signal from the N2 1st positive band. The 80 nm shift in the UV/Vis region between the two gas mixtures is because NO species radiate in this region. After confirming none of these species were present in the pure nitrogen data, and thus an adequate leak rate achieved, the wavelength region was thus shifted so that higher wavelengths could be observed.

The primary goal of these experiments was to obtain non-equilibrium radiance relevant to Low Earth Orbit return missions. This was achieved, along with the equilibrium radiance further behind the shock. Analysis of the effect shock speed has on non-equilibrium metrics has been plotted for synthetic air data. However, one of the primary findings with this dataset is the offset in equilibrium spectral radiance, between the experimental radiance measured and that predicted by CEA-NEQAIR simulations. This is observed in both gases and wavelength regions. Different methods to account for calibration artifacts such as stray light removal have been trialled, and can shift the experimental data to some degree, though it is not enough to account for the offset even in the most extreme case. The offset is thus believed to be a result of physical phenomena occurring during a shock tube experiment that are unaccounted for in simulations. Similar test conditions have been repeated in the Electric Arc Shock Tube at NASA Ames and the same offset was seen.

Any non-equilibrium analysis or simulations run to match experiment and extract rates is going to be influenced by this equilibrium offset. Thus, the primary focus has been to investigate its origin. Shock deceleration effects have been eliminated and the remaining theories include: contaminants on the shock tube walls; high temperature boundary layer effects; excess electron number densities (potentially caused by one of the two former points). Despite this, the data herein provides information to improve understanding of the shock layer thermochemical state at conditions relevant to Low Earth Orbit return.

Synthetic Air

This first paper details the synthetic air (20.78% O_2 and 79.22% N_2) experiments carried out for Low Earth Orbit return speeds from 5.5 to 7.2 km/s. Absolute radiance is plotted spatially and spectrally for both the equilibrium and non-equilibrium region. Simulations using CEA- and LASTA-NEQAIR are compared against equilibrium data, and POSHAX-NEQAIR predictions from a two-temperature model for the non-equilibrium region.

Contents

Experimental Non-Equilibrium Radiation Measurements for Low-Earth Orbit Return

A.B. Glenn*, P.L. Collen†, and M. McGilvray‡
Osney Thermofluids Institute, University of Oxford, United Kingdom

This paper reports on absolute radiation measurements performed in synthetic air (20.78% O_2, 79.22% N_2) shock-heated flows. Experiments were carried out in the Oxford T6 Stalker Tunnel in Aluminium Shock Tube mode. Data is presented for velocities ranging from 5.5-7.2 km/s at a nominal 1 bar post-shock pressure, in both UV/Vis and Vis/NIR spectral ranges. Simulations of the equilibrium radiance using NASA CEA and NEQAIR codes underpredict that obtained from the experimental data. An analysis using the newly developed LASTA code removes shock deceleration from consideration as a cause for this discrepancy. Non-equilibrium data is analysed in the form of spectral and absolute non-equilibrium metrics, and the effects of shock speed and post-shock pressure on the non-equilibrium radiance isolated. Finite-rate one-dimensional two-temperature simulations using POSHAX3 with Park 1993 rates are performed, which significantly underpredict the experimentally acquired data.

I. Introduction

The thermochemical state of the excited species in the shock-layer ahead of an entry vehicle has a profound influence on heat transfer and aerodynamics around the vehicle. Excitation and relaxation of any of the translational, rotational, vibrational and electronic energy modes can result in radiation absorption and emission respectively. Quantum mechanics dictates that each energy mode can only exist at discrete levels, thus allowing only a finite number of discrete wavelengths that can be emitted from each species during bound-bound interactions. In an optically thin radiating medium, where absorption is negligible, the intensity of radiation at a specific wavelength is directly related to the number density of the species it originates from. Emission spectroscopy techniques can therefore be used to measure the number densities of species present in such a flow. Corrections are possible to account for the optical thickness in a flow with significant absorption. The rates of the thermochemical processes can also be inferred by observing the spatial or temporal variation of radiation intensity at wavelengths relevant to the species of interest. Radiation emission studies therefore not only reveal details of the radiative heating environment, but are essential to understanding the thermochemical state of the shock layer gas and the rates of processes in the non-equilibrium region.

Shock layer radiation emission studies for low-Earth orbit (LEO) return missions have received less attention than those for high-speed Lunar and Mars return missions in recent years, due to the low contribution of radiation to overall heating. The Space Shuttle trajectory is exemplary of such LEO return conditions, generally not exceeding velocities above 8 km/s. Radiative heating increases with velocity in an exponential fashion, only becoming significant relative to stagnation point convective heating at speeds above 10 km/s in air [1]. LEO returns have therefore not promoted study from a radiative heating standpoint. However, as previously addressed, radiation studies allow indirect investigation of the thermochemical state of the flow, which can help to overcome a number of engineering challenges. Aerothermodynamics is one such example: the coupling between the aerodynamic and thermal processes, which cause the forces on the surfaces of a vehicle to be affected by the thermochemical state of the gas around it. Heat transfer is also a strong motivator: though radiative heating may be negligible at LEO return conditions, the convective heating is largely influenced by the thermochemical state at the edge of the boundary layer. Observability is another example, for which radiation in the visible and infrared wavelength ranges are directly of interest. Finally, the onset of communications blackout occurs around 4 km/s due to the initial ionisation of molecules, producing free electrons capable of absorbing radio frequency radiation. These issues mentioned motivate further study into the radiating shock layer of LEO return vehicles, to provide a more detailed understanding of species present. This is achieved in this work via radiation emission measurements. At the conditions of interest in this paper, the non-equilibrium radiance exceeds that of the equilibrium region. The analysis discussed herein thus focuses on this region.

*DPhil Candidate, Department of Engineering Science, Oxford Thermofluids Institute, University of Oxford
†Postdoctoral Researcher, Department of Engineering Science, Oxford Thermofluids Institute, University of Oxford
‡Associate Professor, Oxford Thermofluids Institute, Department of Engineering Science, University of Oxford

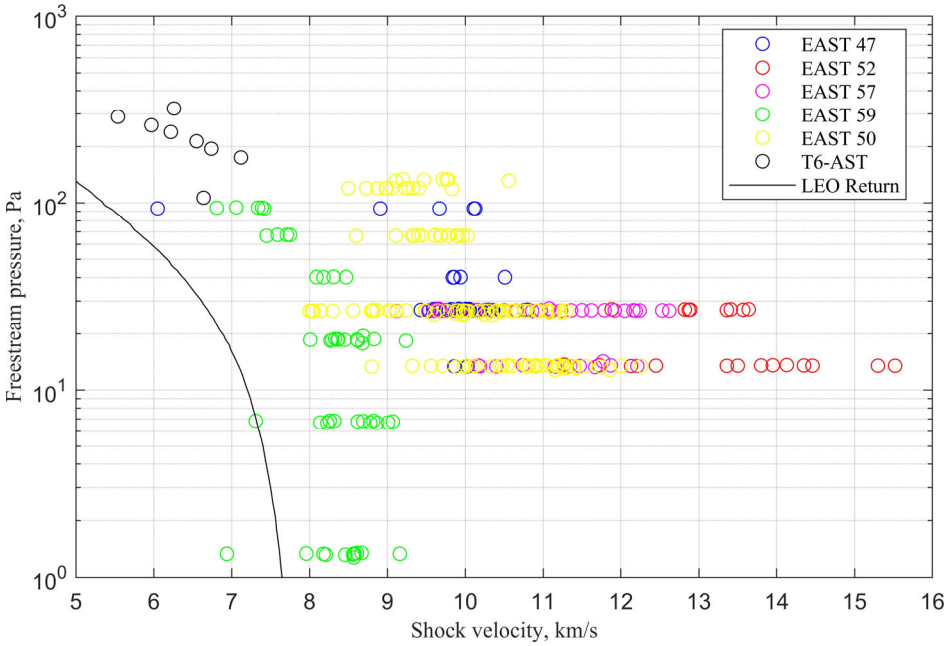

Fig. 1 T6 Aluminium Shock Tube test conditions studied in this paper compared against EAST test series in air and LEO return trajectory.

Non-equilibrium thermochemical relaxation phenomena and associated rate coefficients have been studied since the 1960s [2], though they are typically limited to high-velocity data and suffer from high uncertainties. Reducing uncertainties of non-equilibrium radiation has been identified as one of planet entry gas dynamics' highest priorities for the last 20 years [3]. Computational models capturing the non-equilibrium effects are still being developed and rely on experimental data for validation. In 2017, Cruden and Brandis [4] showed that current models don't predict non-equilibrium radiation accurately in air from 7–9 km/s due to the radiation being dominated by molecular non-equilibrium features, as opposed to atomic species which dominate at higher speeds [5–7]. Different aspects of the radiative and kinetic modelling are therefore being tested at these lower speed conditions. An extension of data to a wider combination of pressures and velocities will play an important role to improve the understanding of shock tube flows and their application to this low-speed regime.

This paper extends the Earth entry data available to lower velocities from 5.5 to 7.2 km/s, as shown in Fig. 1, plotted with a portion of a LEO return trajectory and air test series from the Electric Arc Shock Tube (EAST) [1] for reference. Most tests were undertaken at a post-shock pressure of 1 bar to enable future comparison to atmospheric plasma torch data. Tests were performed in the T6 Stalker Tunnel [8, 9] operating in Aluminium Shock Tube (AST) mode.

The experimental setup of the T6 facility in AST mode is described in Section II. Equilibrium data is compared to simulations using the NASA Chemical Equilibrium with Applications (CEA) in Section III. An analysis using the newly developed LASTA code is performed on two cases with different amounts of shock deceleration in Section IV. Finally, non-equilibrium data is analysed in Section V, and compared against predictions from a thermal and chemical relaxation solver. A number of different excitation models within the radiative modelling are compared for a nominal test case and the effects of shock velocity and post-shock pressure are assessed.

II. Experimental Setup

A. T6 Description

The T6 Stalker tunnel is a high enthalpy ground test facility at the University of Oxford, capable of reproducing atmospheric entry vehicle shock layer conditions. The facility has recently been described in detail by Collen et al. [8, 9]. Aluminium Shock Tube (AST) mode, illustrated in Fig. 2, was used for testing. Figure 3 is an image of the AST section, connected to the steel secondary driver on the left (upstream) and dump tank on the right (downstream).

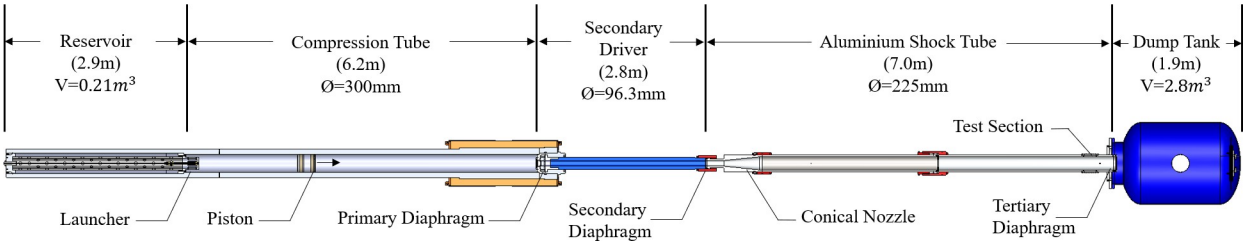

Fig. 2 Section view of T6 Stalker tunnel in Aluminium Shock Tube mode from above

Fig. 3 The T6 Aluminium Shock Tube, connected to the secondary driver (left) and dump tank (right)

The T6 facility utilises a free-piston driver, allowing for high shock speeds due to the generation of high sound speeds in the driver gas. The primary diaphragm initially separating the driver gas from the test gas is designed to rupture when a certain driver pressure is reached. This is controlled by diaphragm material, thickness and score depths. Reservoir air behind the piston is also filled to a set pressure, on the order of megapascals, specific to the tuned driver condition. To initiate a test, a vacuum pressure behind the piston is removed, allowing the high-pressure reservoir air to accelerate the piston through the compression tube, polytropically compressing the helium-argon mixture driver gas. The rapid increase in pressure causes the primary diaphragm to rupture, thus allowing expansion of the driver gas into the test gas, driving it downstream. Continued motion of the piston during this process delays expansion wave production by compressing the gas further.

Prior to this process, the AST section has been filled with a test gas to a pressure and composition relevant for the test case of interest. Upon primary diaphragm rupture, a normal shock wave is generated which progresses through this gas, compressing and accelerating it downstream. The flow between the normal shock and the contact surface (with the driver gas) is analogous to the stagnation streamline from the bow shock to the surface of an entry vehicle, travelling at the same speed as the shock and at an altitude with equivalent density as the initial shock tube fill. An optional secondary driver between the driver and AST can be filled with helium, by implementing a secondary diaphragm, to

reach faster shock speeds. In cases when it is not needed, there is no secondary diaphragm and the secondary driver is filled with the test gas. After the test gas passes the windows and enters the dump tank, a Pitot rake at the outlet of the tube is used to gather stagnation pressure and heat transfer data across the diameter of the test slug.

The design of the Aluminium Shock Tube lends itself to low-speed shock layer radiation studies. A conical nozzle section first increases the diameter from the nominal 96.3 mm secondary driver bore to 225 mm downstream. This provides a larger integration path-length for optically thin radiation, which is advantageous when capturing low-speed data due to the increased signal-to-noise ratio. In addition, the boundary layer formed around the tunnel circumference is relatively thinner compared to the tube diameter. This results in less shock deceleration and therefore longer test gas slugs [10], ideal for investigating the extent of non-equilibrium effects, as well as having a more uniform core flow. An optional tertiary diaphragm at the downstream end of the AST enables isolation of the test gas from the dump tank to reduce leak rates, though generally this was not needed during this experimental campaign. The aluminium construction is also advantageous as it reduces the presence of carbon contaminants in emission spectra. Finally, piezoelectric pressure transducers are located along the facility to measure the shock speed and static pressure.

Small doses of impurities in the test gas can have significant effects on the thermochemical reactions occurring in the test slug, thus causing the radiation captured from an experiment to deviate from the intended entry condition. Contaminants are therefore reduced by various means. Before filling the shock tube with the desired test gas, the initial atmospheric air is extracted via vacuum pumps. The tube is also flushed with the test gas multiple times to minimise the presence of remaining impurities. The ultimate pressure to achieve sufficient purity is dependent on the condition to be tested. In the synthetic air cases studied here, the fill pressures are relatively high and of similar composition to the real air evacuated, which further reduces uncertainties. For the data presented here, ultimate pressures of less than 1 Pa were achieved after flushing with the test gas, and leak rates less than 1 mPa s^{-1}. This was acceptable to avoid noticeable contamination in the majority of spectra for the test cases shown in this paper, with fill pressures all in excess of 100 Pa. Based on this ultimate pressure, leak rate and fill cycling, impurity percentages are estimated to be on the order of less than 1×10^{-7}% by volume. In addition to these attempts to reduce contaminants, the shock tube walls were cleaned with acetone before every test to remove traces of carbon from previous tests. In cases where contaminants are present, typically in the tail end of the equilibrium region, spectra have been averaged over regions which avoid their influence.

B. Test Conditions

The synthetic air test gas composition used for all tests was 20.78% O_2 and 79.22% N_2 by volume. A summary of the achieved conditions is provided in Table 1, data from which is plotted in Fig. 4. For each shot, a shock profile of the shock speed variation along the length of the tube is derived and uncertainties calculated following the method of James et al. [11]. The shock profiles for each test case are shown in Fig. 5. The first 3m are along the secondary driver, followed by the conical nozzle region, leading to the 225 mm diameter AST region which begins at 3.8m. The penultimate point on the trajectory is the velocity of the shock at the AST window. The measured post-shock pressures are determined from the pressure reading of the last shock timing station the shock passes at the window before the spatially and spectrally resolved image is taken.

Table 1 Summary of synthetic air conditions achieved in T6 Stalker tunnel. The shock speed that processed the test gas in the equilibrium and non-equilibrium regions at the time of emission spectroscopy camera gating are quoted separately.

Shot no.	P_{fill} (Pa)	$v_{Equilib}$ (km/s)	$v_{Non\text{-}equilib}$ (km/s)	$P_{2,Meas}$ (kPa)	$P_{2,CEA}$ (kPa)	$T_{2,CEA}$ (K)
195	290.0	5.66	5.54	99	99.7	6140
201	261.2	5.99	5.97	105	101.0	6346
194	240.0	6.26	6.22	98	101.6	6500
198	213.9	6.58	6.55	103	100.4	6666
196	195.0	6.87	6.74	100	100.0	6813
220	175.0	7.21	7.12	101	99.0	6983
207	106.7	6.64	6.64	50	51.1	6480
219	321.3	6.37	6.26	147	140.8	6663

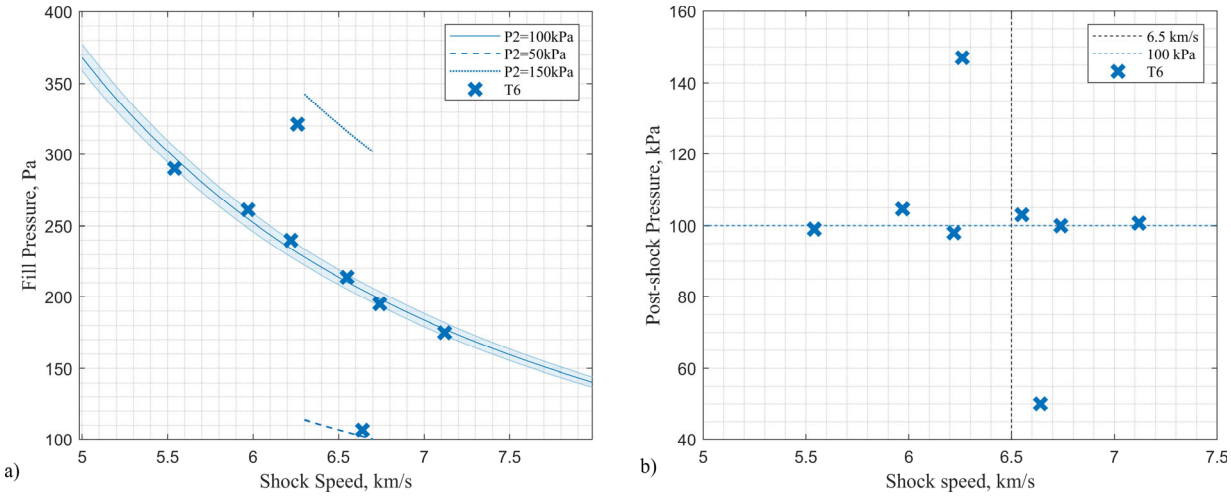

Fig. 4 Plots to illustrate synthetic air test conditions achieved: a) fill pressures used are compared to the theoretical values required to give a post-shock pressure of 1 bar for given shock speeds, shaded region indicates ±2.5 kPa; b) Post-shock pressure measured against shock speed.

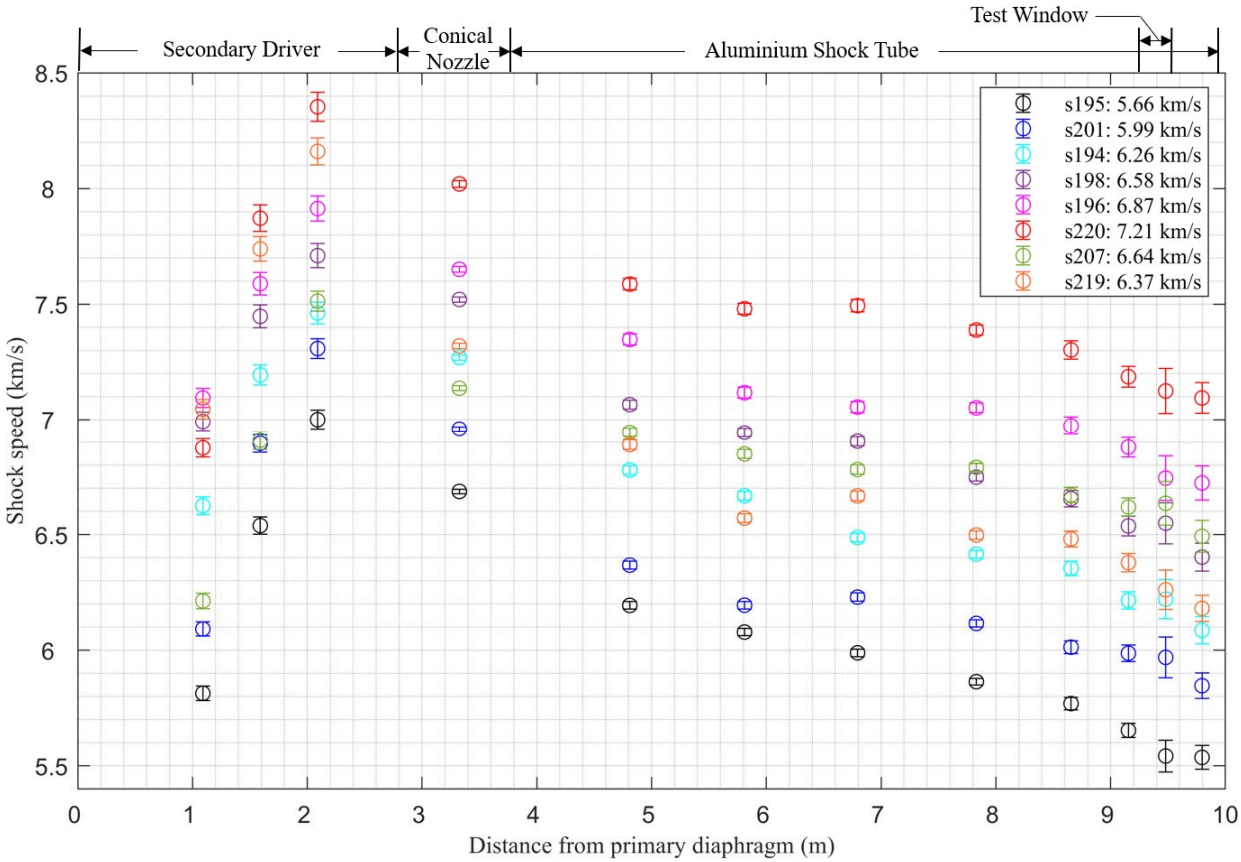

Fig. 5 Shock profile summary for the T6 AST synthetic air cases studied in this paper.

C. Optical Emission Spectroscopy (OES)

Primary analysis of the shocked gas is performed in the downstream section at the windows via two optical emission spectroscopy (OES) setups, as illustrated in Fig. 6. Radiation emitted from the test gas escapes through two 200 mm long, diametrically opposite windows along the tube axis. These are located 9.3 m from the primary diaphragm. Shock timing stations in this section are more closely spaced to provide higher resolution velocity measurement. Both windows have their own optical path and spectrometer, each with a designated wavelength region. For the synthetic air tests discussed here, a "blue side" is used to capture ultraviolet/visible wavelengths from 210 to 440 nm, and a "red side" for visible/near infrared from 600 to 840nm. The de-magnification factor of the red optical set up was 11.4. The blue side originally de-magnified by a factor of 25 but was then modified (due to a camera change part way through the campaign) to a factor of 20. Radiation along the length of the window is focused on the spectrometer slit; it is then spectrally separated by a diffraction grating while retaining its spatial profile along the tube axis. The wavelength dispersed image then falls on the camera sensor at the spectrometer outlet to finally capture the spatially and spectrally resolved image. Exposure times of 1μs or less are used to minimise smearing due to shock motion; this is especially important to analyse the transitory non-equilibrium region. On the red side, a Princeton Instruments Isoplane-320 spectrometer and Andor Intensified sCMOS camera were used, in a similar setup previously described by Collen et al. [12]. The blue side shown in Fig. 7 used a McPherson 218 0.3 m spectrometer and Princeton Instruments PIMAX:2 camera. An Andor iStar sCMOS 18U-E3 camera was also later used. Low resolution gratings, of 180 G/mm and 150 G/mm for the blue and red side respectively, were employed to provide access to broader wavelength ranges.

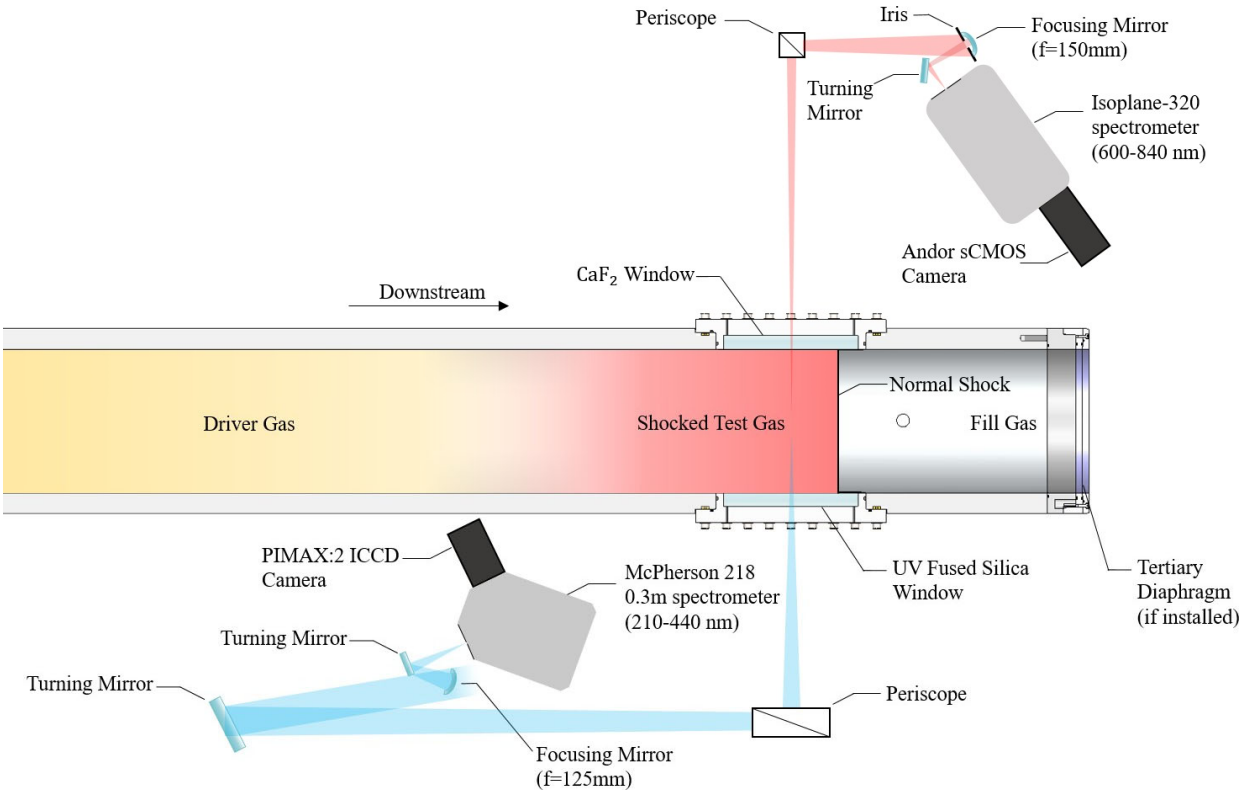

Fig. 6 The red (upper) and blue (lower) optical emission spectroscopy systems. Not to scale.

Calibrations were performed using a uniformly radiating integrating sphere, to produce a full field calibration at wavelengths above 300 nm for both the red and blue optical paths. In addition, a deuterium lamp is used to calibrate the blue side wavelengths below 300 nm. Calibrations were performed before every test. The procedure to calibrate shot data into units of spectral radiance has been described in detail by Collen [9] and is largely based on the methodology used at the Electirc Arc Shock Tube facility, as described by Cruden [1].

Fig. 7 Photo of the "blue side" optical setup to capture ultraviolet/visible radiation. An example image of the raw spatially and spectrally resolved data can be seen on the computer screen.

III. Equilibrium Data Validation

Radiative data from T6 AST experiments is obtained in the format of absolute radiance as a function of wavelength and position, as shown in Fig. 8 for an example in the Vis/NIR region. The vertical cross-section shows the radiance profile at a given wavelength. Data is integrated across the desired wavelength region to view the non-equilibrium peak at the shock front and relaxation to the subsequent equilibrium plateau. The horizontal cross-section gives spectral radiance at a given location. These are typically averaged over an appropriate portion of the equilibrium region to improve signal-to-noise ratio, while avoiding contaminated portions.

The equilibrium spectra and radiance profiles for shot 198 are displayed in Fig. 9, a condition with 6.55 km/s shock speed and 1 bar post shock pressure, accompanied by CEA-NEQAIR simulation results for comparison. The rest of the equilibrium data set for the remaining test cases is included in Appendix A. The simulations were run at the tunnel fill pressure and average shock speed from the three measurements before the shock reaches the window, as indicated in Fig. 5 and Table 1. This average speed is representative of the shock when it processed the gas that is in the equilibrium region at the time of OES camera gating. NEQAIR spectra have been convolved using the experimentally measured instrument line shapes (ILS) following the approach of Cruden [1].

It is clear that for both wavelength regions, in all test cases, the radiance from the experimental data exceeds that of the CEA-NEQAIR simulations. It is tempting to think this difference can be accounted for by subtracting a constant level of continuum background spectral radiance from the experimental data, to match CEA-NEQAIR predictions. If successful this would suggest the disagreement could be a result of excess electrons in the experiment due to shock deceleration or errors in the background subtraction method during data calibration. This method was trialled and though it does bring the baseline level radiation from the N_2 first positive band into close agreement, the height of the atomic peaks do not agree except for one or two fortuitous cases, suggesting excessive background emission in the core flow is not the issue. The study conducted in section IV also supports the conclusion that an excess of electrons from shock deceleration is not the cause of the increased radiation seen in the experiment. This is in agreement with the fact the shock profiles show relatively little deceleration and the radiance profiles generally have flat equilibrium plateaus, except where contaminants are present.

One possibility for the difference between experimental and simulated data is radiation originating from the boundary layer. When imaging the shock passing through the shock tube, the path length across the entire tunnel diameter is

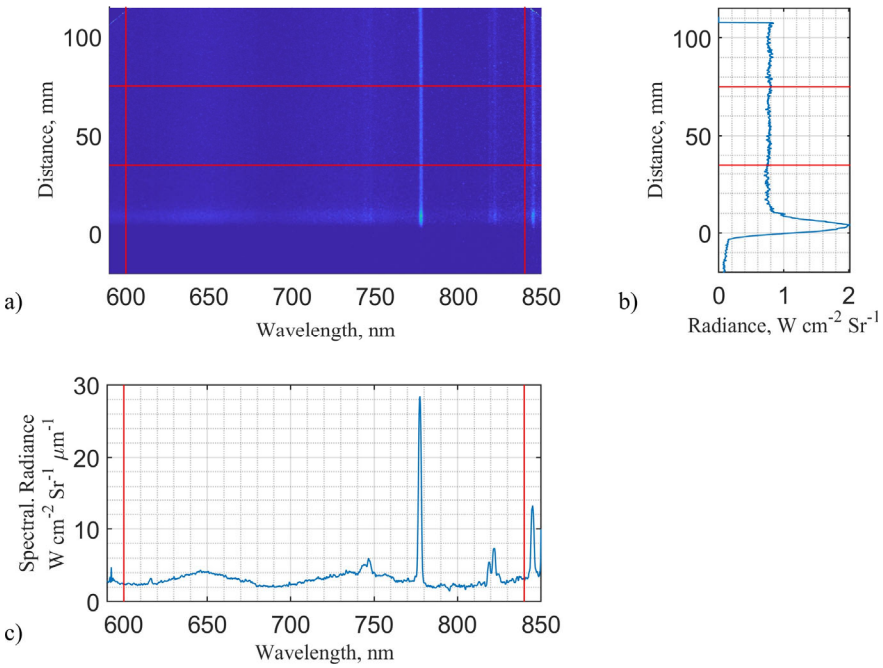

Fig. 8 Sample data set for Vis/NIR region, obtained in T6 facility from shot 198, 6.55 km/s, 103 kPa post-shock pressure. a) Absolute radiance as a function of position and wavelength is integrated between the vertical lines to obtain b) the radiance profile, while averaging between horizontal lines gives c) the equilibrium spectrum.

integrated, thus any radiation emanating from the boundary layer will be included in the analysed data. Viscous effects in the boundary layer may lead to higher temperatures, generating increased electron number densities and thus augmented continuum radiation. However, for the test cases considered here the boundary layer thickness is less than 1 mm in the equilibrium region of the test slug, thus contributing to less than 1% of the integration path length. Additionally, despite the regular cleaning of the internal tunnel walls, it is still likely that remnants on the surface will radiate when exposed to the high temperatures in the boundary layer or core flow.

Another possible source is the highly reflective aluminium tunnel walls. Radiation from the equilibrium region should be fairly constant and therefore reduce the effect of reflections, but the more intensely radiating non-equilibrium region could emit radiation which is subsequently reflected and superimposed on the equilibrium section of the flow. Additionally, stray light in the spectrometer could be contributing to the high radiation levels witnessed, though steps are taken at multiple points during the calibration procedure to rectify this effect via a "pedestal removal" technique [1]. Finally, radiative modelling errors within NEQAIR could be contributing to the observed discrepancies. These are low-speed conditions with significant radiation from molecular bands and therefore tests different aspects of the NEQAIR radiation modelling, compared to higher speed cases which are more dominated by atomic spectral lines.

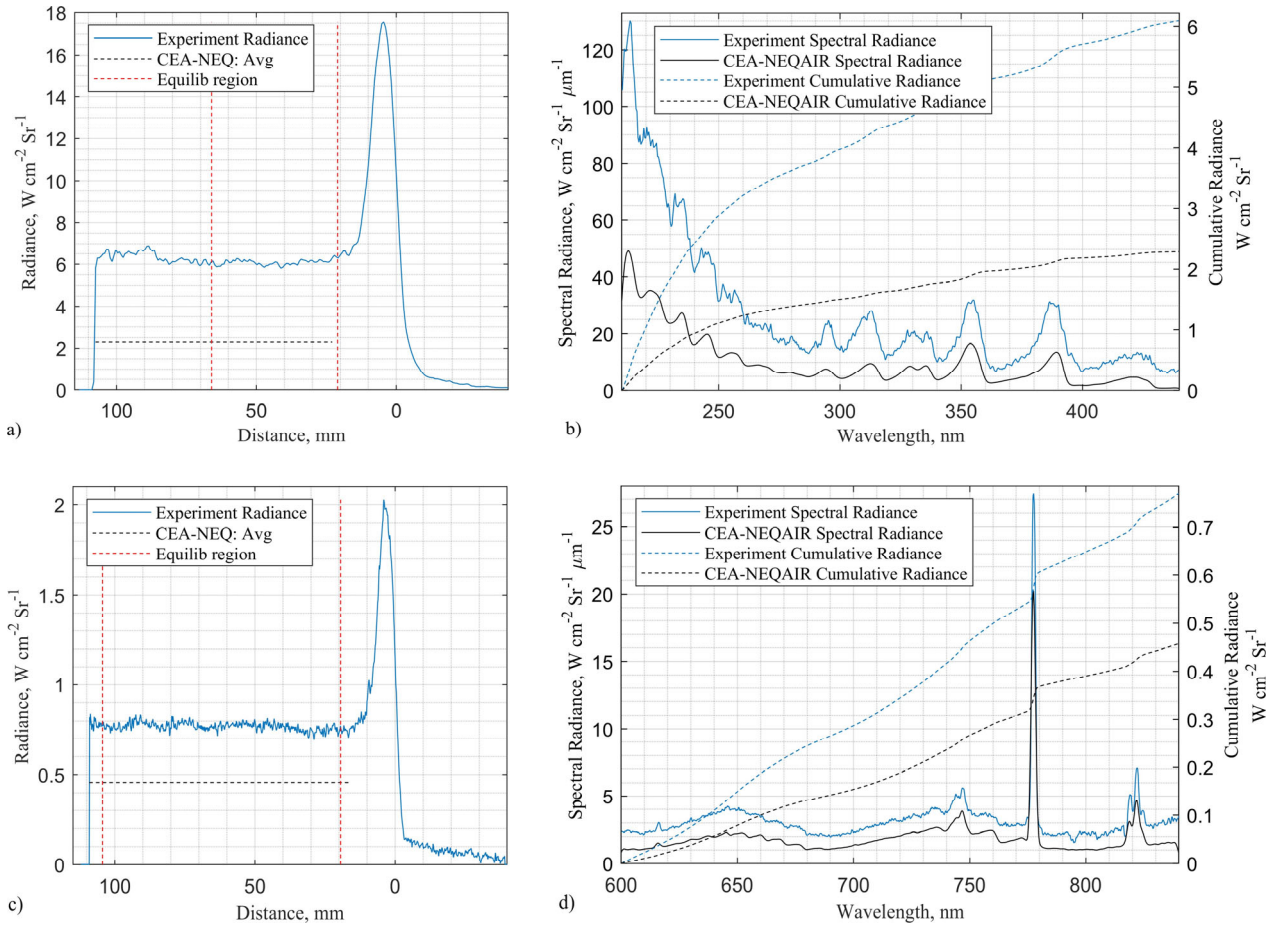

Fig. 9 Data summary for s198 at 6.55 km/s, 103 kPa post-shock pressure compared to CEA-NEQAIR simulations: a) radiance profile and b) equilibrium spectra for 210-440 nm; c) radiance profile and d) equilibrium spectra for 600-840 nm.

IV. LASTA Analysis

It has been demonstrated in the works of Satchell et al. [13–16] and Collen [9] that variations in shock speed down the tube and boundary layer growth cause variations in the test gas, which should be considered when analysing radiative data from shock tube experiments. A quasi one-dimensional Lagrange Shock Tube Analysys (LASTA) code has been developed at the University of Oxford to predict the variations in the test gas by discretising the test slug into a number of slices. The distance-time data of a given shock trajectory, along with test gas properties, fill pressure and tunnel dimensions are fed into the LASTA code to predict the compression and expansion waves required to induce the measured shock profile. The influence of those pressure waves on the thermochemical properties of each gas slice are calculated, providing a means to account for test-to-test variation in simulations by reconstructing the test slug of a given experiment.

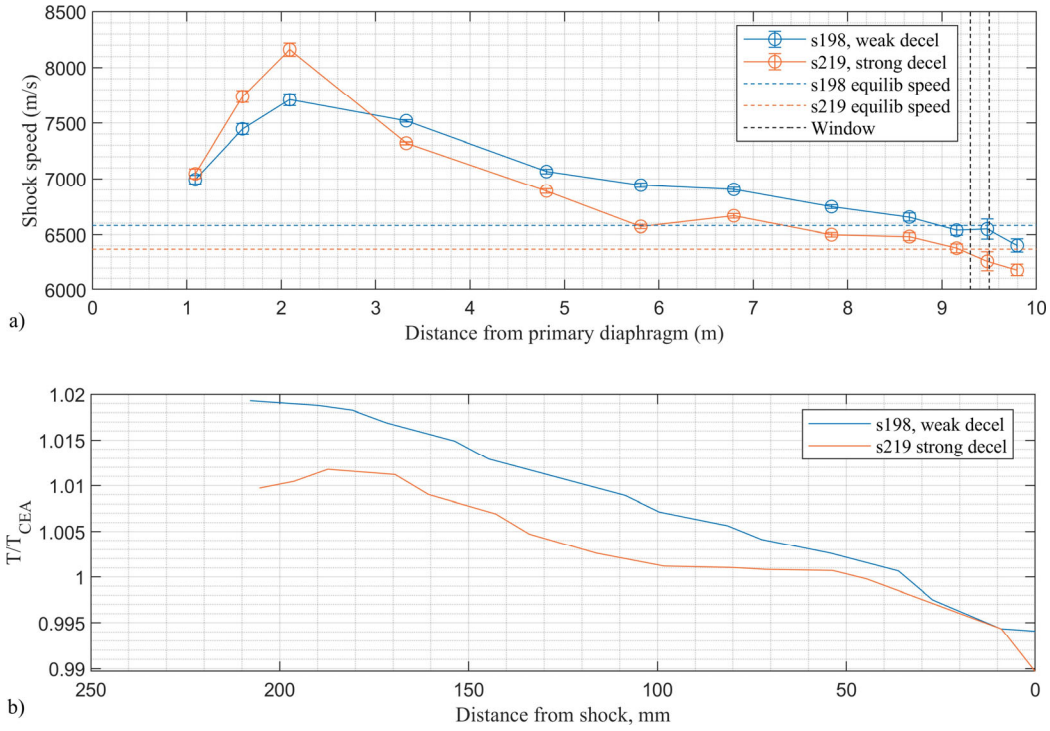

Fig. 10 Comparison of a) shock profiles and b) LASTA calculated temperatures normalised by CEA values through each test slug for two test cases with different amounts of shock deceleration.

To demonstrate the use of LASTA, two test cases are considered with different amounts of shock deceleration. The case with less shock deceleration is shot 198, which is compared to shot 219, having the greatest deceleration of all the test cases considered in this paper. The shock profiles are plotted in Fig. 10 a) with velocities used for the equilibrium CEA-NEQAIR simulations shown for reference. LASTA is able to calculate the properties of the core flow region in each slice. Figure 10 b) compares the temperatures calculated through the test slug of the two cases, each having been normalised by the equilibrium temperature calculated from CEA. Neither case significantly exceeds that of the equilibrium value calculated, with notable portions at the start of each test slug with temperatures less than the equilibrium values used, particularly for the case with more deceleration. This minor deviation from equilibrium through the test slug is likely due to the relatively small amounts of deceleration seen in each, in comparison to that typically seen for high-speed test cases.

The number densities of an 11-species model from the LASTA analysis were fed into NEQAIR to predict the radiance profiles of the two test cases. As can be seen in Fig. 11 and Fig. 12, the LASTA predictions are in very close agreement with that from CEA, with only very small gradients seen in the equilibrium region. LASTA only considers equilibrium conditions and so does not capture the non-equilibrium rise at the shock front. The close agreement between

the CEA and LASTA shock profiles eliminates excess electrons from shock deceleration as a potential cause of the increased level of background continuum radiation seen in the experimental data. This leaves reflections, boundary layer emission, background subtraction methodology during calibration and NEQAIR radiative modelling as potential sources of the discrepancy.

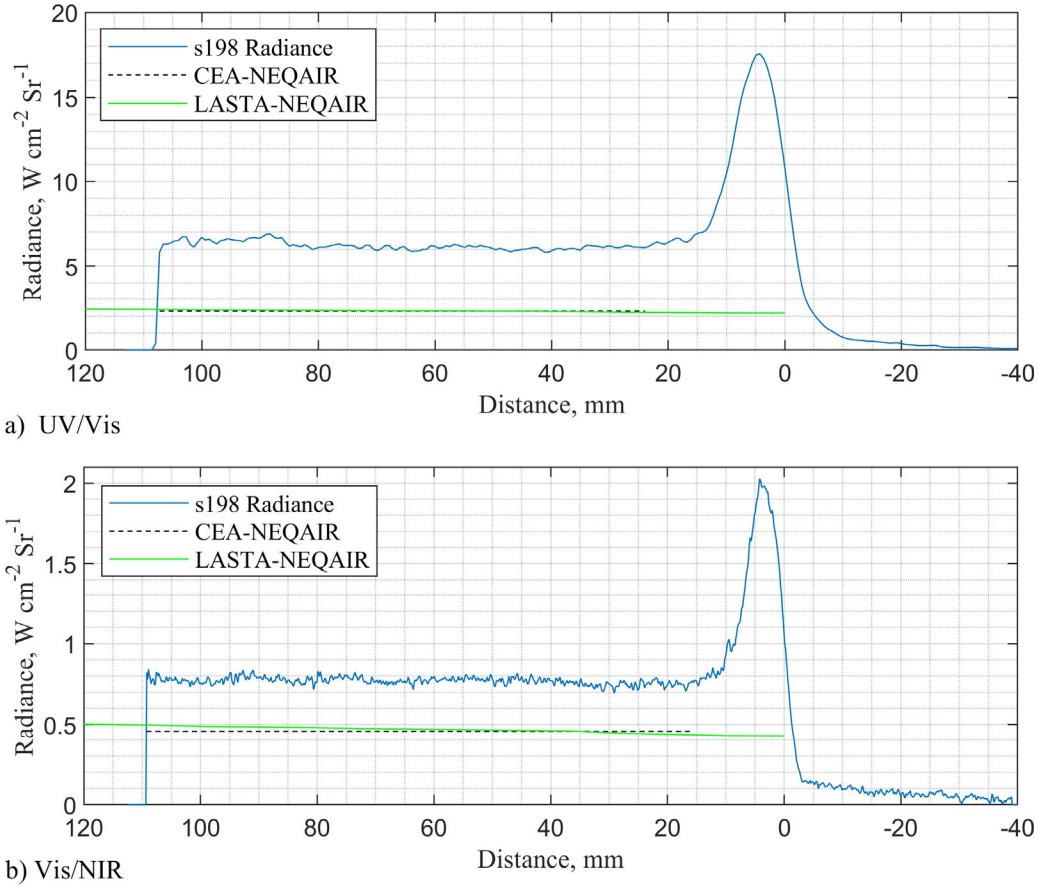

Fig. 11 Radiance profile comparisons between experiment, CEA, and LASTA for test case 198, for the a) UV/Vis (210-440 nm) and b) Vis/NIR (600-840 nm) region.

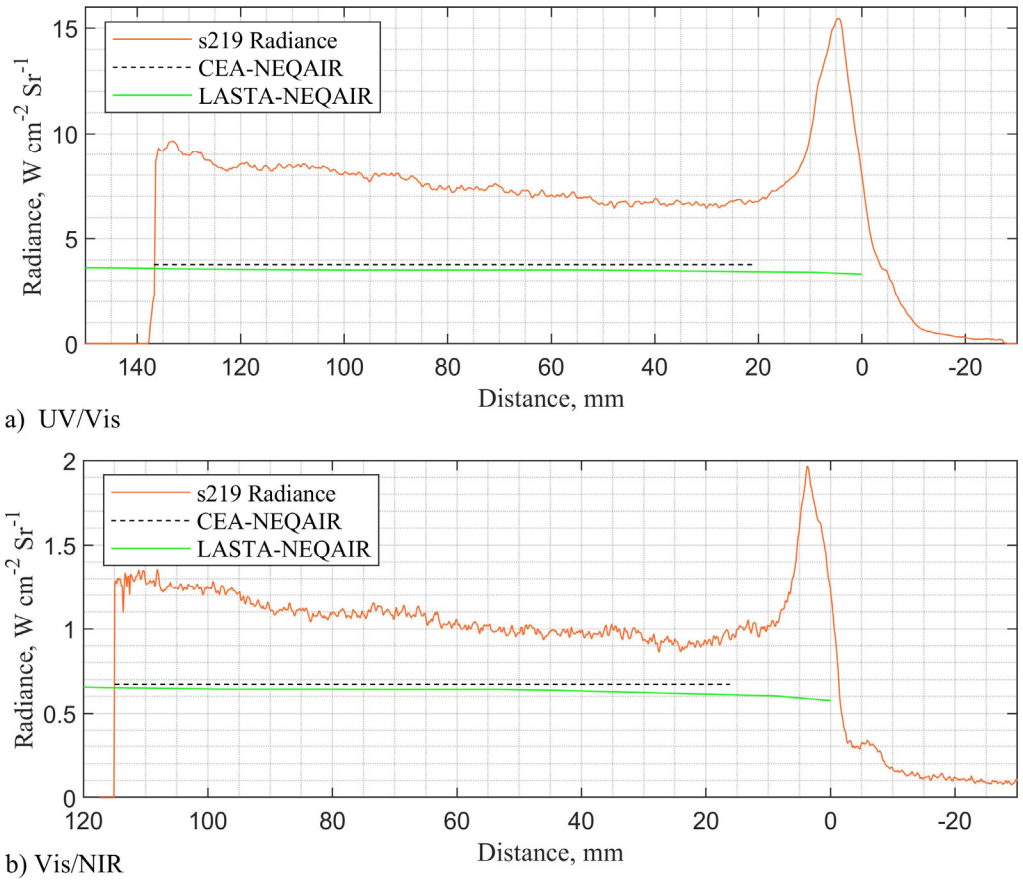

Fig. 12 Radiance profile comparisons between experiment, CEA, and LASTA for test case 219, for the a) UV/Vis (210-440 nm) and b) Vis/NIR (600-840 nm) region.

V. Non-Equilibrium Analysis

A. Modelling Process

To simulate the non-equilibrium region of the given test cases, a finite-rate one-dimensional thermal and chemical relaxation solver (POSHAX3) [17], developed at the University of Queensland, with an 11-species two-temperature air model with Park 1993 [2] reaction rates is used. The inputs required are shock speed, initial temperature, pressure and composition, in addition to the selection of appropriate chemical reaction and energy exchange rates. The shock speed at the window is used as the input for these simulations since that is the closest reading available to the speed of the shock when it processed the test gas in the non-equilibrium region at the time of OES camera gating. Results from the POSHAX simulations are fed into the NASA NEQAIR code to predict the corresponding radiance profiles for each wavelength region. The ILS and Spatial Resolution Functions (SRF), measured during the wavelength and spatial calibrations respectively, are convolved into the NEQAIR simulations to account for the broadening mechanisms imposed on the experimental data, enabling a like-for-like comparison between the two.

An example comparison between the experimentally measured and POSHAX3-NEQAIR radiance profiles is given in Fig. 13 for test 198. It is encouraging to see that the equilibrium plateaus from the POSHAX3 simulations overlie with the CEA simulations also run with the shock speed at the window, suggesting the final thermochemical state arrived at by POSHAX3 is correct. However, it is evident that the result from NEQAIR simulations underpredicts the experimentally measured radiance profiles, especially in the UV/Vis region. Hence, the species predicted in the non-equilibrium region by the Park 93 two-temperature model do not agree with the profile captured in the experiment. Future works will extend this by implementing other kinetic and radiative models.

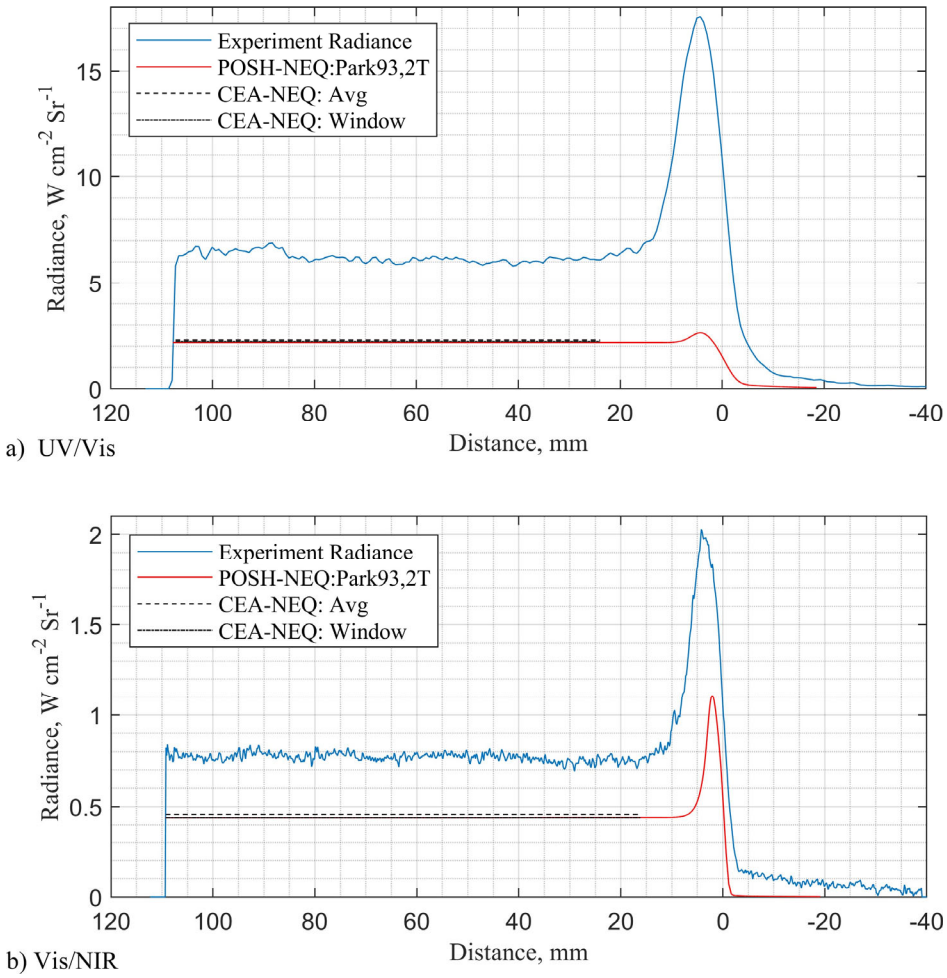

Fig. 13 Radiance profile comparisons between experiment, CEA, and POSHAX3 using Park 93 rates and a two-temperature model for test case 198, for the a) UV/Vis (210-440 nm) and b) Vis/NIR (600-840 nm) region.

B. Non-Equilibrium Metrics

Non-equilibrium data in previous work by Cruden et al. [4] [18, 19] has been analysed in terms of spectral and absolute non-equilibrium metrics (NEMs), providing a means to summarise and compare a number of simulations and experimental results while still maintaining a physically relevant meaning. The spectral NEM is defined as the average radiance within ±20 mm of the peak radiance, giving a result as a function of wavelength, as shown in equation 1(where L is the spectral radiance, W cm^{-2} sr^{-1} μm^{-1}). The absolute NEM is the integrated radiance of the spectral NEM, as shown in equation 2.

$$NEM_{\text{spec}}(\lambda) = \frac{1}{D_{\text{tube}}} \int_{y_{\text{pk}}-20}^{y_{\text{pk}}+20} L(y,\lambda)\, dy \tag{1}$$

$$NEM_{\text{abs}} = \frac{1}{D_{\text{tube}}} \int_{\lambda_{\text{low}}}^{\lambda_{\text{high}}} \int_{y_{\text{pk}}-20}^{y_{\text{pk}}+20} L(y,\lambda)\, dy\, d\lambda \tag{2}$$

An illustration of the ±20 mm region centered on the peak radiance is illustrated in Fig. 14. These metrics capture the non-equilibrium peak and are long enough to contain the camera and optical smearing functions, enabling comparison of data between tests with different values of these experimental parameters. The experimentally obtained spectral non-equilibrium metrics for each test case are included in the data summary of Appendix A, along with summary plots in Appendix B to aid comparison between test cases.

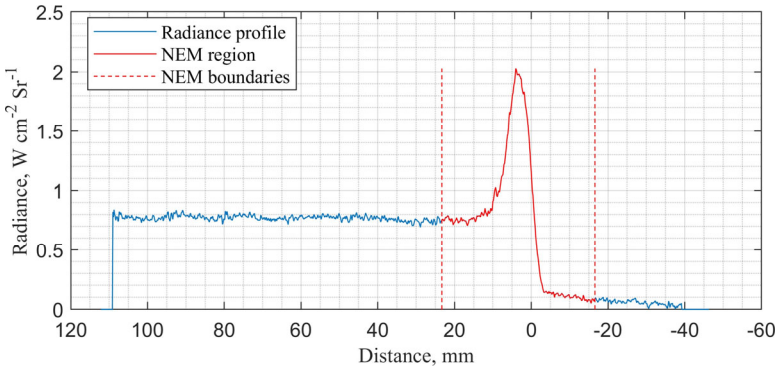

Fig. 14 Illustration of the region integrated for the non-equilibrium metrics, ±20 mm of the peak radiance, for the Vis/NIR region of test case 198.

C. Results

The absolute NEM values for the 1 bar post-shock test cases are plotted against shock speed in Fig. 15 and Fig. 16 for the UV/Vis and Vis/NIR regions respectively. These are compared to the results of the POSHAX3-NEQAIR simulations, corresponding radiance profiles for which are included in Appendix A. In the Vis/NIR region, the experimental data displays an exponential increase in non-equilibrium radiance with shock speed. This trend seems to be captured by the POSHAX3-NEQAIR simulations, though is significantly underpredicted (60 to 70%) at the cases available for comparison. The absolute NEM for the 1 bar post-shock experimental data of the UV/Vis region also increases with shock speed and is generally one order of magnitude greater than the Vis/NIR region. The trend exhibits a more asymptotic increase with velocity, as opposed to exponential, with a sudden drop after around 6.6 km/s corresponding to the decrease in spectral NEM from the NO region (see Fig. 35 in Appendix B). The NO species radiating from 200 to 300 nm are the most intensely radiating species of both the wavelength regions considered in this paper and hence have a noticeable effect when their dissociation rates increase to reduce their number densities. Further numerical simulations and repeated testing of this regime will help to assess the legitimacy of this decrease. Thereafter, the absolute NEM continues to increase as the effects of increasing velocity outweigh the reducing NO number densities. The POSHAX3-NEQAIR simulations underpredict the UV/Vis absolute NEM values by 70-80% in this region, again demonstrating inaccurate capturing of the thermochemical state in the non-equilibrium region at these conditions.

Figure 17 and Fig. 18 display the absolute NEM as a function of post-shock pressure between cases with similar shock speeds for the UV/Vis and Vis/NIR regions respectively. POSHAX3-NEQAIR comparisons are once again

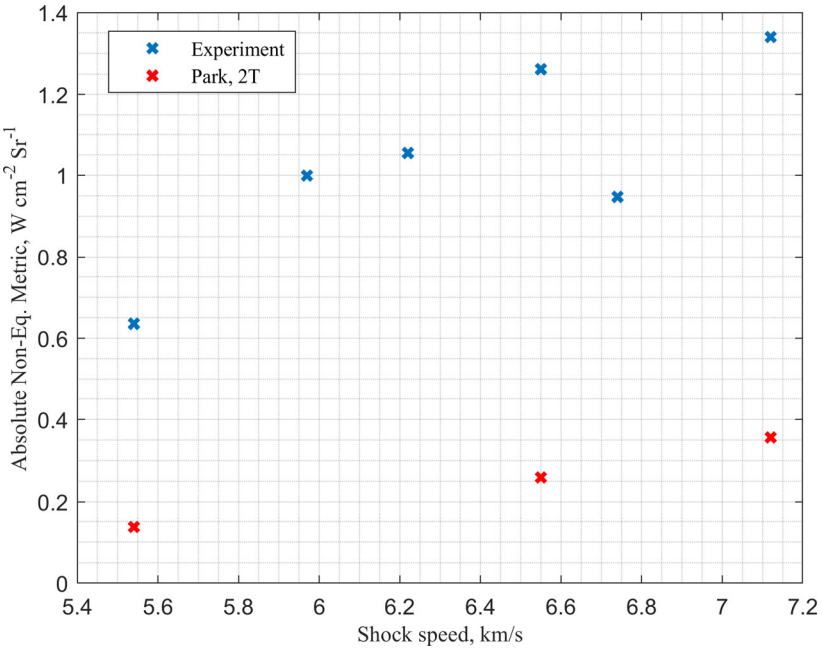

Fig. 15 Summary of absolute NEM values versus shock speed from 210 to 440 nm, at 1 bar post-shock pressure. POSHAX3-NEQAIR simulation results from a two-temperature model using Park 1993 rates are shown for comparison at nominal and extreme conditions.

provided for comparison, plotted with the final post-shock pressures calculated from the POSHAX3 simulation. The increase in absolute NEM appears to be asymptotic with increase in post-shock pressure for both wavelength regions, except for the high-pressure case in the UV/Vis region where a drop in absolute NEM occurs. The asymptotic trend can be explained by the increasing number of molecules and atoms radiating as the pressure and therefore density in the radiating region increases. The absolute NEM of test case 198 is nearly double that of 207, corresponding to the increase from 0.5 to 1 bar post-shock pressure. Deviations from this trend, including the drop in the UV/Vis for the high-pressure test case, are believed to be a result of the shock speeds decreasing for each increase in post-shock pressure, preventing a true like-for-like comparison between the test cases. In addition, there could be an increase in optical thickness with post-shock pressure, reducing the measured radiation. The POSHAX3-NEQAIR simulations capture the asymptotic trend well for both wavelength regions however significantly underpredict the experiment data, by 55-60% for the Vis/NIR region and 70-85% for the UV/Vis region.

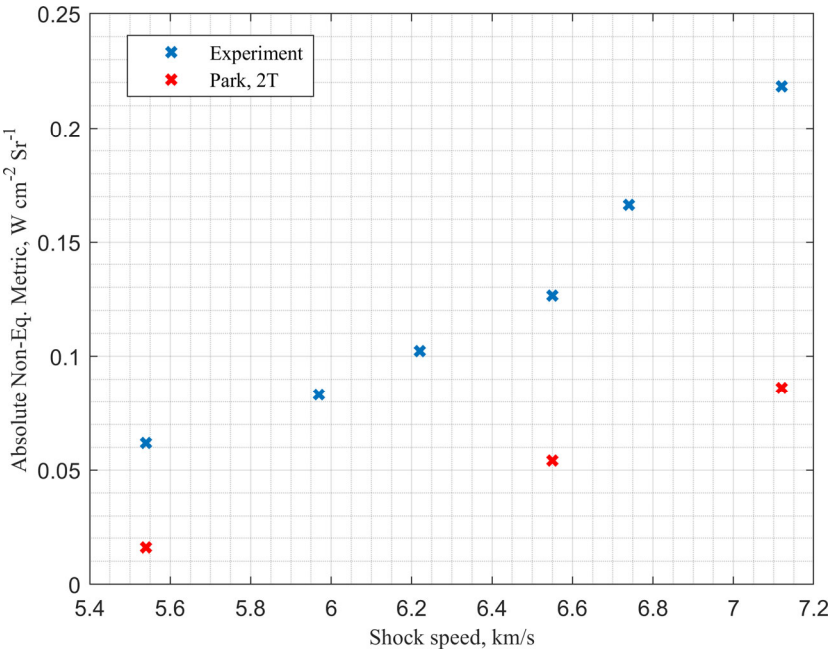

Fig. 16 Summary of absolute NEM values versus shock speed from 600 to 840 nm, at 1 bar post-shock pressure. POSHAX3-NEQAIR simulation results from a two-temperature model using Park 1993 rates are shown for comparison at nominal and extreme conditions.

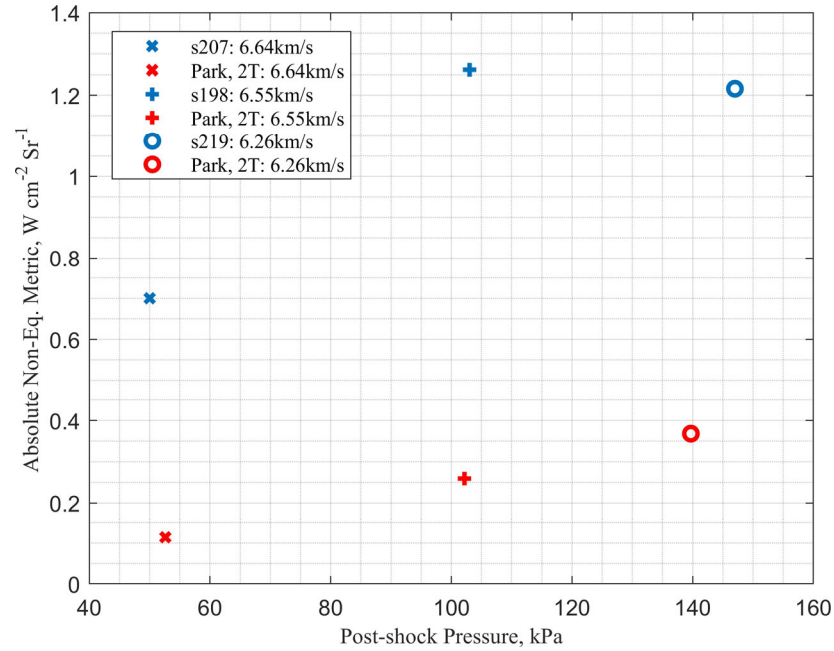

Fig. 17 Summary of absolute NEM values versus post-shock pressure from 210 to 440 nm. POSHAX3-NEQAIR simulation results from a two-temperature model using Park 1993 rates are shown for comparison.

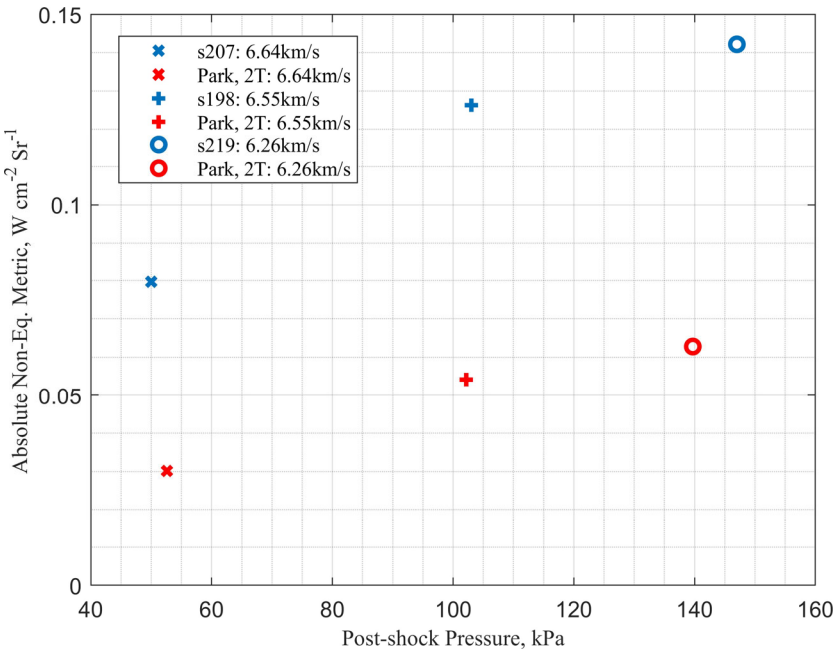

Fig. 18 Summary of absolute NEM values versus post-shock pressure from 600 to 840 nm. POSHAX3-NEQAIR simulation results from a two-temperature model using Park 1993 rates are shown for comparison.

D. Alternative Excitation Models

The radiative simulations up to now have been carried out using the non-Boltzmann rates in NEQAIR version 15.0. The nominal test case (shot 198) with 6.55 km/s shock speed at the window and 1 bar post-shock pressure, is chosen to perform a preliminary comparison of predicted absolute NEM values against a range of excitation rates, including the recently updated NEQAIR version 15.1. Table 2 compares the results of the two codes, as well as the effect of implementing alternative excitation models. The molecular excitation rates recently attained from Cruden and Brandis [4] for 7-9 km/s air shocks are compared against models using the atomic excitation rates of Huo et al. [20] and the traditional rates from Park 1990 [21]. The results predominantly underpredict the experimentally obtained absolute NEM values quite significantly, with the exception of the Cruden and Brandis molecular excitation rates in the Vis/NIR region which overpredicts considerably. The results of the Vis/NIR region show the most sensitivity to excitation model selection. All simulations relax to the same equilibrium radiance, which has been shown to underpredict the experimentally observed equilibrium radiance. This will have some effect on the predicted NEM values by inherently reducing the area in the relaxation region behind the peak. It should be noted that all kinetic modelling here has been performed using the same two-temperature model with Park 1993 rates via the POSHAX3 simulations. At the time of writing, it is too early to assess which excitation model is best for these test conditions. These analyses will continue by testing a wide range of combinations of radiative and kinetic modelling options, with the ultimate goal of extracting the rates of the thermochemical processes during the relaxation phase.

Table 2 Comparison of absolute NEM predictions from different NEQAIR excitation rate models, all performed using the two-temperature Park 1993 kinetic model, for the nominal test case 198.

NEQAIR Ver.	Model	ref	210-440nm		600-840nm	
			Abs NEM, W cm^{-2} sr^{-1}	% of Exp.	Abs NEM, W cm^{-2} sr^{-1}	% of Exp.
15.0	Default	-	0.259875	20.6	0.054213	42.9
15.1	Default	-	0.327879	26.0	0.078113	61.8
15.1	Cruden	[4]	0.305800	24.2	0.176682	139.8
15.1	Huo	[20]	0.327787	26.0	0.075196	59.5
15.1	Park	[21]	0.328082	26.0	0.083127	65.8

VI. Conclusion

Experiments of LEO return shock speeds in synthetic air have been carried out in the T6 Stalker Tunnel operating in Aluminium Shock Tube mode. Both equilibrium and non-equilbrium data from these tests have been analysed. Simulations using NASA CEA-NEQAIR codes underpredict the spectral radiance of all low-speed test cases considered. An analysis using the newly developed LASTA code for two cases with different amounts of shock deceleration has demonstrated the deceleration to have negligible effect on predicted equilibrium radiance for the cases considered, due to the minimal deceleration seen in these low-speed tests. This conclusion leaves boundary layer effects, reflections from the internal tunnel wall, the experimental background subtraction methodology and radiative modelling within NEQAIR as potential causes for the disagreement between the two data sets.

The presented absolute NEM data has shown revealed radiance from the non-equilibrium region increases exponentially with velocity in the Vis/NIR region and asymptotically in the UV/Vis, with increasing NO dissociation becoming significant from around 6.6 km/s. The post-shock pressure experienced by the radiating molecules increases non-equilibrium radiance in an asymptotic fashion, due to the increased density of radiating atoms and molecules. There is also likely an increase in optical thickness with post-shock pressure, which could influence the measurement. Comparisons made using a finite-rate one-dimensional two-temperature model with Park 1993 rates in POSHAX3 show significant underprediction of the experimental data captured, by up to 80%. A preliminary comparison of results using different excitation models within NEQAIR for a nominal test case brings simulation closer to experiment in some cases though still generally underpredicts.

These analyses will continue by comparing the equilibrium 1 bar data against equivalent conditions from the Ecole Centrale radio-frequency TAFA Model 66 ICP Torch. This approach will help to identify the source of discrepancies seen in the equilibrium data. The investigation of alternative radiative and kinetic models to simulate the non-equilibrium data will be continued. The ultimate intention for this data is to extract rates of the thermochemical processes occurring in the non-equilibrium region for these LEO return speeds. Finally, this work has presented a new experimental dataset relevant to the shock layer of LEO return conditions. This compliments and extends existing results in the literature, and can now be used to aid development and validation of numerical tests. Work in these areas is on-going.

Appendix

Experimental and simulated data for all test cases considered in this study is presented in the following figures. Section A gives a summary of the experimental equilibrium and non-equilibrium data for each test case, along with results from simulations, thus providing the information to investigate and assess each test case individually. Sections B, C and D provide a summary of all the experimental data across all cases to aid their comparison. The figures are plotted according to post-shock pressures and wavelength regions.

A. Test Case Summaries

The data presented in the figures of this section gives a summary of shock profiles, radiance profiles, equilibrium spectra and measured spectral NEM for both the UV/Vis (210-440 nm) and Vis/NIR (600-840 nm) wavelength ranges, for each individual test case. Simulations using CEA-NEQAIR and POSHAX3-NEQAIR, when relevant, are included for comparison in the figures.

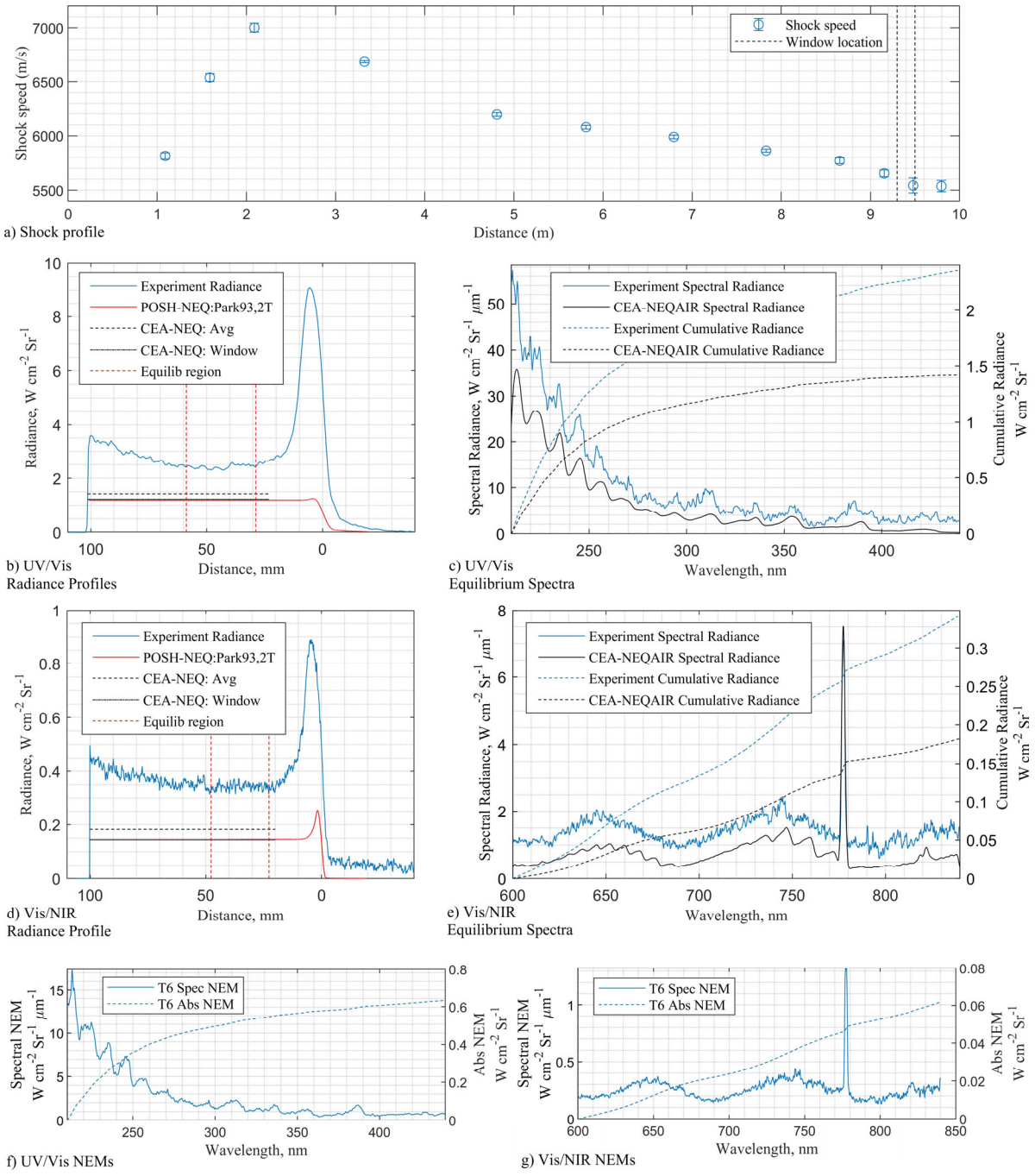

Fig. 19 Data summary for s195 at 5.66 km/s, 99 kPa post-shock pressure compared to simulations. a) shock profile; b) radiance profile and c) equilibrium spectra for UV/Vis (210-440 nm); d) radiance profile and e) equilibrium spectra for Vis/NIR (600-840 nm); measured non-equilibrium metrics for f) UV/Vis and g) Vis/NIR.

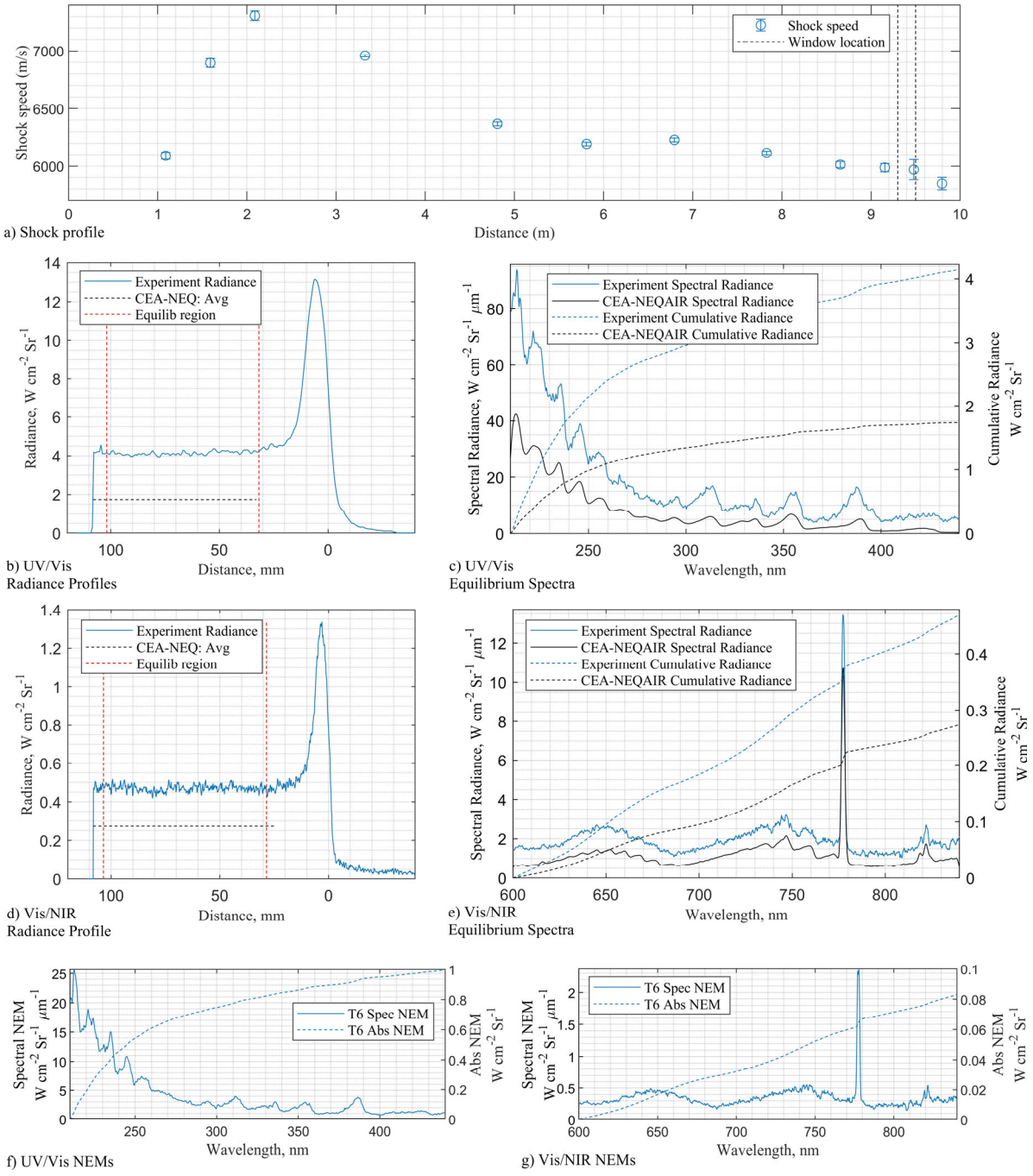

Fig. 20 Data summary for s201 at 5.99 km/s, 105 kPa post-shock pressure compared to simulations. a) shock profile; b) radiance profile and c) equilibrium spectra for UV/Vis (210-440 nm); d) radiance profile and e) equilibrium spectra for Vis/NIR (600-840 nm); measured non-equilibrium metrics for f) UV/Vis and g) Vis/NIR.

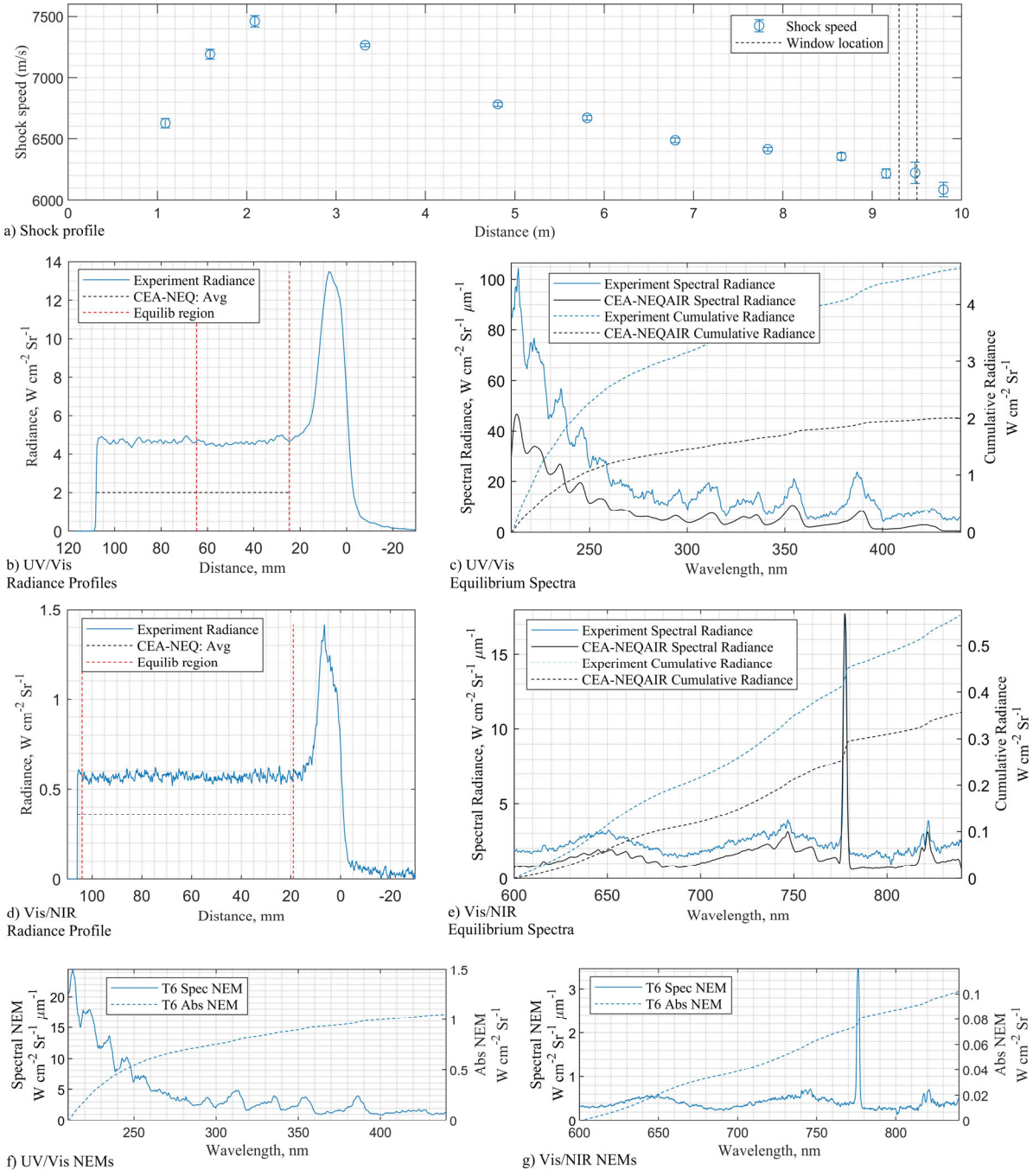

Fig. 21 Data summary for s194 at 6.26 km/s, 98 kPa post-shock pressure compared to simulations. a) shock profile; b) radiance profile and c) equilibrium spectra for UV/Vis (210-440 nm); d) radiance profile and e) equilibrium spectra for Vis/NIR (600-840 nm); measured non-equilibrium metrics for f) UV/Vis and g) Vis/NIR.

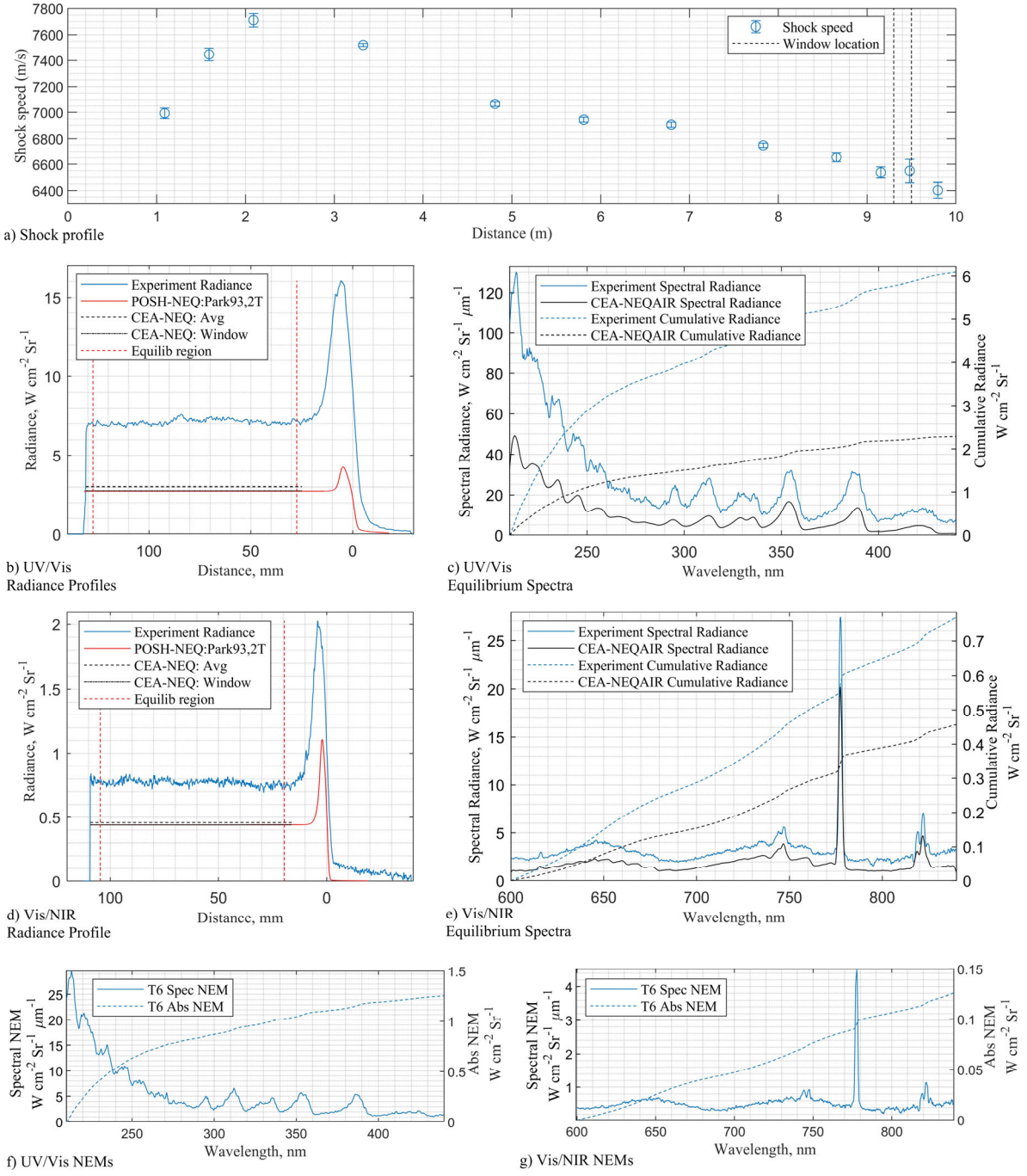

Fig. 22 Data summary for s198 at 6.58 km/s, 103 kPa post-shock pressure compared to simulations. a) shock profile; b) radiance profile and c) equilibrium spectra for UV/Vis (210-440 nm); d) radiance profile and e) equilibrium spectra for Vis/NIR (600-840 nm); measured non-equilibrium metrics for f) UV/Vis and g) Vis/NIR.

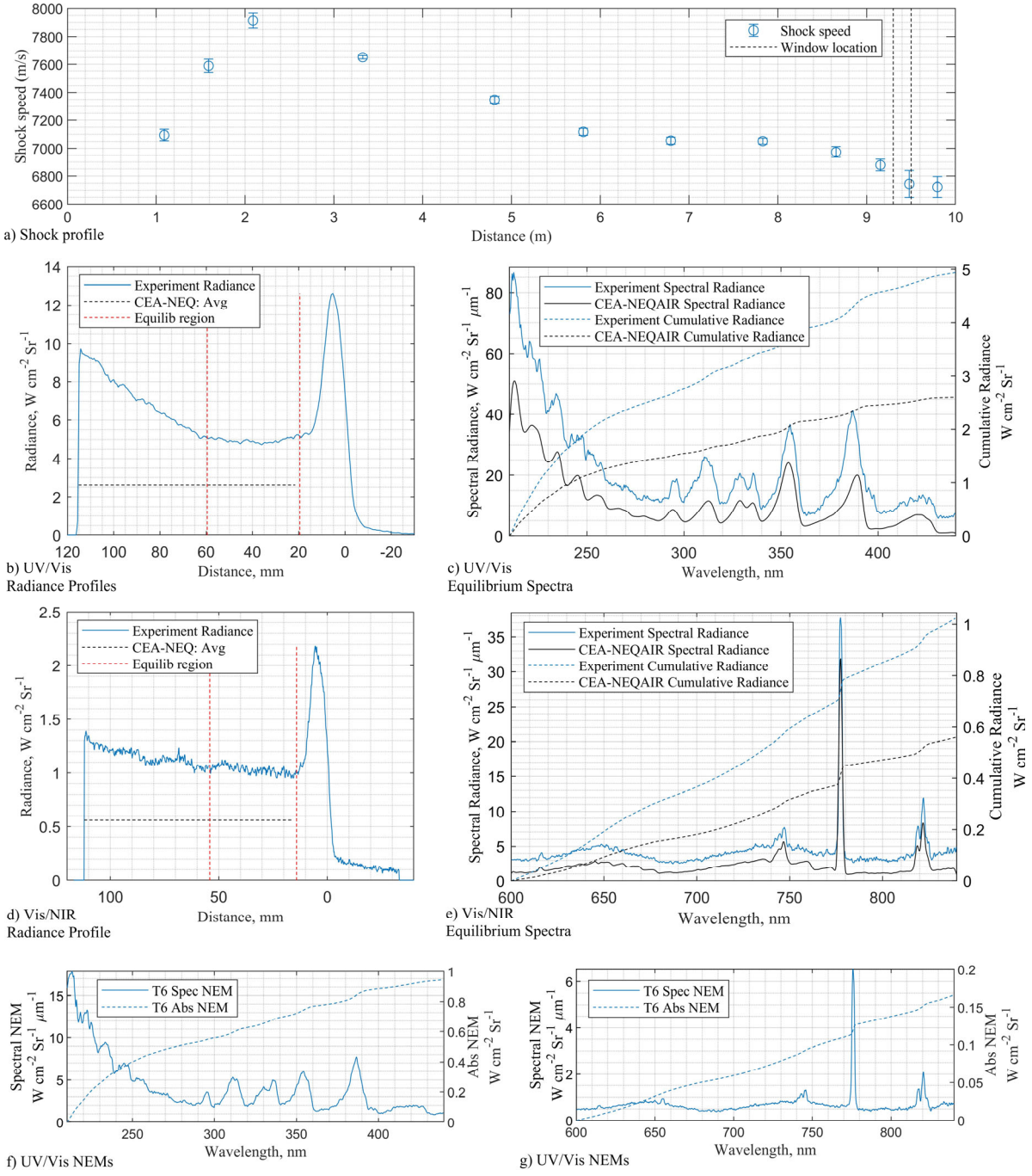

Fig. 23 Data summary for s196 at 6.87 km/s, 100 kPa post-shock pressure compared to simulations. a) shock profile; b) radiance profile and c) equilibrium spectra for UV/Vis (210-440 nm); d) radiance profile and e) equilibrium spectra for Vis/NIR (600-840 nm); measured non-equilibrium metrics for f) UV/Vis and g) Vis/NIR.

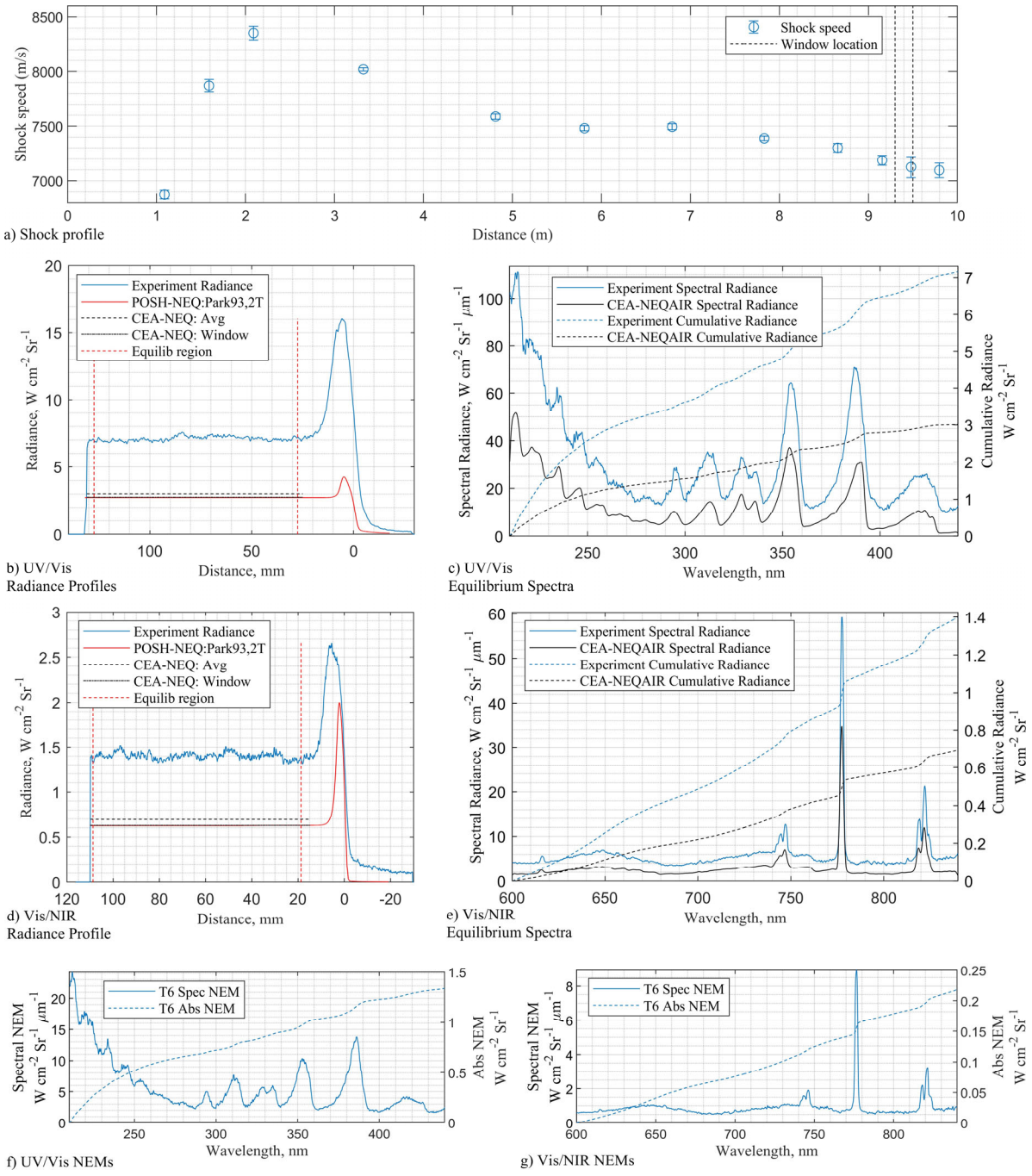

Fig. 24 Data summary for s220 at 7.21 km/s, 101 kPa post-shock pressure compared to simulations. a) shock profile; b) radiance profile and c) equilibrium spectra for UV/Vis (210-440 nm); d) radiance profile and e) equilibrium spectra for Vis/NIR (600-840 nm); measured non-equilibrium metrics for f) UV/Vis and g) Vis/NIR.

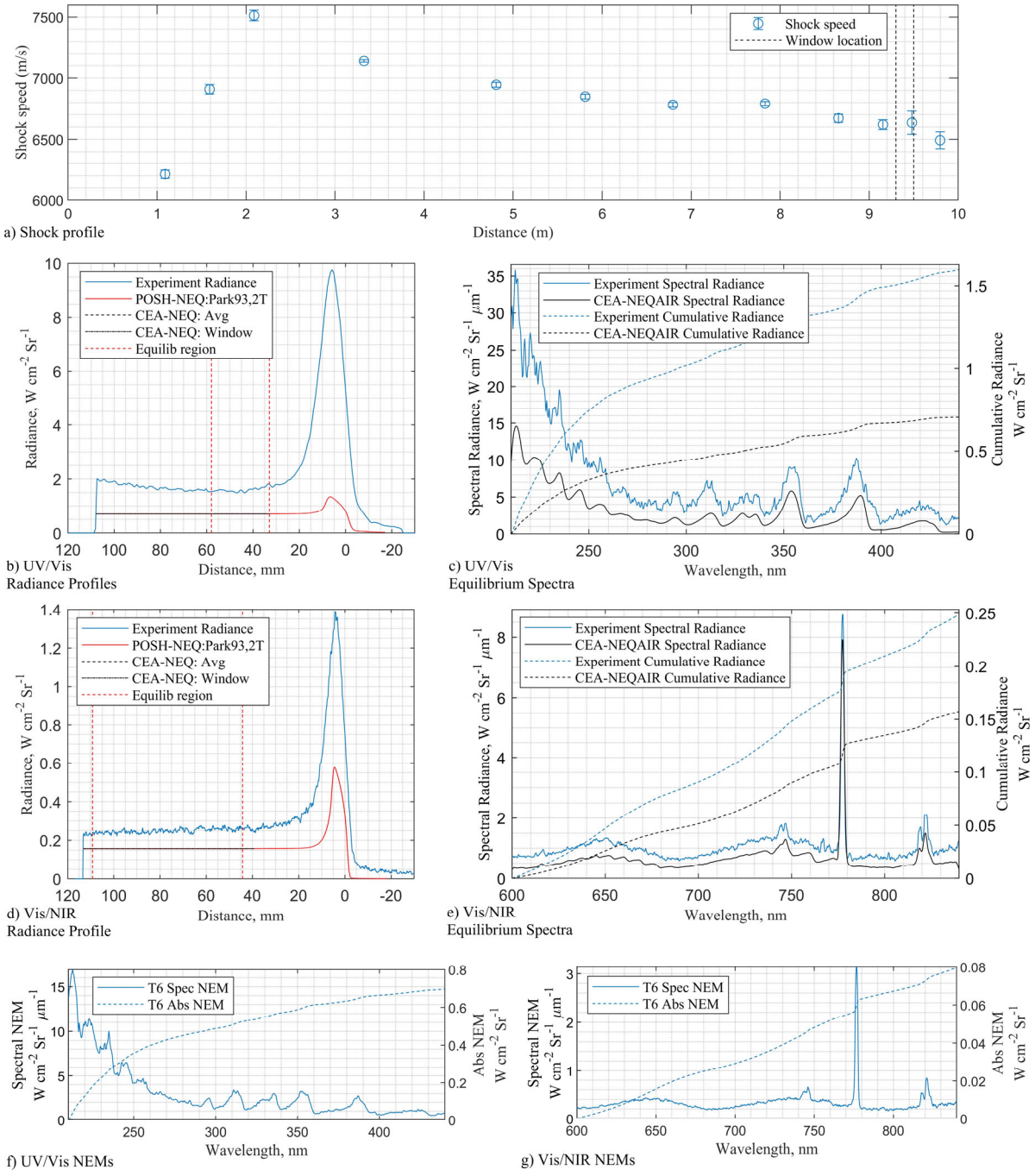

Fig. 25 Data summary for s198 at 6.64 km/s, 50 kPa post-shock pressure compared to simulations. a) shock profile; b) radiance profile and c) equilibrium spectra for UV/Vis (210-440 nm); d) radiance profile and e) equilibrium spectra for Vis/NIR (600-840 nm); measured non-equilibrium metrics for f) UV/Vis and g) Vis/NIR.

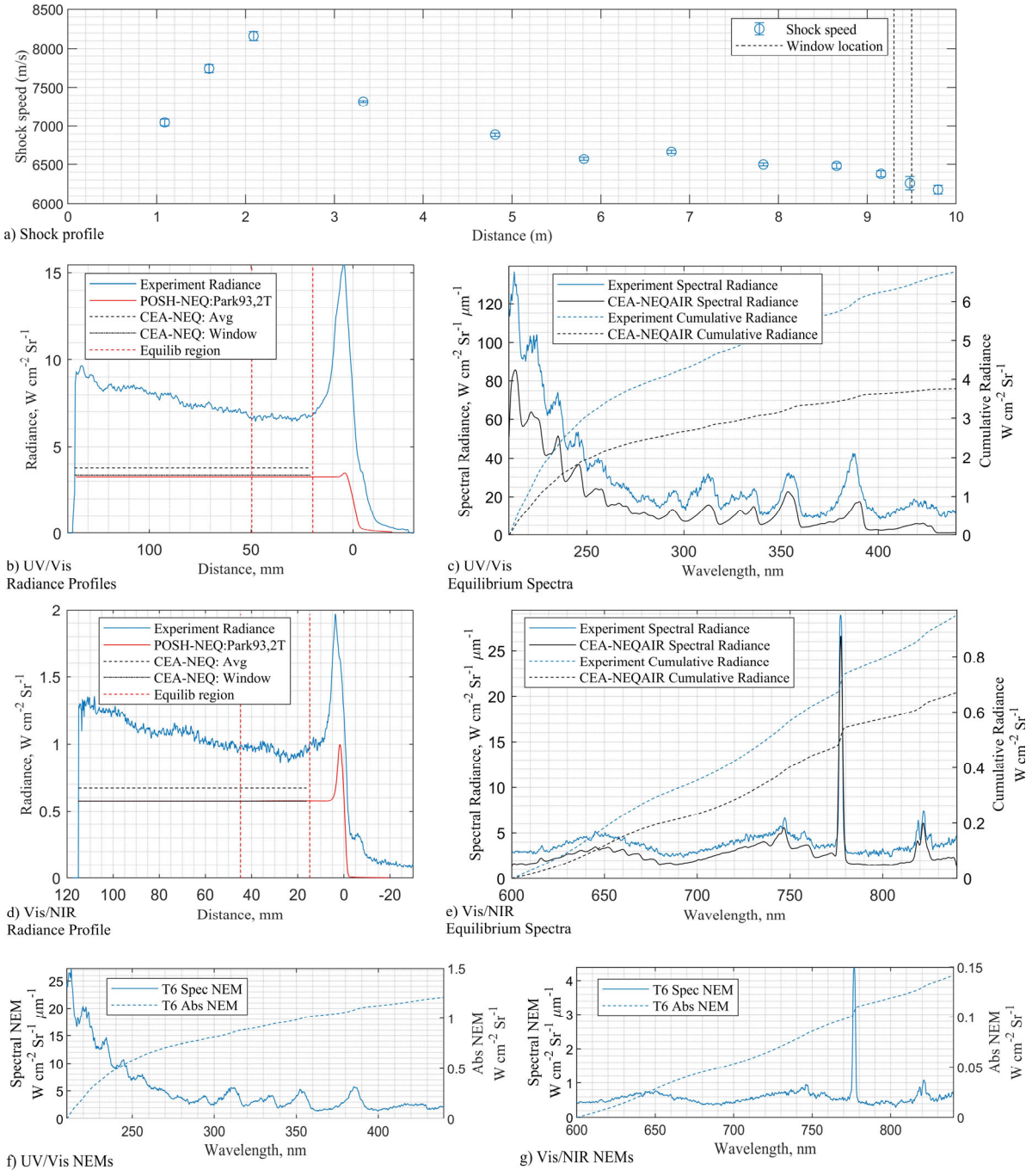

Fig. 26 Data summary for s219 at 6.37 km/s, 147 kPa post-shock pressure compared to simulations. a) shock profile; b) radiance profile and c) equilibrium spectra for UV/Vis (210-440 nm); d) radiance profile and e) equilibrium spectra for Vis/NIR (600-840 nm); measured non-equilibrium metrics for f) UV/Vis and g) Vis/NIR.

B. Equilibrium Spectra Summary

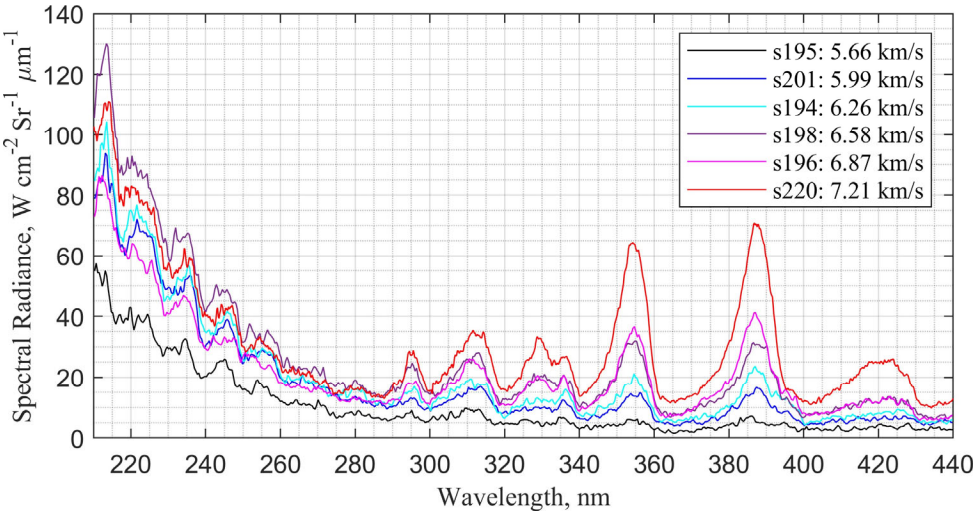

Fig. 27 Summary of spectra obtained from test cases all with 1 bar post-shock pressure in the UV/Vis region from 210-440nm.

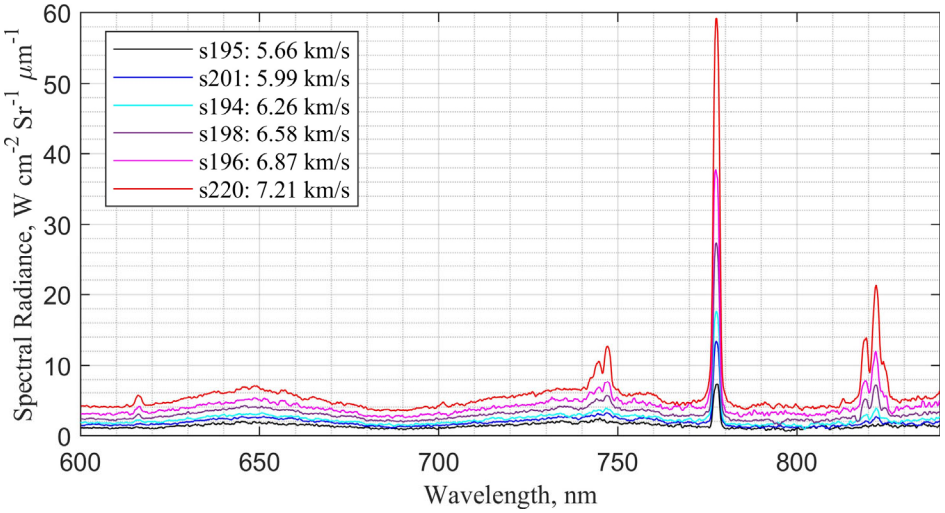

Fig. 28 Summary of spectra obtained from test cases all with 1 bar post-shock pressure in the Vis/NIR region from 600-840nm.

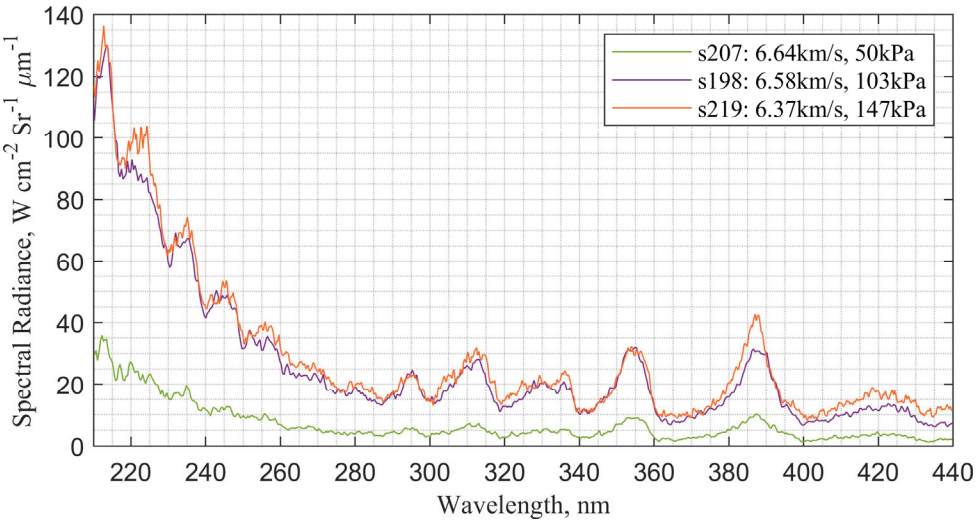

Fig. 29 Summary of spectra obtained from test cases all with 1 bar post-shock pressure in the UV/Vis region from 210-440nm.

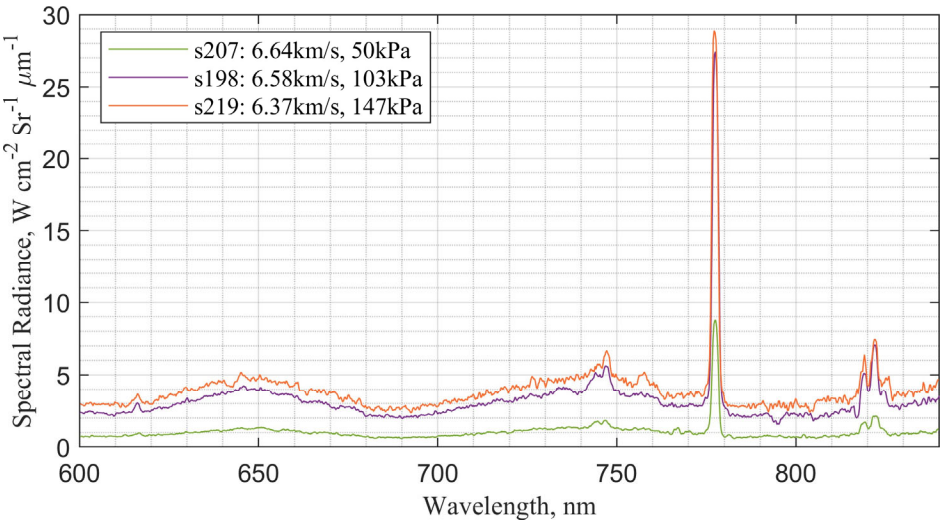

Fig. 30 Summary of spectra obtained from test cases all with similar shock speed and different post-shock pressures pressure in the Vis/NIR region from 600-840nm.

C. Radiance Profile Summary

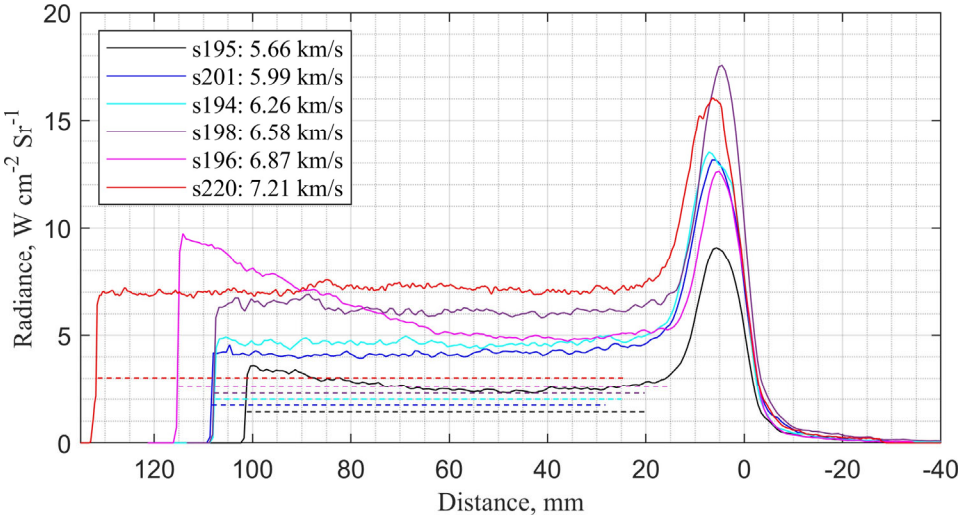

Fig. 31 Summary of radiance profiles obtained from test cases all with 1 bar post-shock pressure in the UV/Vis (210-440 nm) region. Dashed lines represent the final cumulative radiance from a CEA-NEQAIR simulation.

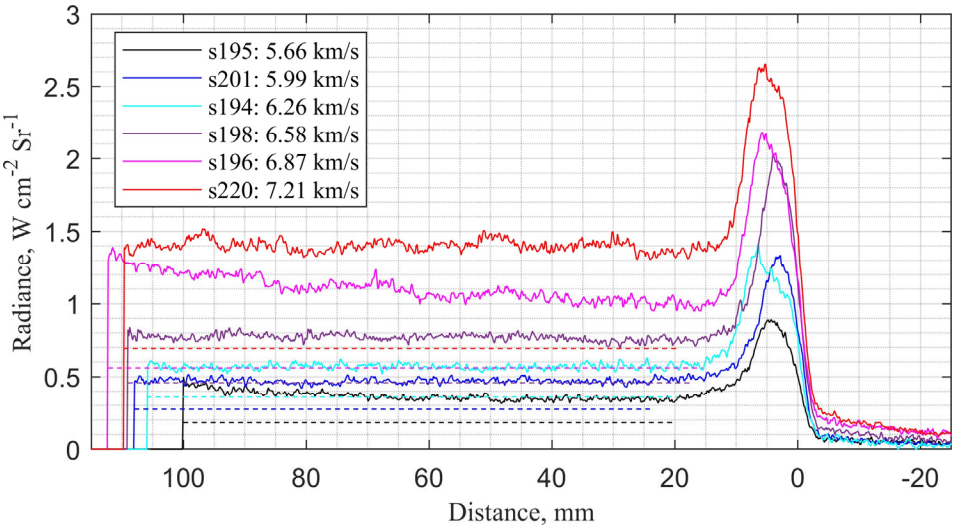

Fig. 32 Summary of radiance profiles obtained from test cases all with 1 bar post-shock pressure in the Vis/NIR (600-840 nm) region. Dashed lines represent the final cumulative radiance from a CEA-NEQAIR simulation.

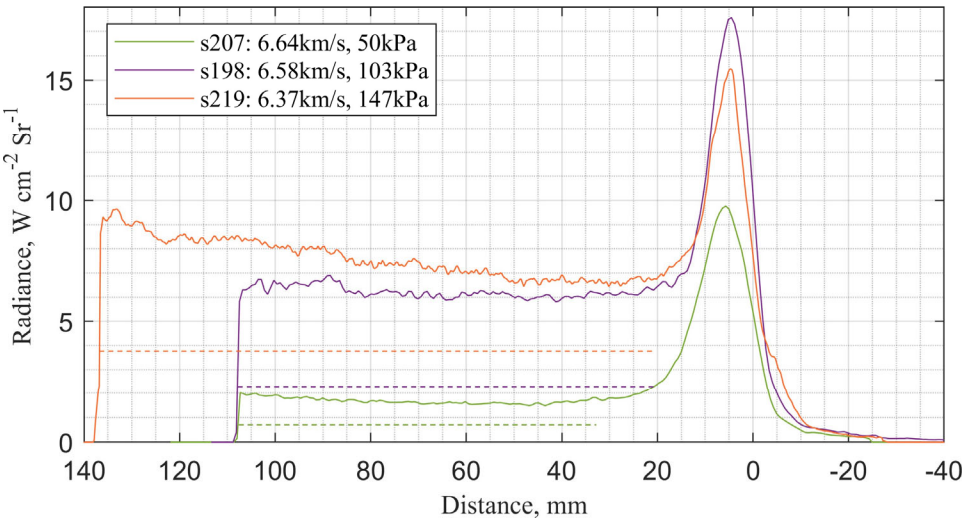

Fig. 33 Summary of radiance profiles obtained from test cases with similar shock speed and different post-shock pressure in the UV/Vis (210-440 nm) region. Dashed lines represent the final cumulative radiance from CEA-NEQAIR simulations.

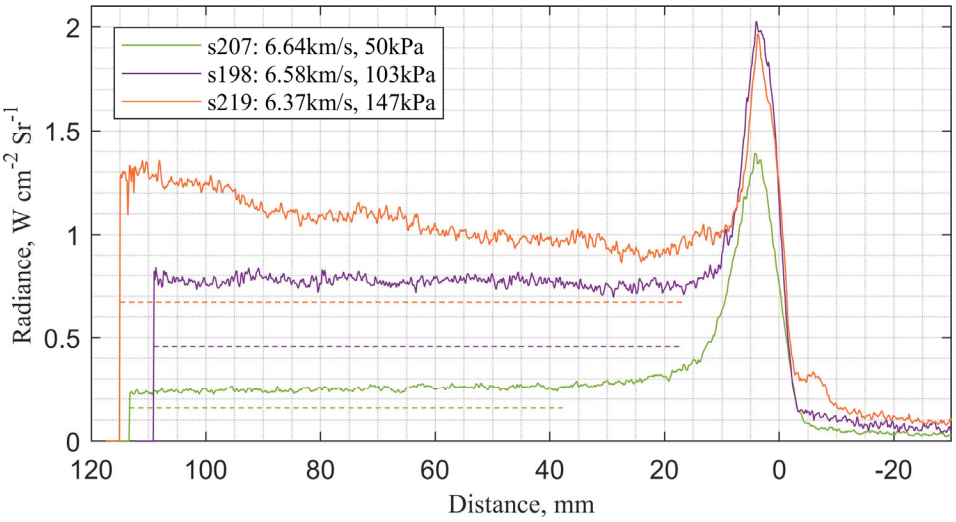

Fig. 34 Summary of radiance profiles obtained from test cases with similar shock speed and different post-shock pressure in the Vis/NIR (600-840 nm) region. Dashed lines represent the final cumulative radiance from CEA-NEQAIR simulations.

D. Spectral NEM Summaries

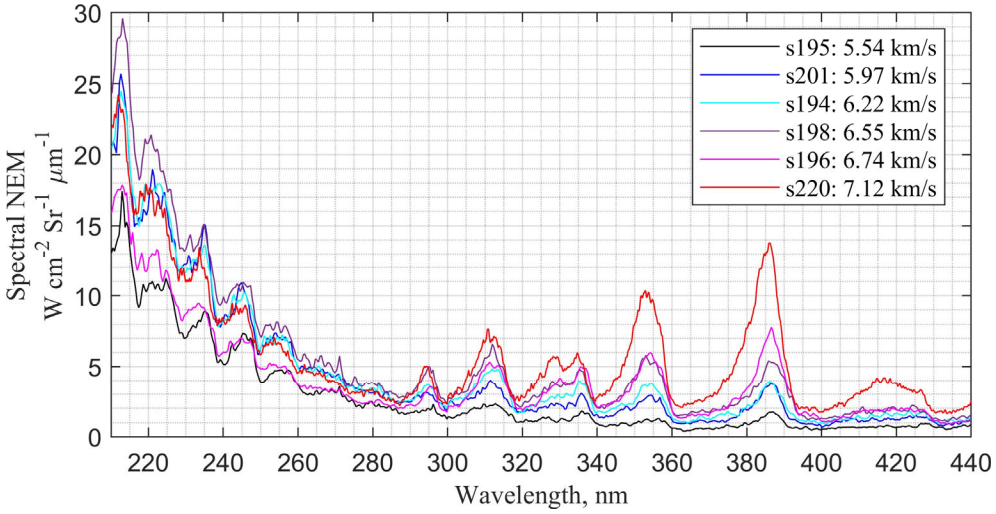

Fig. 35 Summary of spectral NEM's from the test cases with 1 bar post-shock pressure in the UV/Vis region.

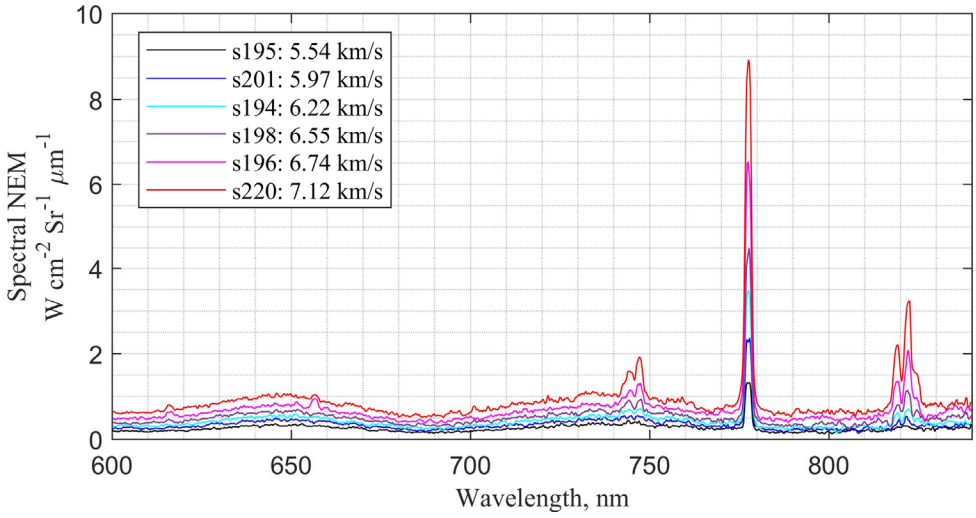

Fig. 36 Summary of spectral NEM's from the test cases with 1 bar post-shock pressure in the Vis/NIR region.

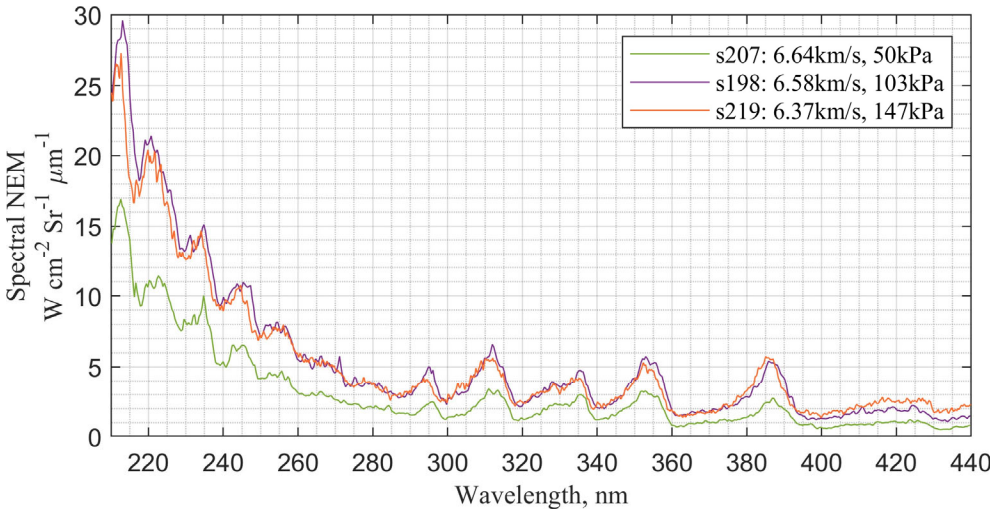

Fig. 37 Summary of spectral NEM's from the test cases with similar shock speed and different post-shock pressure in the UV/Vis region.

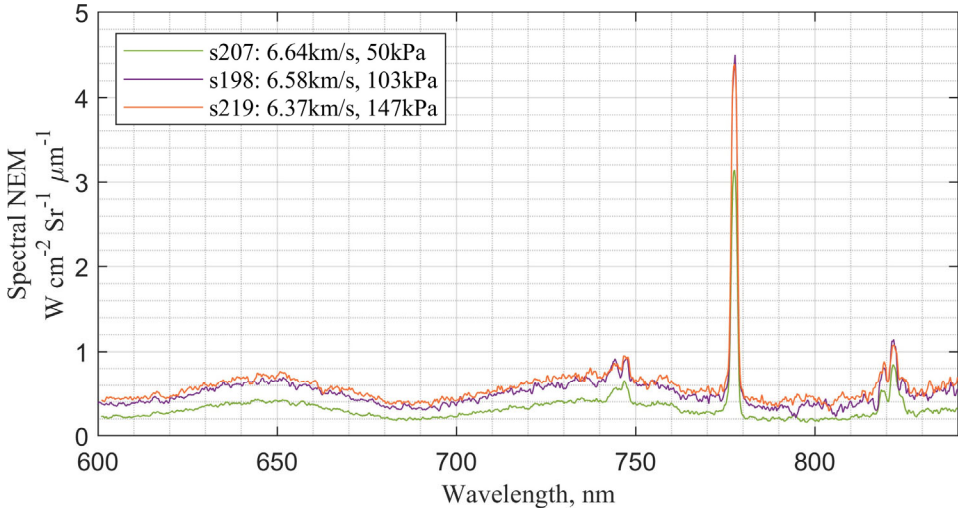

Fig. 38 Summary of spectral NEM's from the test cases with similar shock speed and different post-shock pressure in the Vis/NIR region.

Acknowledgments

The test campaign to gather data for this paper was funded by US Air Force grant FA9550-19-1-7020. The authors would like to thank Brett Cruden and Aaron Brandis at NASA Ames Research Center for their guidance on work throughout the project and for the loan of equipment, in particular the McPherson 218 spectrometer, Princeton Instruments PI-MAX2 camera and deuterium calibration lamp.

References

[1] Cruden, B. A., "Absolute radiation measurements in earth and mars entry conditions," 2014.

[2] Park, C., "Review of chemical-kinetic problems of future NASA missions. I-Earth entries," *Journal of Thermophysics and Heat transfer*, Vol. 7, No. 3, 1993, pp. 385–398.

[3] Gnoffo, P. A., Weilmuenster, K. J., Hamilton, H. H., Olynick, D. R., and Venkatapathy, E., "Computational aerothermodynamic design issues for hypersonic vehicles," *Journal of Spacecraft and Rockets*, Vol. 36, No. 1, 1999, pp. 21–43.

[4] Cruden, B. A., and Brandis, A. M., "Measurement and prediction of radiative non-equilibrium for air shocks between 7-9 km/s," 2017.

[5] Brandis, A., Johnston, C., Cruden, B., Prabhu, D., and Bose, D., "Uncertainty analysis and validation of radiation measurements for earth reentry," *Journal of Thermophysics and Heat Transfer*, Vol. 29, No. 2, 2015, pp. 209–221.

[6] Brandis, A., Johnston, C., Cruden, B., and Prabhu, D., "Equilibrium radiative heating from 9.5 to 15.5 km/s for earth atmospheric entry," *Journal of Thermophysics and Heat Transfer*, Vol. 31, No. 1, 2017, pp. 178–192.

[7] Brandis, A. M., Johnston, C. O., and Cruden, B. A., "Non-equilibrium radiation for earth entry," *46th AIAA Thermophysics Conference*, 2016, p. 3690.

[8] Collen, P., Doherty, L. J., Subiah, S. D., Sopek, T., Jahn, I., Gildfind, D., Penty Geraets, R., Gollan, R., Hambidge, C., Morgan, R., et al., "Development and commissioning of the T6 Stalker Tunnel," *Experiments in Fluids*, Vol. 62, No. 11, 2021, pp. 1–24.

[9] Collen, P., "Development of a High-Enthalpy Ground Test Facility for Shock-Layer Radiation," Ph.D. thesis, DPhil Thesis, Univ. of Oxford, Oxford, UK, 2021.

[10] Mirels, H., "Test time in low-pressure shock tubes," *The physics of Fluids*, Vol. 6, No. 9, 1963, pp. 1201–1214.

[11] James, C., Gildfind, D., Lewis, S., Morgan, R., and Zander, F., "Implementation of a state-to-state analytical framework for the calculation of expansion tube flow properties," *Shock Waves*, Vol. 28, No. 2, 2018, pp. 349–377.

[12] Collen, P., Doherty, L. J., and McGilvray, M., "Measurements of radiating hypervelocity air shock layers in the T6 free-piston driven shock tube," ESA Conference Bureau, 2019.

[13] Satchell, M., Collen, P., McGilvray, M., and Di Mare, L., "Numerical Simulation of Shock Tubes Using Shock Tracking in an Overset Formulation," *AIAA Journal*, Vol. 59, No. 6, 2021, pp. 2102–2112.

[14] Satchell, M., McGilvray, M., and Di Mare, L., "Analytical Method of Evaluating Nonuniformities in Shock Tube Flows: Theory and Development," *AIAA Journal*, 2021, pp. 1–15.

[15] Satchell, M., Glenn, A., Collen, P., Penty-Garaets, R., McGilvray, M., and di Mare, L., "An Analytical Method of Evaluating Nonuniformities in Shock Tube Flows. Part 2: Application," 2021.

[16] Satchell, M., "Numerical simulation and modeling of shock tube experiments," Ph.D. thesis, University of Oxford, 2021.

[17] Potter, D., "Modelling of radiating shock layers for atmospheric entry in Mars and Earth," Ph.D. thesis, Ph. D. Thesis, Univ. of Queensland, Brisbane, Australia, 2011.

[18] Cruden, B., "Radiance measurement for low density mars entry," *43rd AIAA Thermophysics Conference*, 2012, p. 2742.

[19] Brandis, A., Johnston, C., Panesi, M., Cruden, B., Prabhu, D., and Bose, D., "Investigation of nonequilibrium radiation for Mars entry," *51st AIAA Aerospace Sciences Meeting including the New Horizons Forum and Aerospace Exposition*, 2013, p. 1055.

[20] Huo, W. M., Liu, Y., Panesi, M., Wray, A., and Carbon, D. F., "Electron-impact excitation cross sections for modeling non-equilibrium gas," *53rd AIAA Aerospace Sciences Meeting*, 2015, p. 1896.

[21] Park, C., "Nonequilibrium Hypersonic Aerothermodynamics," 1990.

Pure Nitrogen

The next paper presents the absolute radiance data gathered in pure nitrogen tests, at conditions close to the previous synthetic air cases. A similar summary of plots including experimental data and simulation predictions are provided. The goal of performing pure nitrogen tests is to simplify the chemical kinetics and number of possible energy exchange mechanisms, to provide a simpler problem to validate numerical models against. Less species present in the resulting spectra also makes it easier to distinguish specific spectral features from one another and allow for a more detailed analysis focusing on individual species.

Contents

Experimental Radiation Measurements in Nitrogen

A.B. Glenn*, J. Clarke†, P.L. Collen‡, Luca Di Mare§ and M. McGilvray¶
Osney Thermofluids Institute, University of Oxford, United Kingdom

Absolute radiance measurements of pure nitrogen have been performed in the Oxford T6 Stalker Tunnel while operating in Aluminium Shock Tube mode. Spatially and spectrally resolved data has been attained for shock speeds from 5.45 to 7.24 km/s. Post-shock pressures of 1 bar were predominantly targeted, as well as 0.5 and 1.5 bar. Data is presented in the form of equilibrium spectral radiance and spatially dependent radiance profiles integrated over designated wavelength regions. Equilibrium spectral radiance profiles are compared against CEA predictions, while LASTA and NESS simulation results are plotted against the spatial radiance profiles. Together these help to assess the level of equilibrium attainment; account for the effects of variations in shock speed and a growing boundary layer; and assess the modelling of non-equilibrium vibrational relaxation processes. Number densities and temperatures from the aforementioned codes are fed into NEQAIR v15.1 to convert to radiation predictions. Where relevant, synthetic air spectra for similar conditions are also provided. Scaled comparisons suggest the addition of oxygen species becomes more negligible to the chemistry of nitrogen-only mechanisms as shock speed increases. The aim of this paper is to provide fundamental data for kinetic and radiative model validation, for a simplified set of species relevant to planet entry of nitrogen rich atmospheres.

I. Introduction

Thermochemical phenomena that occur during a planet entry mission as a result of the high-temperature gas effects have been studied since the 1960s. Under such conditions, dissociation and ionisation reactions occur, as well as radiation emission, as species in excited energy states try to relax to a new equilibrium. Though these events have implications to entry vehicle design, the radiation emission provides a means to perform non-intrusive optical spectroscopy measurements. Due to the expense of real flight experiments, ground test facilities have traditionally been used to recreate these high-enthalpy flow conditions, to capture clean radiation data, amongst other parameters, and inform computational models. Experiments are routinely run on a number of ground test facilities, such as the Electric Arc Shock Tube (EAST) at NASA Ames [1] and Inductively Coupled Plasma (ICP) Torch at CentraleSupélec [2], where it is common practice to match the test gas composition to the planet atmosphere as close as possible. Such experiments have also previously been performed in the Oxford T6 Stalker tunnel [3–5], capable of operating in two shock tube modes [6–8]. Chemical kinetic rates are extracted [9] and implemented into computational models to predict the shock layer radiation environment ahead of an entry vehicle. High-speed entries (>10 km/s for air) warrant consideration due to radiative heating and are dominated by atomic spectral features [10–12]. At lower speeds, reaction rates decrease and the non-equilibrium region can contribute a more significant portion of the total shock layer radiation, dominated by molecular features such as NO, N_2 and N_2^+ for Earth entry. This exercises different components of computational models, which have been shown to produce larger disagreement for synthetic air in both EAST and T6 shock tube facilities [6, 13] at these lower speeds. Reducing uncertainties of non-equilibrium radiation has been identified as one of planet entry gas dynamics' highest priorities for the last 20 years [14].

The goal of this paper is to perform a more fundamental study by providing radiation data in pure nitrogen, that can be used for model development of nitrogen rich atmospheres. Reducing the number of reactants in turn reduces the number of possible collision partners and the complexity of energy exchange reactions. Similar experiments have previously been performed in EAST (Test 62) [15, 16] and the ICP torch [17]. The data herein extends the available data set of benchmark conditions generated by EAST, to higher fill pressures at low speeds, more relevant to Low Earth Orbit (LEO) trajectories. Conditions with a post-shock pressure of 1 bar were nominally targeted, to allow comparison

*DPhil Candidate, Department of Engineering Science, Oxford Thermofluids Institute, University of Oxford
†DPhil Candidate, Department of Engineering Science, Oxford Thermofluids Institute, University of Oxford
‡Postdoctoral Researcher, Department of Engineering Science, Oxford Thermofluids Institute, University of Oxford
§Associate Professor, Oxford Thermofluids Institute, Department of Engineering Science, University of Oxford
¶Associate Professor, Oxford Thermofluids Institute, Department of Engineering Science, University of Oxford

to equivalent synthetic air data [6] and plasma torch experiments. Brandis and Cruden [15] highlight that by removing oxygen from synthetic air studies, the 11 species and 21 chemical reactions to consider are simplified to only 5 species (N, N^+, N_2, N_2^+, e^-) and 4 reaction mechanisms, summarised as:

$$N_2 + M \longleftrightarrow N + N + M \tag{1}$$

$$N + e^- \longleftrightarrow N^+ + e^- + e^- \tag{2}$$

$$N + N \longleftrightarrow N_2^+ + e^- \tag{3}$$

$$N^+ + N_2 \longleftrightarrow N_2^+ + N \tag{4}$$

The data here can be used for fundamental model development, for which considerable efforts have been made [18]. Molecular nitrogen theoretical works have identified discrepancies with current modelling in relation to vibrational energy states and relaxation times [19–21]. Analysis work carried out by Cruden and Brandis [15] measured radiation in shock heated nitrogen flows at velocities from 6 to 12 km/s in a freestream pressure of 0.2 Torr. Equilibrium spectral radiance was generally found to be under-predicted by CEA-NEQAIR across all speeds, from 130 to 1650 nm. The nitrogen test data attained from T6 AST is intended to be a continuation of these studies, expanding the range of conditions and to allow future cross-facility comparisons. In addition, the computational tools available to analyse shock tube data post-test have improved since the previous works. This is demonstrated through the use of LASTA [22, 23] and NESS [24] codes, developed at the University of Oxford. Where appropriate, synthetic air data for comparable conditions have also been included to help assess how addition of oxygen contributes to consumption of nitrogen species via alternate reaction mechanisms and production of species such as NO.

A description of the T6 Aluminium Shock Tube experimental set up is provided in Section II. This is followed by a summary of the pure nitrogen conditions achieved in Section III, and the analysis codes used to generate numerical predictions in Section IV. Results in the form of equilibrium spectral radiance and spatial radiance profiles are given in Section V. Finally, these are discussed in Section VI.

II. Experimental Setup

All experimental data presented in this paper was obtained from the Oxford T6 Stalker Tunnel, which has been described in detail in previous works by Collen [3, 4, 8]. In addition, an account of the specific Aluminium Shock Tube (AST) set up for the experiments in question has previously been given by Glenn et al. [6]. Thus, only a brief summary is provided herein.

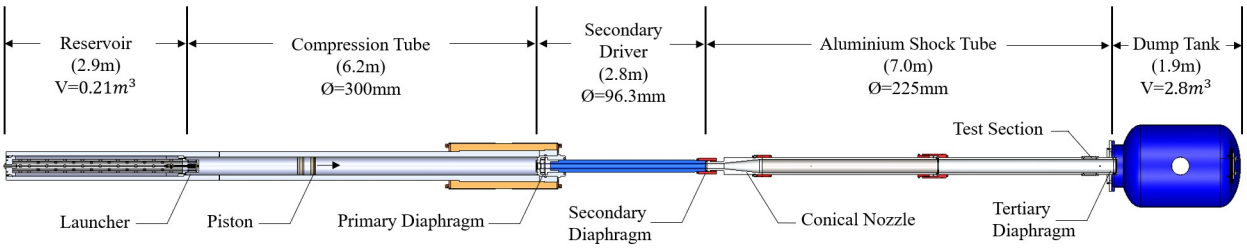

Fig. 1 Section view of T6 Stalker tunnel in Aluminium Shock Tube mode from above

Figure 1 shows a cross-section view of the T6 facility in AST mode. A free-piston driver is used to polytropically compress a helium-argon mixture in the compression tube until rupture of the primary diaphragm to generate a shock wave which then travels downstream. Prior to this rupture, the AST section has been filled with a test gas relevant for the planet entry test case of interest. The normal shock wave progresses through the test gas, compressing and accelerating the gas to travel downstream. An analogy is made to relate the flow between the normal shock and the contact surface (with the driver gas), in the shock tube, to the stagnation streamline from the bow shock to the boundary layer edge ahead of an entry vehicle. The shock tube is filled with equivalent composition and density to the desired planet atmosphere and altitude, and a driver condition selected to produce a normal shock travelling at the same speed

as the vehicle for the chosen trajectory point. This enables recreation of the thermochemical evolution through the entire test slug, equivalent to the vehicle shock layer through the stagnation line, including the non-equilibrium and relaxation processes. After primary diaphragm rupture, the continued piston motion acts to delay expansion wave generation and propagation, helping to postpone shock deceleration. The driver gas expanding out into the driven section cushions the piston to allow for a "soft" landing at the end of the compression tube. An optional secondary driver between the driver and AST can be filled with helium, through use of a secondary diaphragm, to reach faster shock speeds [25] . In cases when it is not needed, there is no secondary diaphragm and the secondary driver is filled with the test gas.

Two major inconsistencies with the analogy between shock tube and entry vehicle stagnation line that have been highlighted in recent literature are: 1. Variations in shock speed within a shock tube experiment; 2. the presence of a growing boundary layer. The effect of the former has been well documented in works of Satchel et al. [22,23] and Collen et al. [26], demonstrating shock speed variations directly lead to thermochemical gradients in the resulting test slug, which can be seen in radiance measurements. The latter has recently been documented in works of Clarke et al. [24]. The presence of a growing boundary layer around the circumference of the tube inner wall introduces differences in particle time of flight through a test slug, compared to a vehicle stagnation line. This is owed to extraction of particles from the test gas core flow as they are consumed by the boundary layer. Correcting for this particle time of flight has drastically reduced discrepancies between shock tube experimental data and simulations over a blunt body, originally thought owed to incorrect reaction rates. This correction is particularly important for gases or conditions with long relaxation times.

The design of the AST lends itself to low-speed shock layer radiation studies. The 225 mm diameter tube provides a large integration path-length for optically thin radiation, which increases signal-to-noise ratio. Reduced boundary layer effects results in less shock deceleration and therefore longer test gas slugs [27]. Considerable effort is devoted to minimising all leaks since inadequate sealing has the potential to invalidate all spectral data gathered. For the data presented here, ultimate pressures of less than 1 Pa were achieved after flushing with the test gas, and leak rates less than 1 mPa/s. The quality of the sealing was demonstrated by pure nitrogen shot T6s225, 6.33 km/s and 213.5 Pa fill, looking in the UV/Vis region. The resulting spectrum is shown in Fig. 2. Since NO species will radiate strongly at these conditions, the lack of signal at the lower wavelengths indicates only very low concentrations of oxygen would be present. The leak rate was thus deemed acceptable to carry out the pure nitrogen experiments presented herein, and the wavelength of the UV/Vis system was shifted to look at higher wavelengths for the remaining shots, where radiating species are present.

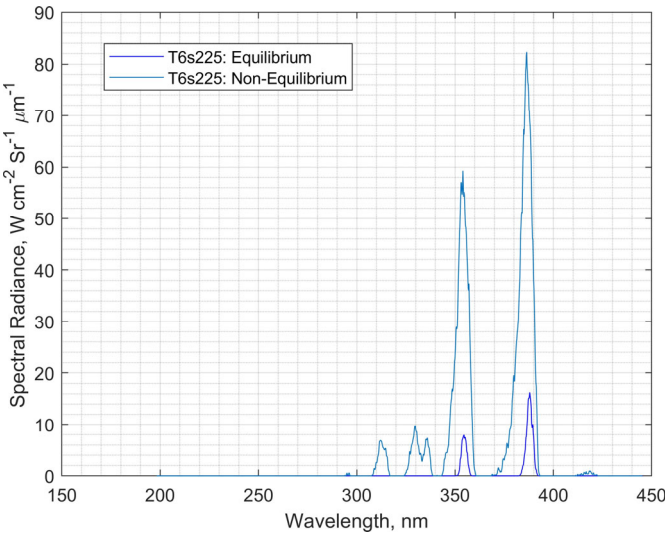

Fig. 2 UV/Vis spectra from T6s225, 6.33 km/s shock speed at window and 213.5 Pa fill. No signal at the lower wavelengths demonstrates low leak rate.

Primary analysis of the test gas is performed in the downstream section at the windows just before the dump tank, via a dual Optical Emission Spectroscopy (OES) setup, as illustrated in Fig. 3. Radiation emitted from the test gas escapes through two 200 mm long diametrically opposite windows along the tube axis, 9.3 m from the primary diaphragm.

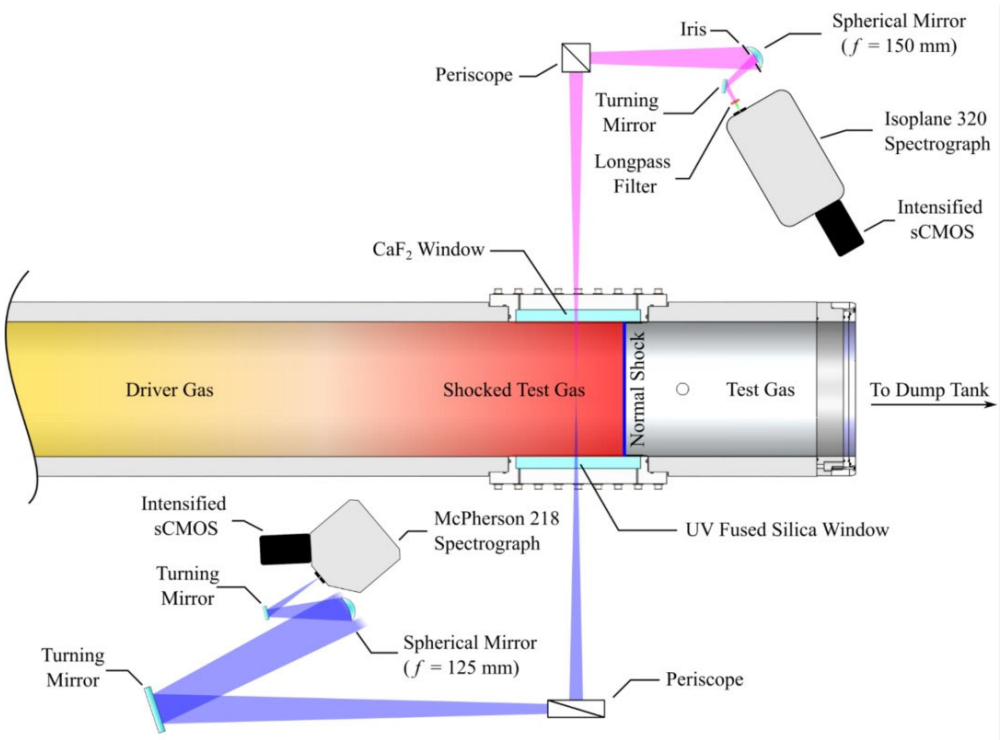

Fig. 3 The red (upper) and blue (lower) optical emission spectroscopy systems. Not to scale.

Both windows have their own optical path and spectrometer, each with a designated wavelength region. For the pure nitrogen tests discussed here, a "blue side" is used to capture Ultraviolet/Visible wavelengths from 290 to 520 nm, and a "red side" for Visible/Near Infrared from 600 to 840nm. Radiation along the length of the window is focused on the spectrometer slit; it is then spectrally separated by a diffraction grating while retaining its spatial profile along the tube axis. The wavelength-dispersed image then falls on the camera sensor at the spectrometer outlet to finally capture the spatially and spectrally resolved image. Exposure times of 1us or less are used to minimise smearing due to shock motion. Both sides used intensified Andor sCMOS cameras to capture radiation, while the red side spectrometer was a Princeton Instruments Isoplane-320 and the blue side a McPherson 218 0.3m. 150 G/mm and 180 G/mm low resolution gratings were employed on the red and blue OES systems respectively to provide access to broad wavelength ranges.

The raw images taken by the cameras provide data with signal in units of counts. In order to convert this to spectral radiance, calibrations were performed using a uniformly radiating integrating sphere to produce a full field calibration at wavelengths above 300 nm for both the red and blue optical paths. In addition, a Deuterium lamp is used to calibrate the blue side wavelengths below 300 nm. Calibrations were performed before every test, following the methodology of Cruden [1].

III. Conditions Achieved

The conditions achieved in the pure nitrogen test cases are plotted in Fig. 4. Similar conditions from synthetic air tests previously shown in [6] are also included for comparison. Table 1 summarises information regarding the pure nitrogen tests under consideration. The shock speeds quoted are representative of the speed of the shock as it passes the windows where the OES systems are focused.

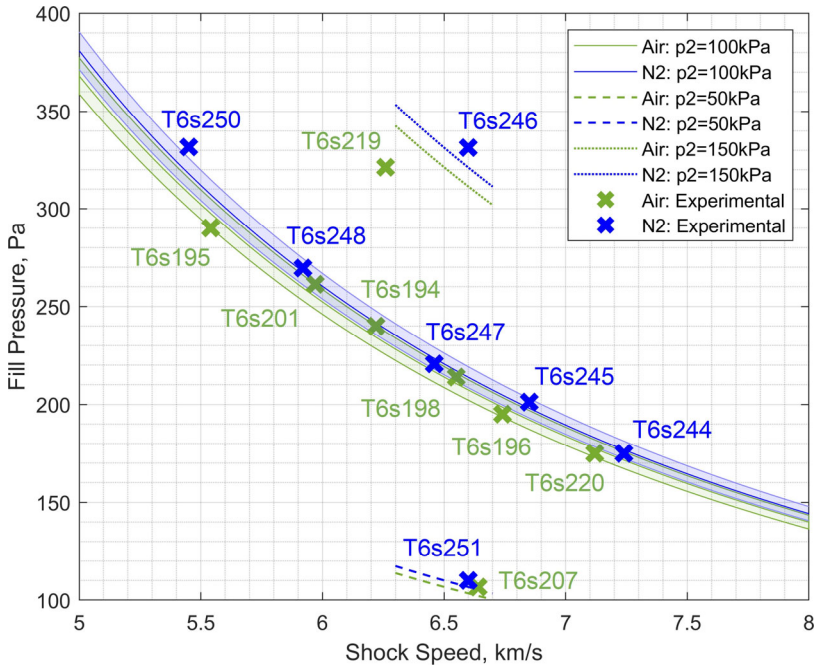

Fig. 4 Pure nitrogen conditions achieved, compared against the synthetic air conditions from [6]. Shaded regions indicate ± 2.5 kPa post-shock pressure.

In the light of recent work from Satchel et al. [22,23], demonstrating the effect of shock trajectory on thermochemical gradients in the resulting test slug, the shock speed profiles for the considered nitrogen cases are given in Fig. 5. These plots are derived from the distance-time shock trajectory information that is fed into LASTA simulations, as explained in the following section.

Table 1 Summary of pure nitrogen conditions obtained from T6 Stalker tunnel.

Shot no.	P_{fill} (Pa)	Shock speed (km/s)	$P_{2,Meas}$ (kPa)	$P_{2,CEA}$ (kPa)	$T_{2,CEA}$ (K)
T6s250	331.7	5.45	104	103.9	6359
T6s248	269.6	5.92	102	100.5	6564
T6s247	220.6	6.46	101	99.6	6801
T6s245	201.1	6.85	105	101.7	6959
T6s244	175.0	7.24	98	98.6	7098
T6s251	110.1	6.60	53	52.4	6647
T6s246	331.4	6.60	133	148.1	6930

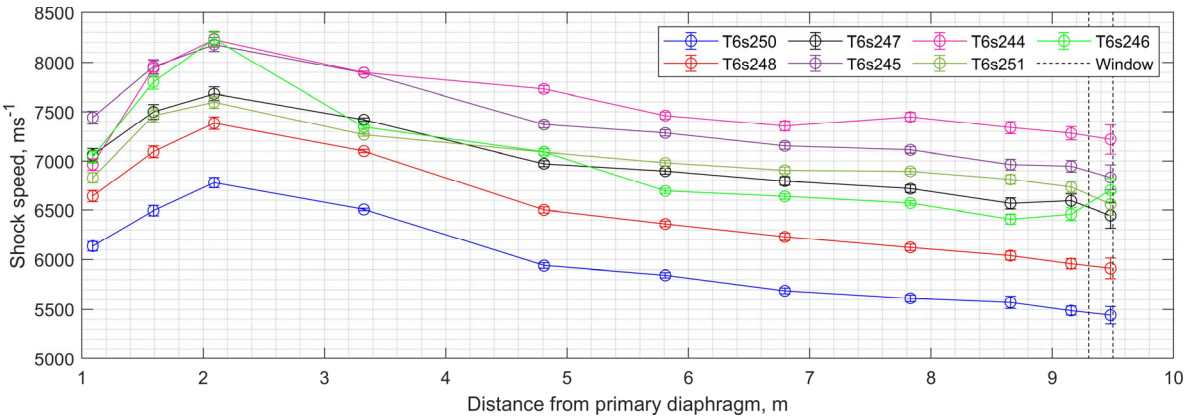

Fig. 5 Summary of pure nitrogen test shock speed profiles. Solid lines between data points are included to improve plot readability, not to indicate linear variations in shock speed.

IV. Summary of Codes

A. CEA

Chemical Equilibrium with Applications (CEA) [28] is a NASA code to calculate equilibrium mass or mole fractions given a set of reactants under specified conditions. The subsequent thermodynamic and transport properties of the resulting mixture are also predicted. When run as a shock problem, specification of the normal shock speed, freestream pressure and composition provide CEA enough information to predict the resulting species number densities and shock layer equilibrium temperatures, assuming all reactions have run to completion.

B. LASTA

LAgrange Shock Tube Analysis (LASTA) is a quasi one-dimensional code developed at the University of Oxford to predict the thermochemical variations in the post-shock test gas of a shock tube experiment, by discretising the test slug into a number of slices. The distance-time data from a given shot, along with fill pressure, composition and tunnel dimensions are fed into LASTA to predict the compression and expansion waves required to induce the measured normal shock trajectory. The influence of those pressure waves on the thermochemical properties of each gas slice are calculated, allowing reconstruction of the test slug of a given experiment. This provides a means to account for test-to-test variations in simulations. Like CEA, it assumes the reactions within each slice have run to completion, and is thus limited to equilibrium solutions. LASTA calls an in-house developed equilibrium solver "OCEAN" to calculate the variation in thermodynamic and transport properties through the resulting test slug. A full review of the principles of operation of LASTA and validation can be seen in the works of Satchel et al. [22, 23]. This code has since resolved historical discrepancies between experimental data from the Electric Arc Shock Tube (EAST) facility and predictions from radiative transport codes [26], owing to shock deceleration.

C. NESS

Non-Equilibrium Shock Solver (NESS) is a new computationally low-cost non-equilibrium solver being developed at the University of Oxford and has been summarised in previous work by Clarke et al. [24]. It allows resolution of shock structure, capturing translational and vibrational excitation and relaxation for a two-temperature model. Additionally, it accounts for mass loss to the boundary layer and boundary layer compression. Inputs required are specification of the chosen thermochemistry regime, shock speed, tube diameter and fill pressure, temperature and composition.

D. NEQAIR

Non-EQuilibrium AIr Radiation (NEQAIR) is a line by line radiation code developed by NASA, which computes spontaneous emission, absorption and stimulated emission due to transitions between various energy states of species along a line of sight [29]. The number densities and temperatures generated by the aforementioned codes are fed into

NEQAIR to generate predictions for both equilibrium and non-equilibrium radiance. Numerous updates and versions have been made since the original reporting of Whiting et al. [30]. In this paper, all simulations have been performed using NEQAIR v15.1.

V. Results

A. Calibrated Absolute Spectral Radiance

This section provides a summary of pure nitrogen absolute radiance measurements performed in the T6 Aluminium Shock Tube, from Fig. 6 to Fig. 12. Data from both the UV/Vis (290 - 520nm) and Vis/NIR (600 - 840 nm) are presented in the form of equilibrium spectral radiance, and spatial radiance profiles integrated over designated wavelength regions. The importance of the spectral resolution is demonstrated by the strong wavelength dependence. Equilibrium spectral radiance profiles are compared against CEA-NEQAIR predictions. NEQAIR simulations have been performed from 290 to 840 nm, assuming boltzmann distributions of energy states, with the spectral convolution function switching to the relevant OES system at 560 nm.

LASTA- and NESS-NEQAIR simulation results are included with the measured spatial radiance profiles. The former accounts for the effects of shock speed variations and the growing boundary layer, and the influence this has on the particle time of flight. While NESS is used to predict the non-equilibrium thermochemistry and vibrational relaxation. These codes are evaluated by feeding the line of sight calculated into NEQAIR, to compare the predicted radiance against that measured. NEQAIR simulations used a non-boltzmann distribution for the lines of sight generated by NESS. Two spectral regions chosen to integrate over in this paper are the entire UV/Vis and Vis/NIR regions, as these represent the total difference in radiance from the experiment, to assess the overall performance of the numerical tools. Additionally, specific local regions have been targeted in each spectrum. It is evident that an offset between the experiment and predictions is present in all test cases, increasing towards the lower wavelengths where molecular features predominantly reside. By integrating over a smaller spectral region where there is a dominant atomic or molecular feature, the proportion of signal due to the enhanced background radiation is reduced. This a favourable effect for the comparison of specific spectral features, and will be more valid for the higher speed test cases, where there's more distinct strong features. The background offset is consistent across all pure nitrogen and synthetic air high-pressure low-speed test cases, the origin however is still under investigation. In the Vis/NIR, the atomic N multiplet was selected, by integrating from 817-826 nm, where the signal is strongest in comparison to the background signal. In the UV/Vis region, a combination of N2 and N2+ molecular features, from 320 - 340 nm, is chosen. The first peak is due to N2+ emission and the second from N2. These are not the features of strongest radiance, however they are away from CN violet radiation (~350 - 430 nm), present due to carbon contamination on the tube walls.

To compare the radiance profiles predicted by the simulation tools against that experimentally measured by the OES setup, the simulated profiles must be convolved with the spatial blurring effects, or "Spatial Resolution Function" (SRF) as referred to by Cruden [1]. This is composed of three components: Optical; Camera; Shock motion. The optical blurring component is characterised by a ray tracing code of the optical set up. Since telescopic OES systems were used, this is a function of distance from the optics centreline. The location of the shock was therefore used for each test case, so it is valid for the non-equilibrium region. The camera blurring component is due to charge sharing between adjacent pixels of the camera and is characterised by experimental measurement of the point spread function. Finally, the component due to motion of the shock during the camera gating time is accounted for by a square pulse with width equal to the distance the shock will travel during the gating. This could be improved by measuring the gating function of the cameras, however for relatively long exposure times of 0.5 to 1 μs a square pulse is believed to be a reasonable approximation.

Where possible, synthetic air data from [6] for similar conditions have been included for comparison. This helps to evaluate the role of oxygen species when displacing nitrogen species and consuming them in additional reaction mechanisms. Plots of similar pairs of pure nitrogen and synthetic air shock speed profiles are given in the Appendix.

Figure 12 contains the plots for T6s246, the high pressure condition. Here, two plateaus were observed in the post-shock test gas. The reasons for this are unknown, and believed to likely be anomalous, however the spectra from each region have been plotted non the less.

1. 1 bar Post-Shock Conditions

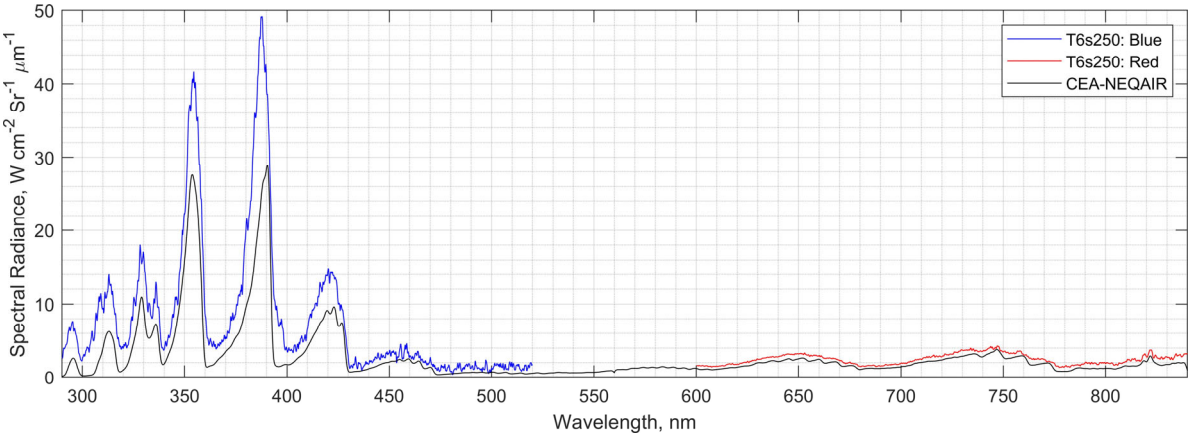

(a) T6s250: Experiment equilibrium spectra vs CEA-NEQAIR

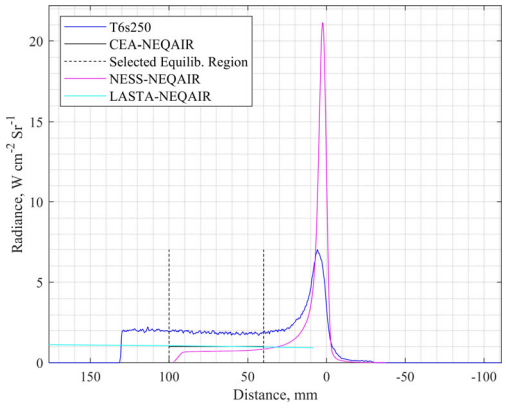

(b) T6s250 Radiance: 290-520 nm

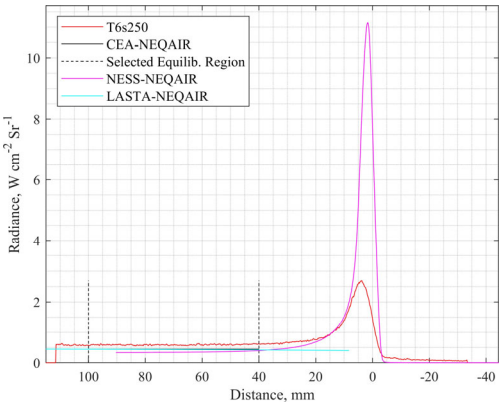

(c) T6s250 Radiance: 600-840 nm

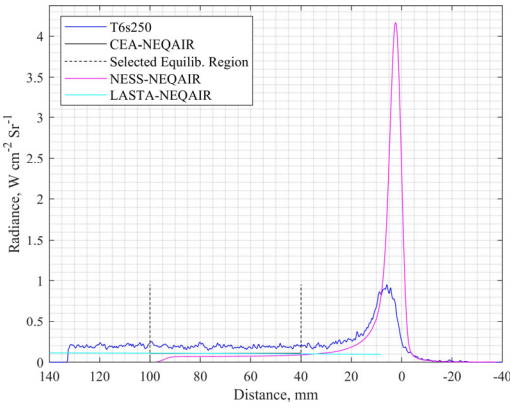

(d) T6s250 Radiance: 320-340 nm

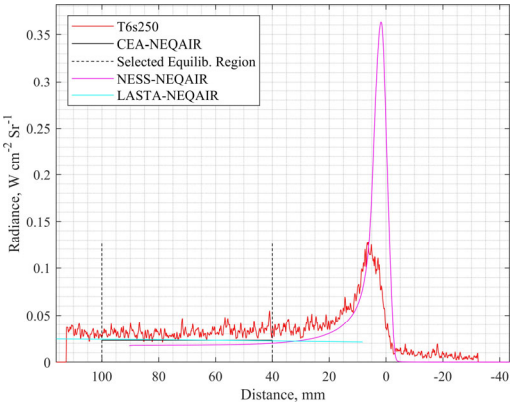

(e) T6s250 Radiance: 816-827 nm

Fig. 6 Equilibrium spectra and radiance profiles for T6s250, 5.46 km/s and 331.7 Pa fill, vs numerical predictions.

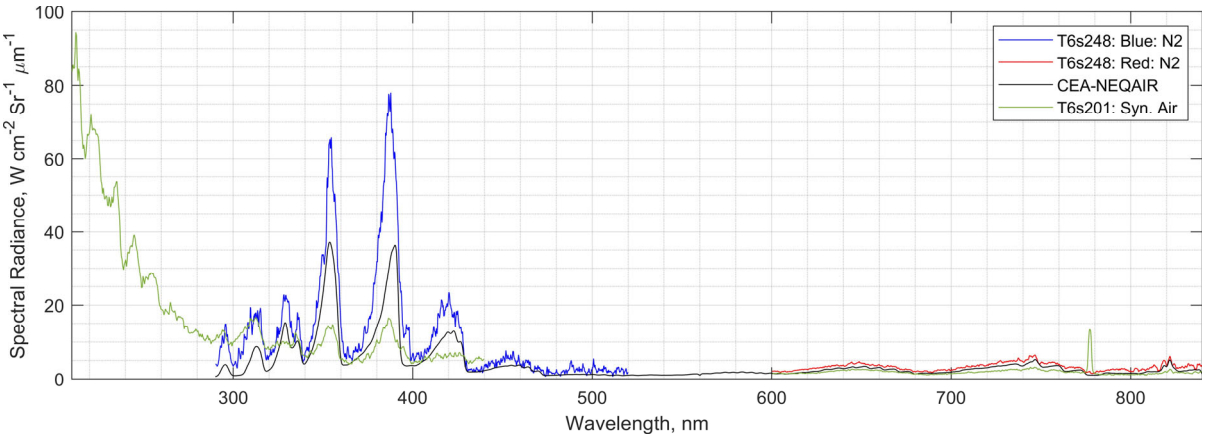

(a) T6s248: Experiment equilibrium spectra vs CEA-NEQAIR

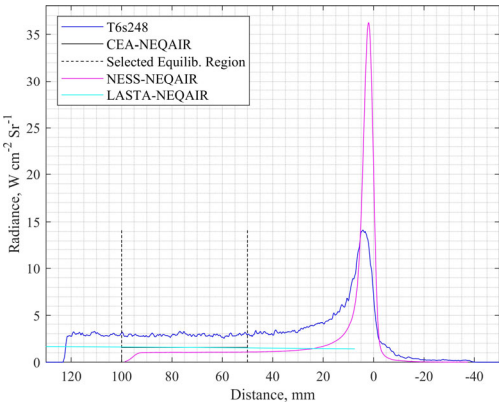

(b) T6s248 Radiance: 290-520 nm

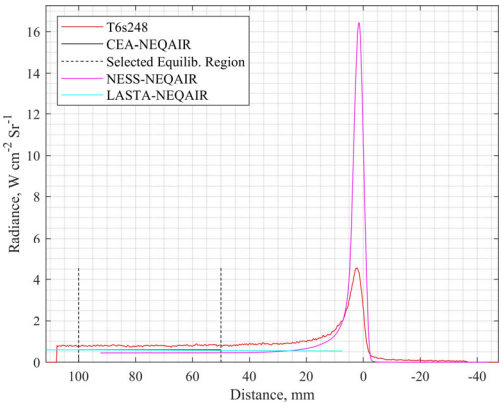

(c) T6s248 Radiance: 600-840 nm

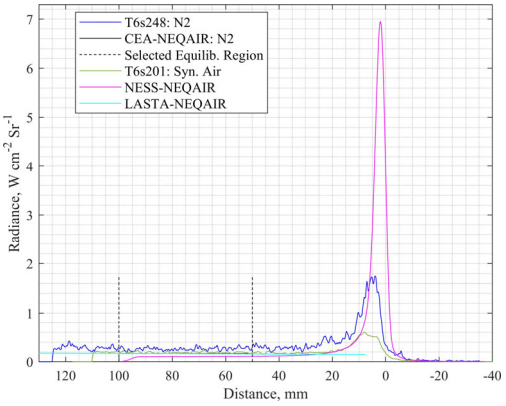

(d) T6s248 Radiance: 320-340 nm

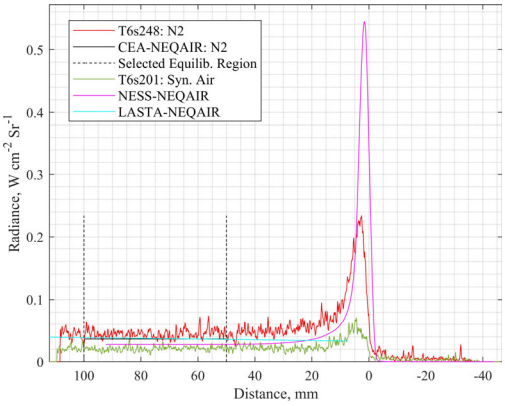

(e) T6s248 Radiance: 816-827 nm

Fig. 7 Equilibrium spectra and radiance profiles for T6s248, 5.92 km/s and 269.6 Pa fill, vs numerical predictions. Synthetic air data from T6s201, 5.97 km/s and 261.2 Pa fill, is included for comparison.

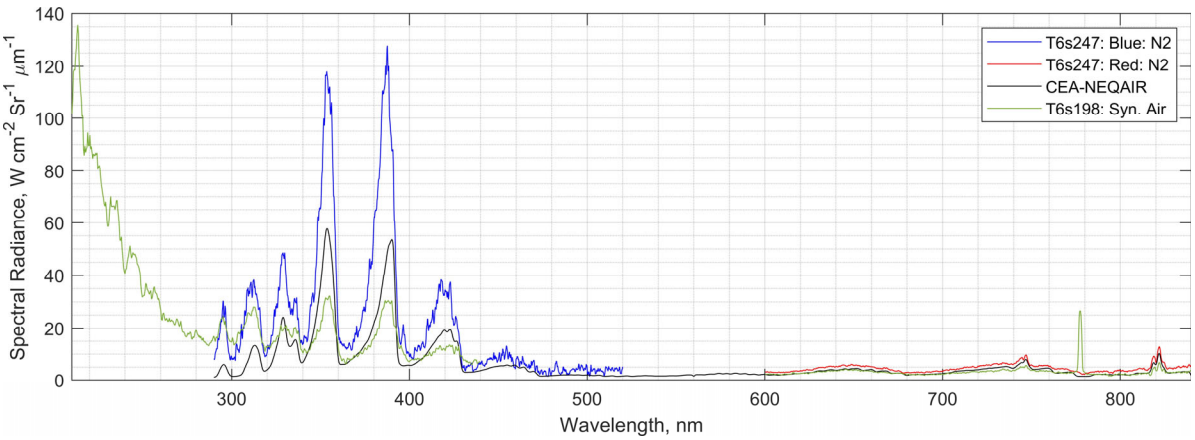

(a) T6s247: Experiment equilibrium spectra vs CEA-NEQAIR

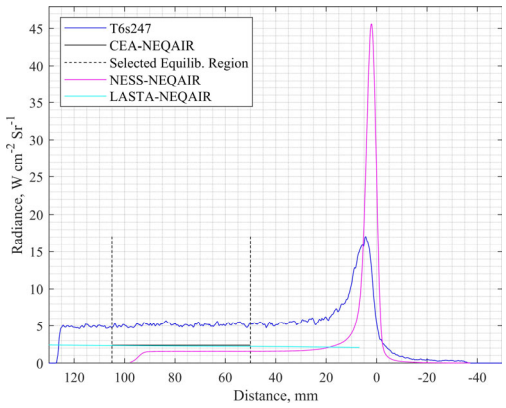

(b) T6s247 Radiance: 290-520 nm

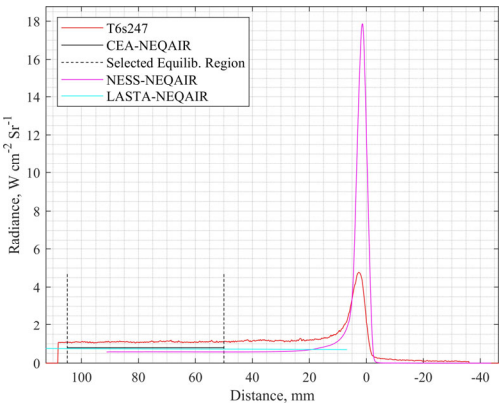

(c) T6s247 Radiance: 600-840 nm

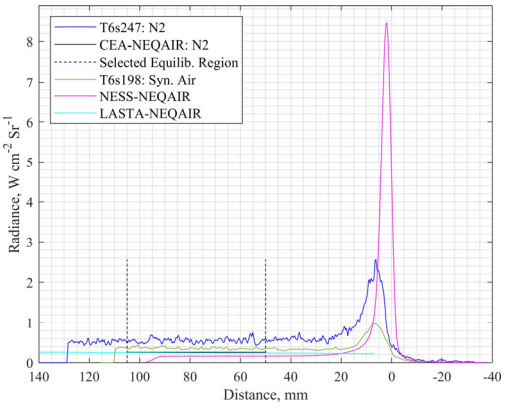

(d) T6s247 Radiance: 320-340 nm

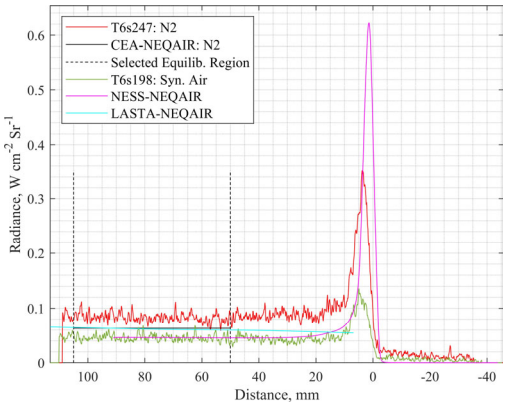

(e) T6s247 Radiance: 816-827 nm

Fig. 8 Equilibrium spectra and radiance profiles for T6s247, 6.46 km/s and 220.6 Pa fill, vs numerical predictions. Synthetic air data from T6s198, 6.55 km/s and 213.9 Pa fill, is included for comparison.

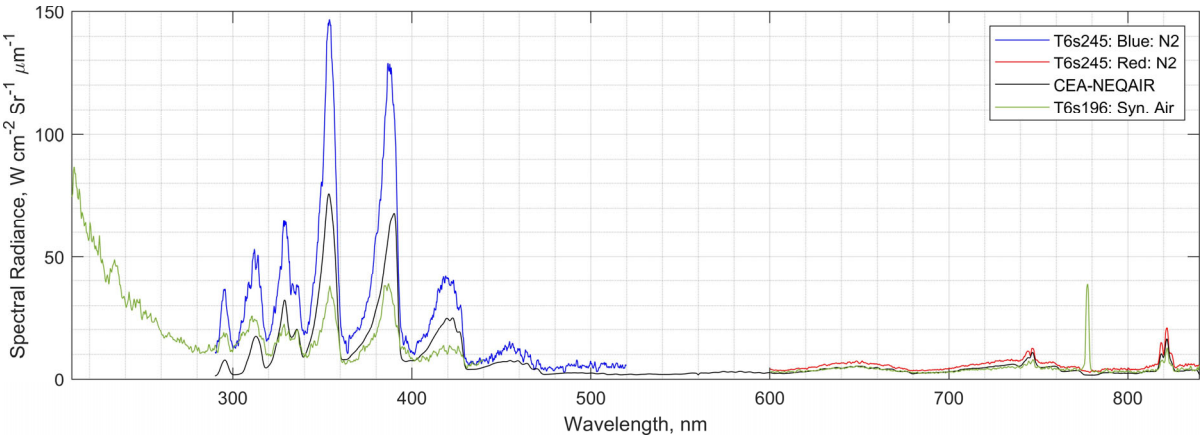

(a) T6s245: Experiment equilibrium spectra vs CEA-NEQAIR

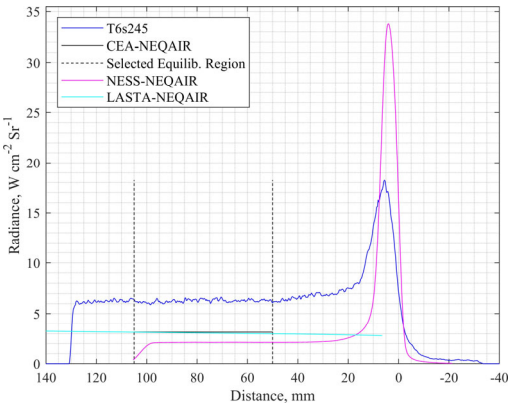

(b) T6s245 Radiance: 290-520 nm

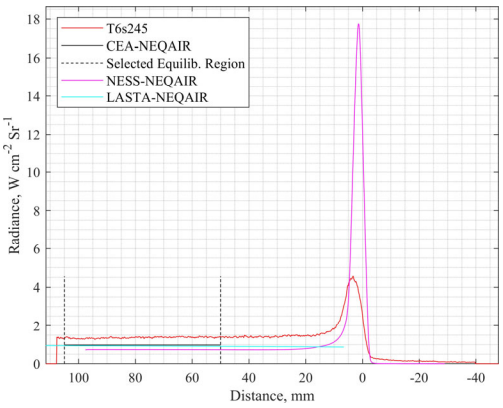

(c) T6s245 Radiance: 600-840 nm

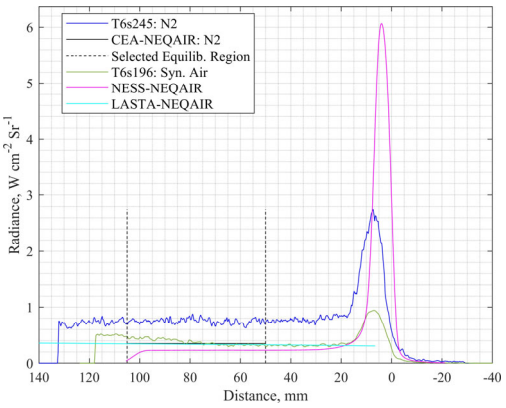

(d) T6s245 Radiance: 320-340 nm

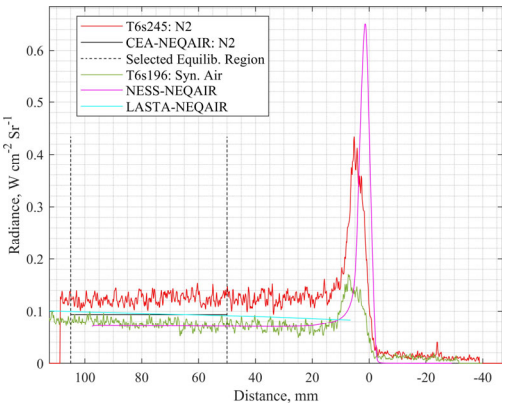

(e) T6s245 Radiance: 816-827 nm

Fig. 9 Equilibrium spectra and radiance profiles for T6s245, 6.85 km/s at window and 201.1 Pa fill, vs numerical predictions. Synthetic air data from T6s196, 6.74 km/s and 195 Pa fill, is included for comparison.

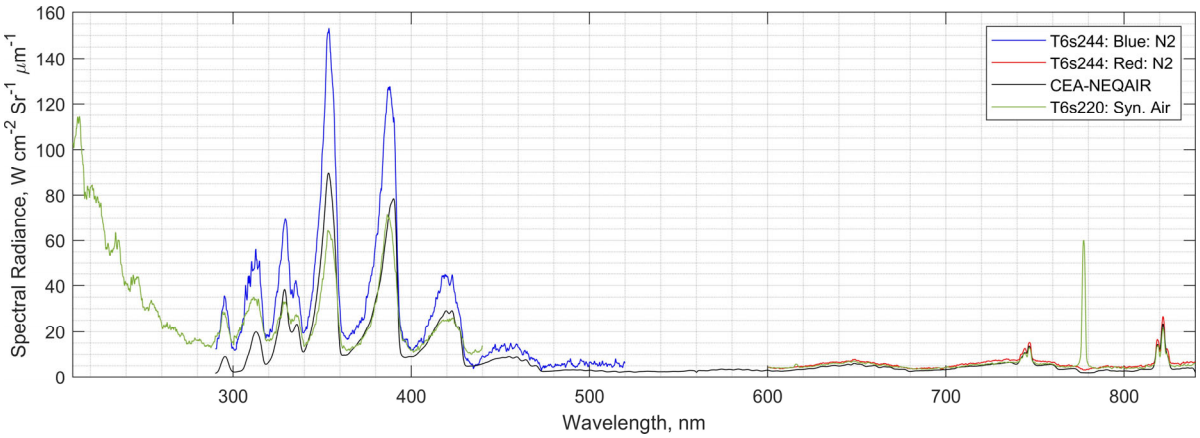

(a) T6s244: Experiment equilibrium spectra vs CEA-NEQAIR

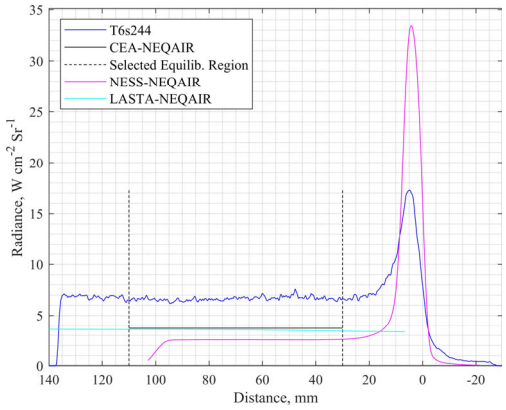

(b) T6s244 Radiance: 290-520 nm

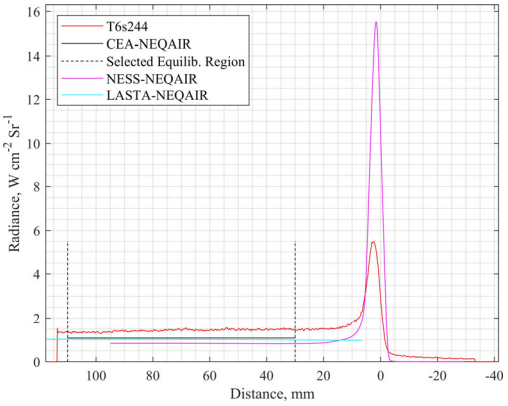

(c) T6s244 Radiance: 600-840 nm

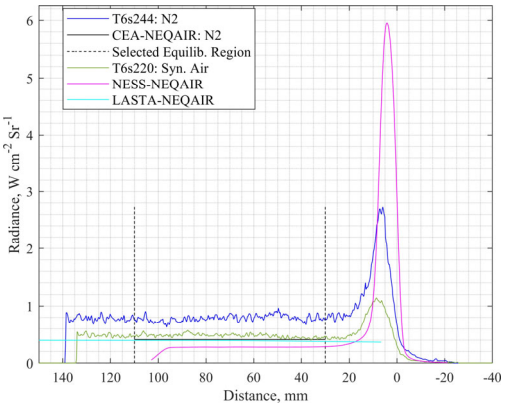

(d) T6s244 Radiance: 320-340 nm

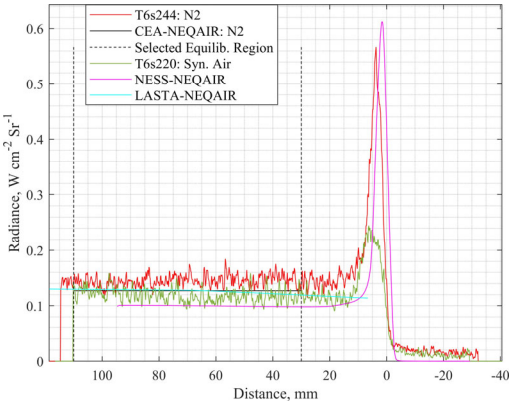

(e) T6s244 Radiance: 816-827 nm

Fig. 10 Equilibrium spectra and radiance profiles for T6s244, 7.24 km/s at window and 175 Pa fill, vs numerical predictions. Synthetic air data from T6s220, 7.12 km/s and 175 Pa fill, is included for comparison.

2. 0.5 bar Post-Shock Condition

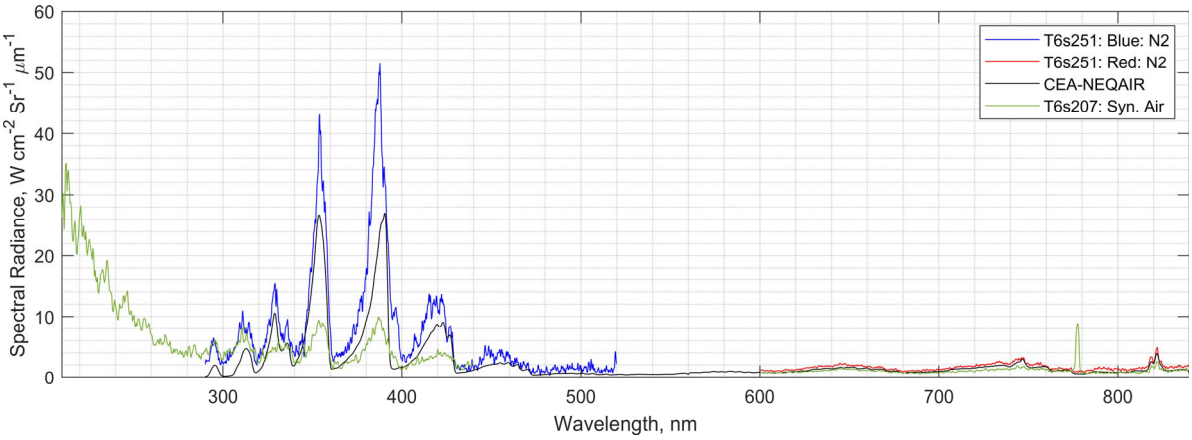

(a) T6s251: Experiment equilibrium spectra vs CEA-NEQAIR

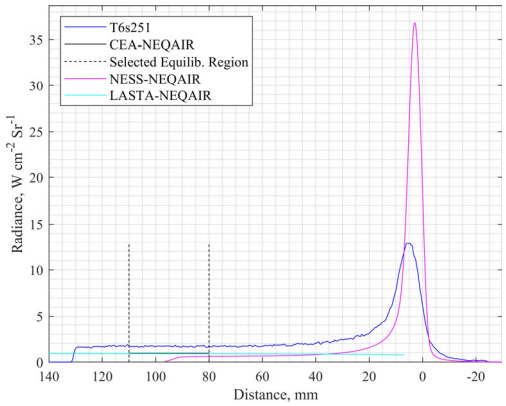

(b) T6s251 Radiance: 290-520 nm

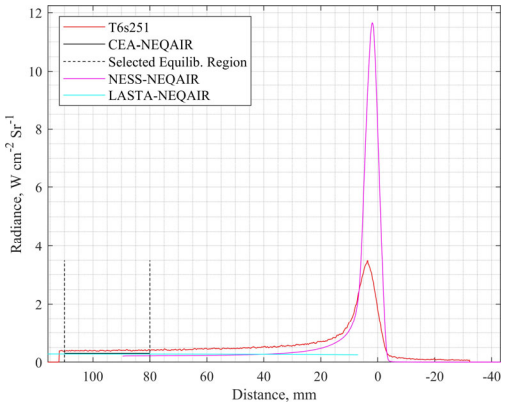

(c) T6s251 Radiance: 600-840 nm

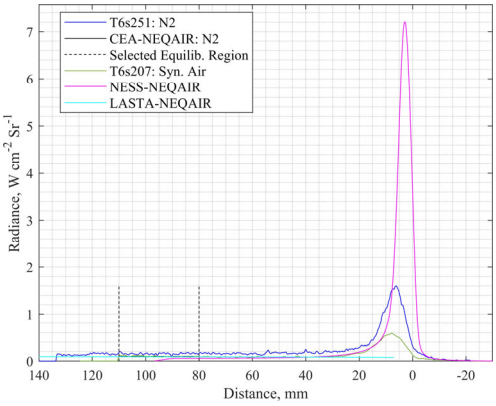

(d) T6s251 Radiance: 320-340 nm

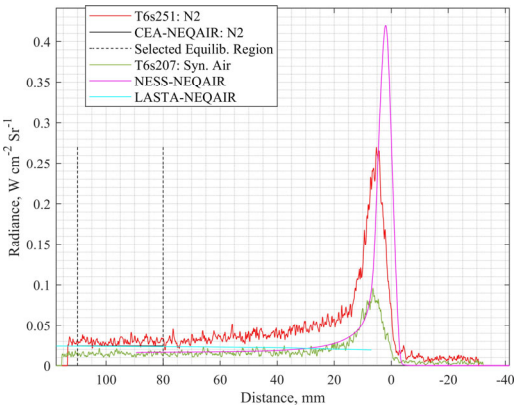

(e) T6s251 Radiance: 816-827 nm

Fig. 11 Equilibrium spectra and radiance profiles for T6s251, 6.60 km/s at window and 110.1 Pa fill, vs numerical predictions. Synthetic air data from T6s207, 6.64 km/s and 106.7 Pa fill, is included for comparison.

3. 1.5 bar Post-Shock Condition

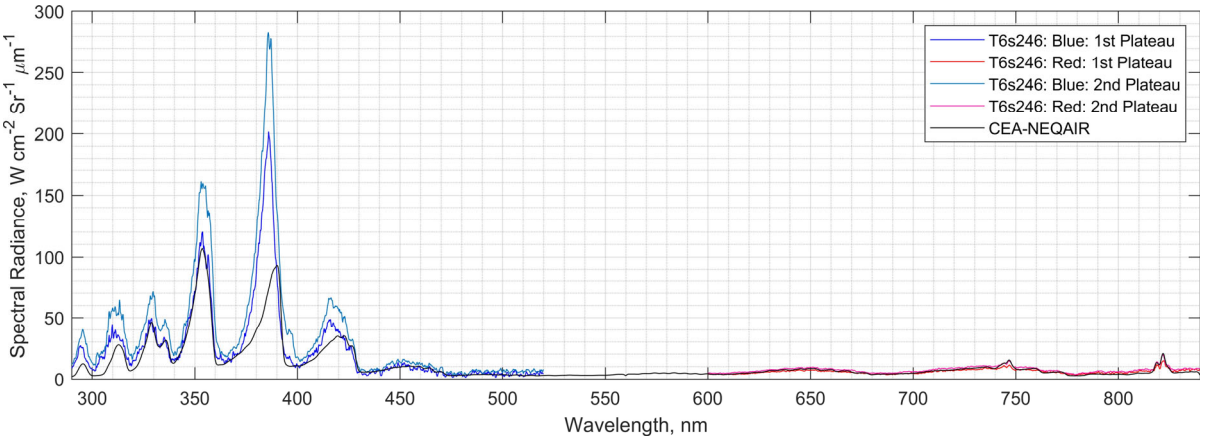

(a) T6s246: Experiment equilibrium spectra vs CEA-NEQAIR

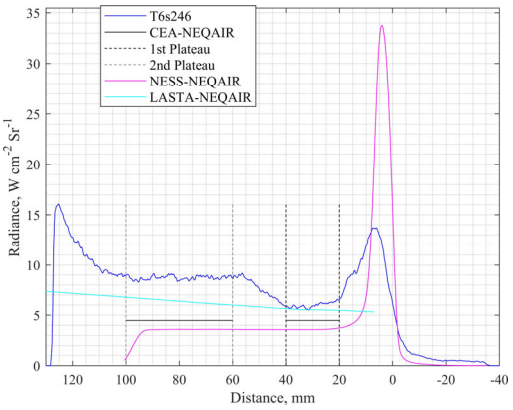

(b) T6s246 Radiance: 290-520 nm

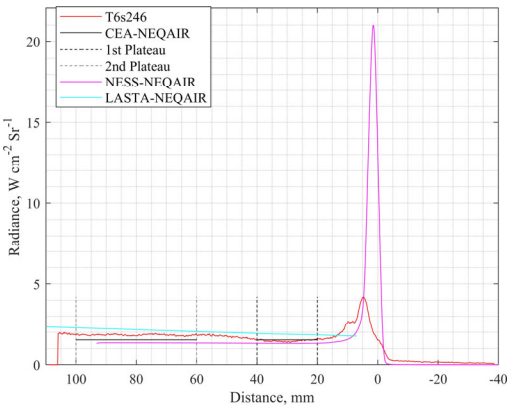

(c) T6s246 Radiance: 600-840 nm

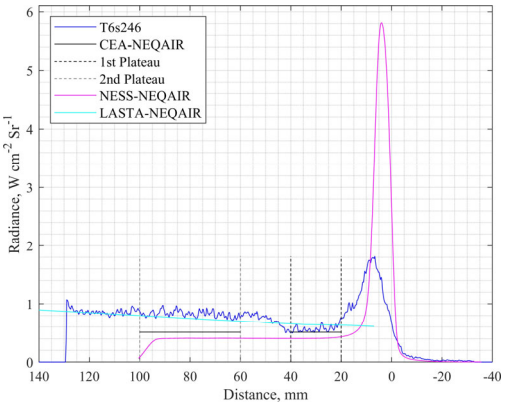

(d) T6s246 Radiance: 320-340 nm

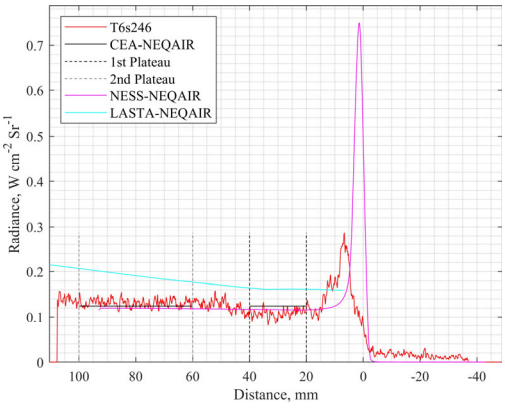

(e) T6s246 Radiance: 816-827 nm

Fig. 12 Equilibrium spectra and radiance profiles for T6s246, 6.60 km/s at window and 331.4 Pa fill, vs numerical predictions.

B. Scaled Comparison

The plots in the previous section showed the calibrated absolute spectral radiance from the pure nitrogen test conditions, as well as comparisons against synthetic air for cases where similar shock profiles were achieved. The equilibrium post-shock temperatures of the two gas mixtures are calculated to be within at least 200 K of each other for each pair of test cases. Thus, the same reaction mechanisms will be relevant for the two cases. Small differences in temperature are desirable in order to isolate the effects of adding oxygen species, and the corresponding additional reaction mechanisms, on the resulting spectra. However, one discrepancy still exists in the previous plots since the initial number of N_2 molecules in the shock tube differs between the two gas mixtures.

In this section, equilibrium spectral radiance has been re-plotted in Fig. 13 to Fig. 17 with the pure nitrogen data multiplied by 0.7922, corresponding to the mole fraction of N_2 molecules in the synthetic air mixture used. This scales the measured spectral radiance to approximate if each gas mixture started with the same number of N_2 molecules, before being processed by the shock. It relies on the assumption of an optically thin post-shock test gas. This was validated for the equilibrium composition by comparing the NEQAIR optically thin and optically thick predictions for the two fastest cases, T6s220 and T6s244. Plots for for this are summarised in Fig. 18. In the worst case, NEQAIR predicts a drop of 3.16% in final cumulative radiance in the Vis/NIR region of T6s220 in synthetic air, 7.21 km/s and 175 Pa fill, largely due to absorption of the 777 nm atomic oxygen line. The lower speed cases should have even less absorption, and thus the optically thin assumption is taken to be valid for all test cases.

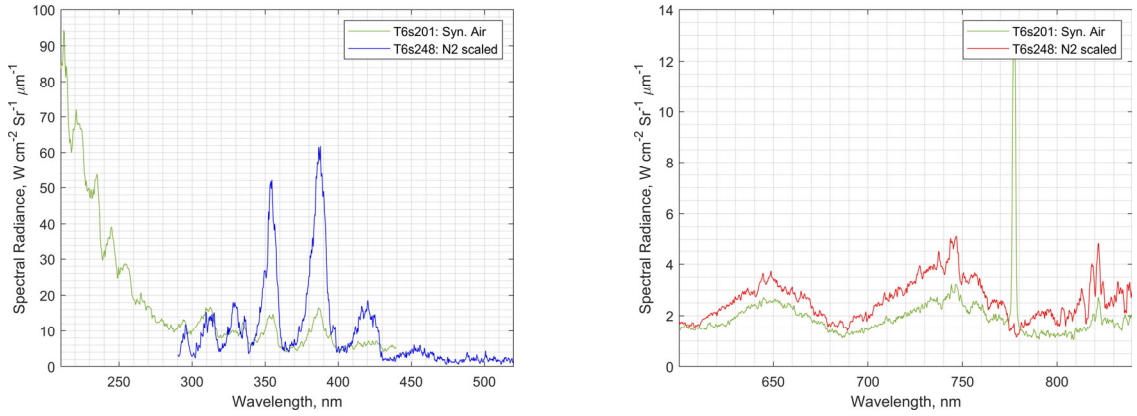

(a) 210-520 nm **(b) 600-840 nm**

Fig. 13 Equilibrium spectra of synthetic air T6s201, 5.97 km/s and 261.2 Pa fill, vs pure nitrogen T6s248, 5.92 km/s and 269.58 Pa fill, multiplied by N_2 mole fraction of the synthetic air mixture.

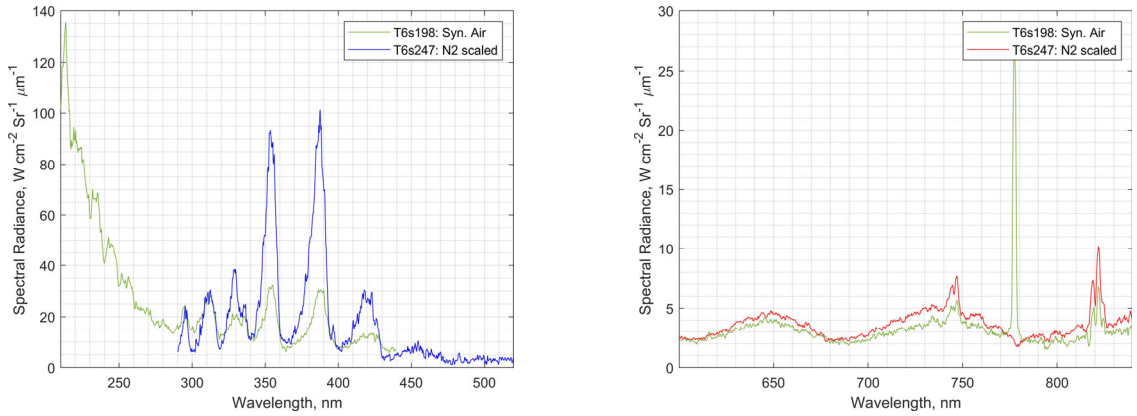

(a) 210-520 nm **(b) 600-840 nm**

Fig. 14 Equilibrium spectra of synthetic air T6s198, 6.58 km/s and 213.9 Pa fill, vs pure nitrogen T6s247, 6.54 km/s and 220.58 Pa fill, multiplied by N_2 mole fraction of the synthetic air mixture.

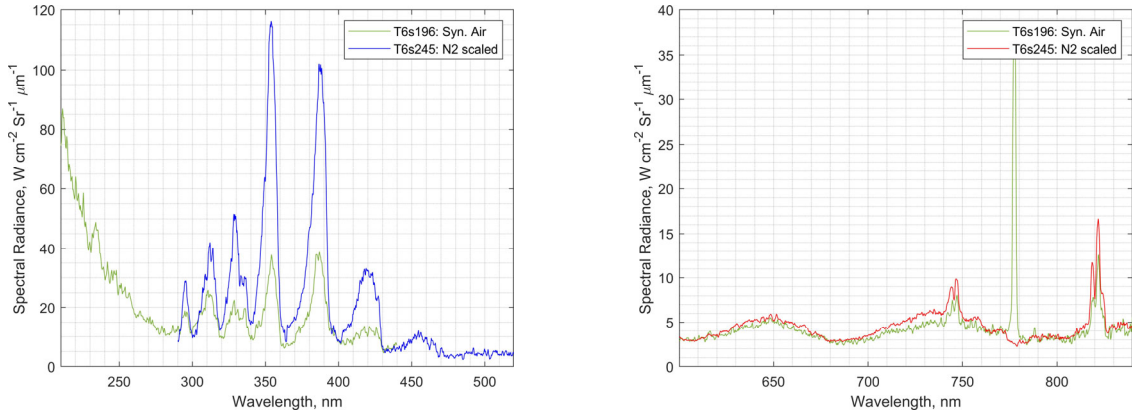

(a) 210-520 nm **(b) 600-840 nm**

Fig. 15 Equilibrium spectra of synthetic air T6s196, 6.87 km/s and 195.0 Pa fill, vs pure nitrogen T6s245, 6.91 km/s and 201.06 Pa fill, multiplied by N_2 mole fraction of the synthetic air mixture.

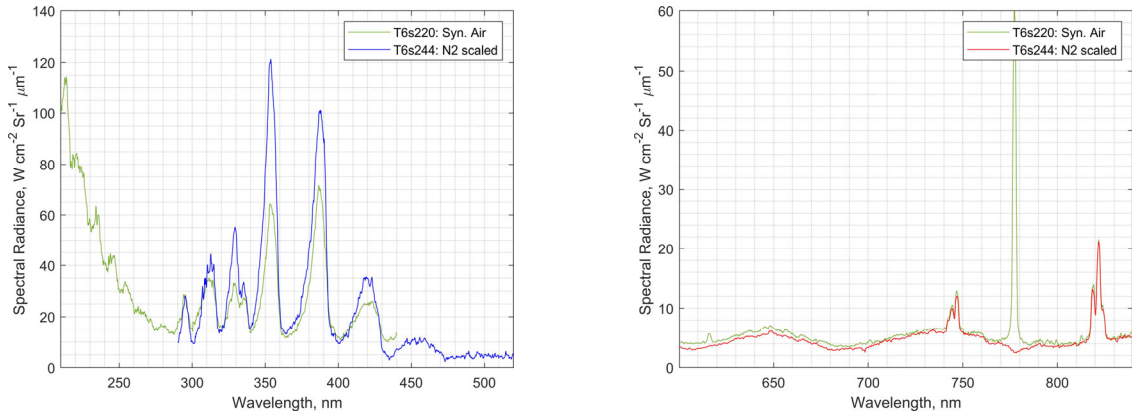

(a) 210-520 nm **(b) 600-840 nm**

Fig. 16 Equilibrium spectra of synthetic air T6s220, 7.21 km/s and 175.0 Pa fill, vs pure nitrogen T6s244, 7.24 km/s and 175.0 Pa fill, multiplied by N_2 mole fraction of the synthetic air mixture.

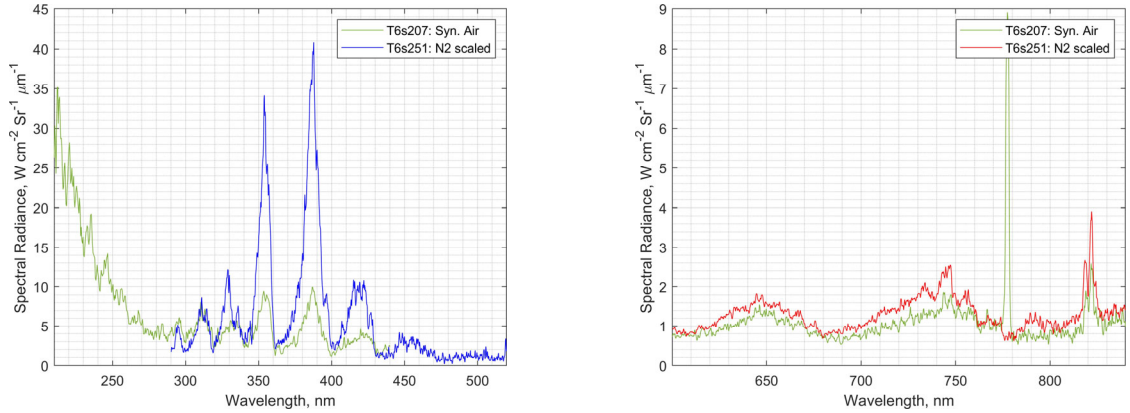

(a) 210-520 nm **(b) 600-840 nm**

Fig. 17 Equilibrium spectra of synthetic air T6s207, 6.64 km/s and 106.75 Pa fill, vs pure nitrogen T6s251, 6.71 km/s and 110.1 Pa fill, multiplied by N_2 mole fraction of the synthetic air mixture.

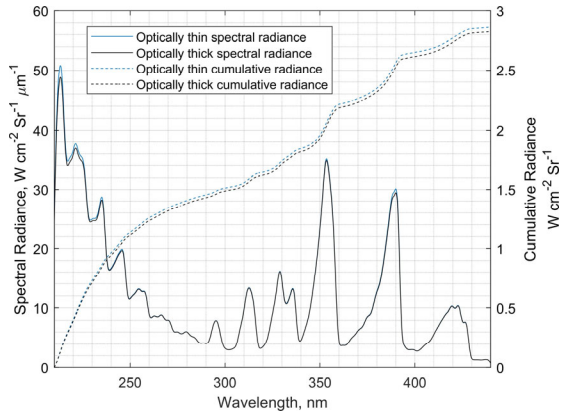

(a) T6s220 Blue: 98.71%

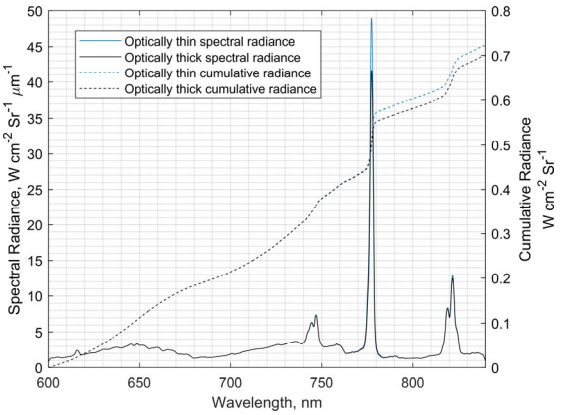

(b) T6s220 Red: 96.84%

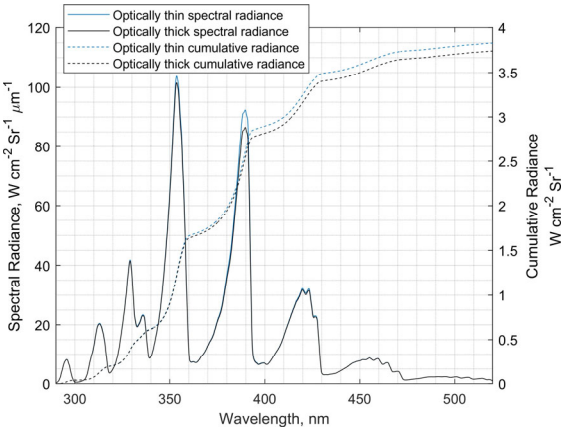

(c) T6s244 Blue: 97.68%

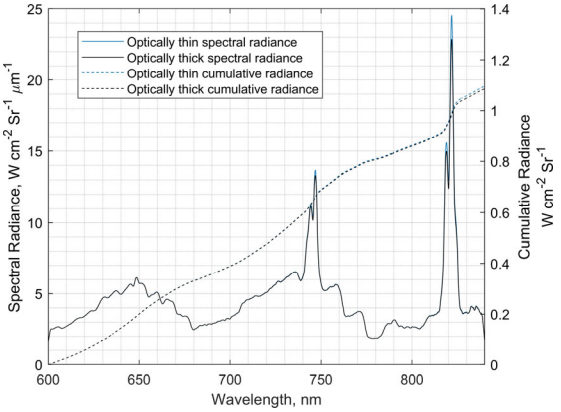

(d) T6s244 Red: 99.11%

Fig. 18 Comparison of CEA-NEQAIR predictions with and without absorption for fastest synthetic air and pure nitrogen test cases, T6s220 and T6s244. Spectra have been convolved with experimentally measured instrument line shapes. The percentage of final thin cumulative radiance compared to final thick cumulative radiance is stated underneath each figure, relevant to the wavelength region plotted.

VI. Discussion

One of the most noticeable discrepancies between the experimental data and numerical predictions, is the offset in equilibrium radiance present across all wavelengths in both pure nitrogen and synthetic air gas mixtures. LASTA-NEQAIR simulations confirm that this is not a result of shock deceleration effects, as would be expected since the shock speed profiles are relatively flat. Trials of different stray light removal techniques have also been tried and although provide some means to bring the equilibrium radiance closer to numerical predictions, it is not enough to account for the offset seen. There is also no strong argument for the alternative methods being correct over the standard pedestal removal technique, thus only the results from the standard stray light calibration methodology, as in [1], have been implemented in this paper. For now, the offset remains a subject for future investigation, and possibly owed to contaminants present on the tunnel walls, the boundary layer's influence on radiation, and/or excess electron number densities. The closest agreement of experiment to CEA- or LASTA-NEQAIR predictions is in the equilibrium region of the spatial radiance profile from 816 to 827 nm. This is expected since the background offset decreases at higher wavelengths and strong atomic nitrogen lines are present in this region.

The following discussion analyses radiation emission from individual species and the N_2 first positive band system. Figure 19 is a summary of these relevant radiating nitrogen species, from a CEA-NEQAIR simulation of T6s244, 7.24 km/s and 175 Pa fill of pure nitrogen. The N_2 first positive band is referred to separately and so is plotted independently of the overall N_2 spectrum. Radiation from N^+ is five orders of magnitude less than any of the other species and so has not been included.

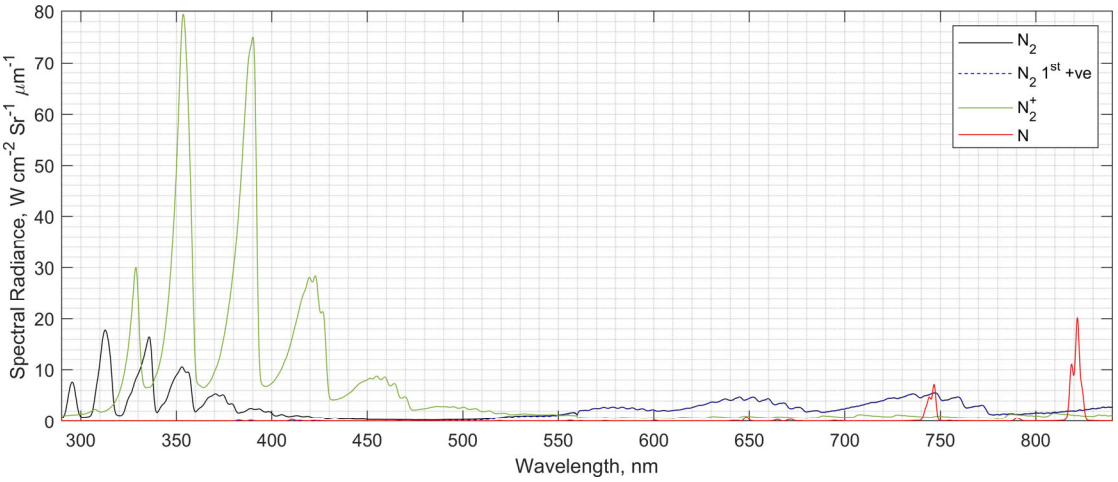

Fig. 19 CEA-NEQAIR spectral radiance predictions for radiating species (and N_2 first positive band) of T6s244. For an optically thin medium, the overall spectrum is a superposition of these constituent species.

Plots of absolute equilibrium spectral radiance for pure nitrogen in Fig. 7 to Fig. 11, show the radiation from molecular and atomic nitrogen species exceeds that from the equivalent synthetic air condition. This is in part due to the higher number of N_2 molecules in the shock tube to start with. The effect of which is removed in Fig. 13 to Fig. 17 by multiplying the pure nitrogen spectral radiance by the mole fraction of N_2 in the synthetic air mixture used.

In the Vis/NIR region, the N_2 first positive band radiance in the pure nitrogen data is elevated over the synthetic air data, but this decreases with shock speed. At 7.2 km/s, Fig. 16, the presence of oxygen species appears to have no effect on the radiation from the N_2 first positive band. Similar can be said of the atomic nitrogen peaks at 745 and 822 nm. By 7.2 km/s, the synthetic air and scaled pure nitrogen data practically overlap, the only difference being the atomic oxygen line present at 777 nm in the synthetic air spectrum. This suggests the presence of oxygen species, and additional reaction mechanisms that come with it, becomes more negligible at higher shock speeds. This can be explained since the two main species introduced by addition of oxygen, that contain both N and O atoms are NO and NO^+. Both of which begin to dissociate rapidly at around 7000 K (7 km/s) to give independent N and O atoms. Thus, at these higher temperatures, where NO is rapidly depleted and production of atomic species is promoted, the chemistry of oxygen and nitrogen species become more independent of each other, explaining the close overlap in the Vis/NIR region of T6s244 and T6s220.

In contrast, in the UV/Vis region, it is evident that radiation from the N_2 and N_2^+ bands from 320 to 440 nm, is significantly higher in the scaled nitrogen data than the synthetic air, at all shock speeds. This is a more intuitive result, as more molecular nitrogen species and ions should be present when they are not being consumed by alternative reaction mechanisms when in the presence of oxygen. Additionally, dissociation of N_2 and N_2^+ will not likely occur as fast as NO due to the presence of a triple bond. Hence, there is still a significant discrepancy between the pure nitrogen and synthetic air data even at higher shock speeds. It is possible at 7.2 km/s the N_2 and N_2^+ radiation in synthetic air begins to catch up with that seen in pure nitrogen, however is not as convincing as seen in the Vis/NIR region. Continued comparisons at higher shock speeds would be beneficial to see if this trend continues. At lower wavelengths, the synthetic air data is superimposed with radiation originating from NO species and thus exceeds the pure nitrogen case. It's also interesting to note the background radiation between the bands is often at the same level for both the synthetic air and scaled nitrogen data. This potentially supports the theory of the excess background equilibrium radiation originating due to physical phenomena in the test gas, and not artifacts of the calibration process such as stray light removal.

Results from the NESS-NEQAIR simulation of the pure nitrogen test cases generally significantly over-predict radiation in the non-equilibrium region, and relax to an equilibrium radiance below that of both experiment and CEA or LASTA predictions. That said, the size of the NESS non-equilibrium regions and relaxation profile is close to that seen in the experiments. This suggests the rate of vibrational relaxation used in the NESS simulations is close to reality, even if off in magnitude. Since the excess non-equilibrium region is a global occurrence across all wavelengths, it suggests an over-prediction in the magnitude of, possibly both, the trans-rotational and vibro-electronic temperatures. Investigation of the line of sight files generated by NESS and CEA show the final NESS temperatures to consistently be 150 K below that predicted by CEA, hence contributing to the lower final equilibrium radiance. This is supported by the final number densities of the NESS predictions being very close to that of CEA, thus suggesting the offsets seen in the NESS-NEQAIR results is owed to the absolute temperature values calculated. There is mildly better agreement of the NESS-NEQAIR non-equilibrium region with the experimental data at higher shock speeds, though still a considerable difference. Best agreement is seen in radiation from the atomic nitrogen species, shown in the spatial radiance profiles integrated over 816 to 827 nm.

VII. Conclusion

Equilibrium and non-equilibrium absolute spectral radiance data of pure nitrogen at shocks speeds from 5.45 to 7.24 km/s, attained from the Oxford T6 Stalker Tunnel operating in Aluminium Shock Tube mode, have been presented. CEA- and LASTA-NEQAIR simulations show the experiment to have an enhanced equilibrium radiance across all wavelengths, increasing towards the lower wavelengths. The reason for this is speculated as contaminants on the walls, high temperature boundary layer, and/or excess electrons, and is to be investigated in further work. NESS-NEQAIR predictions indicate the absolute values of the trans-rotational and vibro-electronic temperatures to be over-predicted in the non-equilibrium region and under-predicted in the final state after relaxation. Although, the size of the non-equilibrium region predicted, and thus vibrational relaxation rate, is in close agreement with the experimental data. Comparisons of synthetic air data against pure nitrogen data scaled by the N_2 mole fraction of the synthetic air mixture have been made. These reveal that the addition of oxygen species becomes more negligible to the chemistry of nitrogen-only mechanisms as shock speed increases. This is related to the rapid dissociation of NO and NO^+ species from around 7 km/s, and increase of independent N and O atoms. Future work to see if this trend continues at higher shock speeds is recommended, though the optically thin assumption will become less valid, to see if the UV/Vis region follows this trend as N_2 and N_2^+ species also dissociate at higher temperatures.

Appendix: N2 vs Synthetic Air Shock Profiles

This section is used to compare the pure nitrogen and synthetic air shock profiles, to aid the analysis of spectra and radiance profiles from Fig. 6 to Fig. 17. Solid lines between data points are included to improve plot readability, not to indicate linear variations in shock speed.

A. T6s248 vs T6s201

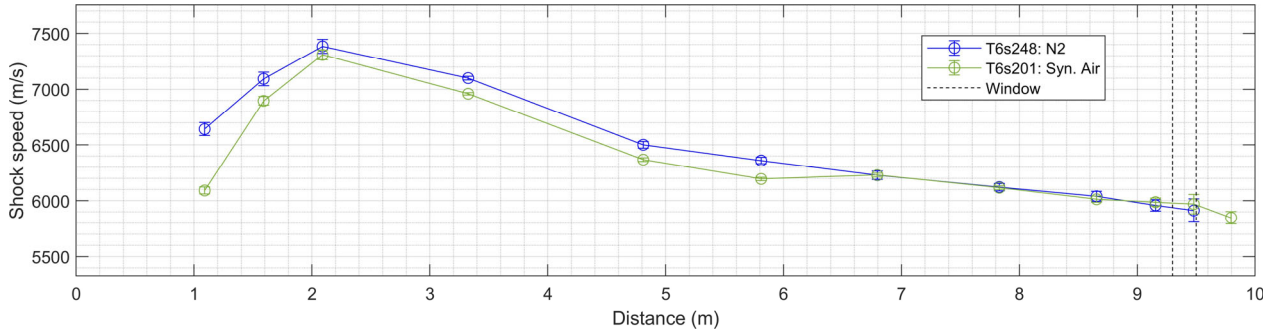

Fig. 20 Shock speed profiles of pure nitrogen T6s248 and synthetic air T6s201 against distance from the primary diaphragm.

B. T6s247 vs T6s198

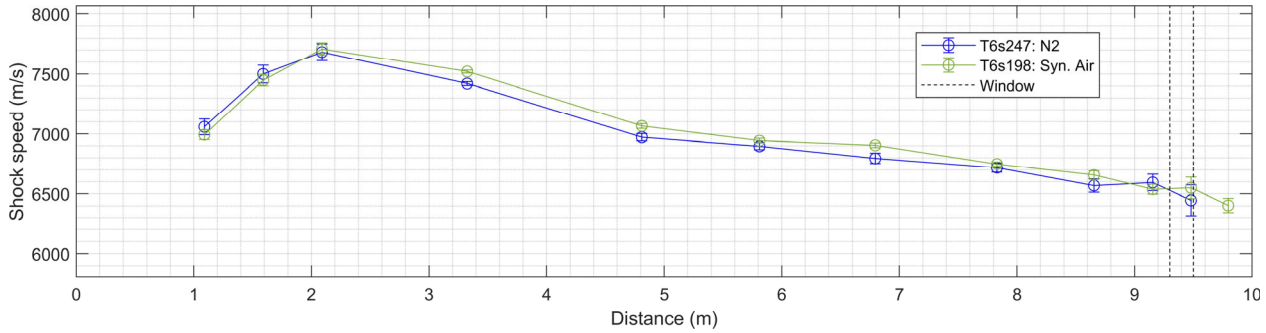

Fig. 21 Shock speed profiles of pure nitrogen T6s247 and synthetic air T6s198 against distance from the primary diaphragm.

C. T6s245 vs T6s196

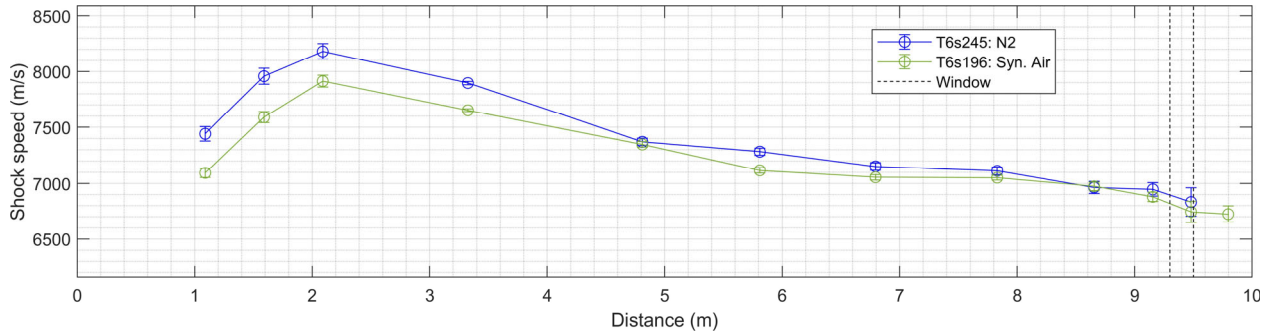

Fig. 22 Shock speed profiles of pure nitrogen T6s245 and synthetic air T6s196 against distance from the primary diaphragm.

D. T6s244 vs T6s220

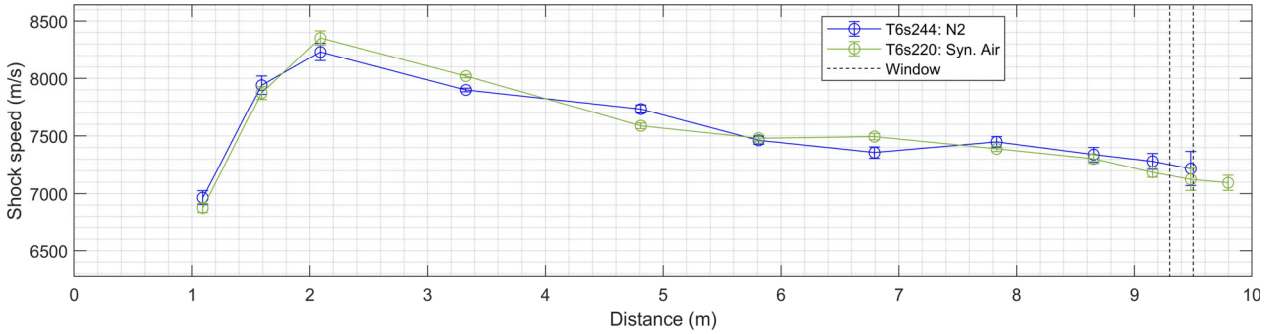

Fig. 23 Shock speed profiles of pure nitrogen T6s244 and synthetic air T6s220 against distance from the primary diaphragm.

E. T6s251 vs T6s207

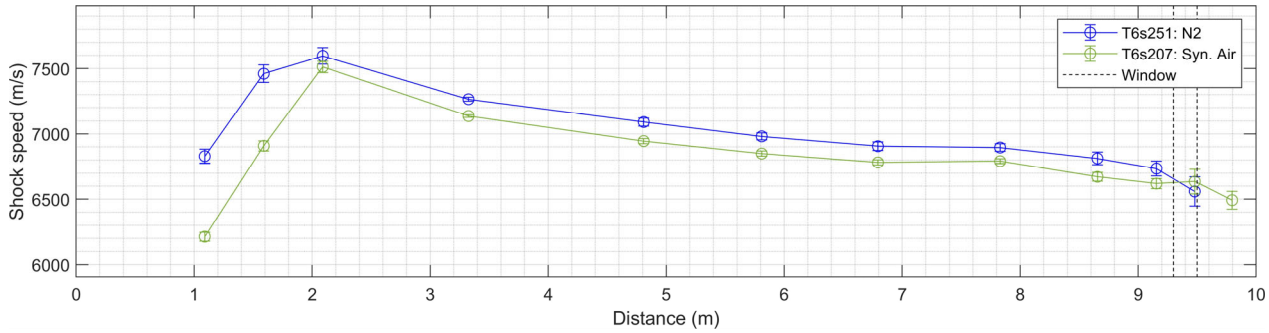

Fig. 24 Shock speed profiles of pure nitrogen T6s251 and synthetic air T6s207 against distance from the primary diaphragm.

Acknowledgments

The test campaign to gather data for this paper was funded by AFOSR/EOARD grant FA9550-19-1-7020. The authors express their gratitude for making this work possible. The authors would also like to thank Brett Cruden and Aaron Brandis at NASA Ames Research Center for their guidance on work throughout the project and for the loan of equipment, in particular the McPherson 218 spectrometer, Princeton Instruments PI-MAX2 camera and deuterium calibration lamp.

References

[1] Cruden, B. A., "Absolute radiation measurements in earth and mars entry conditions," 2014.

[2] Laux, C. O., Spence, T., Kruger, C., and Zare, R., "Optical diagnostics of atmospheric pressure air plasmas," *Plasma Sources Science and Technology*, Vol. 12, No. 2, 2003, p. 125.

[3] Collen, P., "Development of a High-Enthalpy Ground Test Facility for Shock-Layer Radiation," Ph.D. thesis, Univ. of Oxford, Oxford, UK, 2021.

[4] Collen, P., Doherty, L. J., Subiah, S. D., Sopek, T., Jahn, I., Gildfind, D., Penty Geraets, R., Gollan, R., Hambidge, C., Morgan, R., et al., "Development and commissioning of the T6 Stalker Tunnel," *Experiments in Fluids*, Vol. 62, No. 11, 2021, pp. 1–24.

[5] McGilvray, M., Collen, P., Doherty, L., Steer, J., Leader, J., Glenn, A., and Hambidge, C., "The Oxford T6 Stalker tunnel: performance, upgrades and new modes of operation," 2022.

[6] Glenn, A. B., Collen, P. L., and McGilvray, M., "Experimental Non-Equilibrium Radiation Measurements for Low-Earth Orbit Return," 2021.

[7] Steer, J., Collen, P. L., Glenn, A. B., Hambidge, C., Doherty, L. J., McGilvray, M., Loehle, S., and Walpot, L., "Shock Radiation Tests for Ice Giant Entry Probes Including CH4 in the T6 Free-Piston Driven Wind Tunnel," *AIAA SCITECH 2023 Forum*, 2023, p. 1729.

[8] Collen, P. L., Glenn, A. B., Doherty, L. J., and McGilvray, M., "Absolute Measurements of Air Shock-Layer Radiation in the T6 Aluminium Shock Tube," *Journal of Thermophysics and Heat Transfer*, 2023, pp. 1–14.

[9] Park, C., "Review of chemical-kinetic problems of future NASA missions. I-Earth entries," *Journal of Thermophysics and Heat transfer*, Vol. 7, No. 3, 1993, pp. 385–398.

[10] Brandis, A., Johnston, C., Cruden, B., Prabhu, D., and Bose, D., "Uncertainty analysis and validation of radiation measurements for earth reentry," *Journal of Thermophysics and Heat Transfer*, Vol. 29, No. 2, 2015, pp. 209–221.

[11] Brandis, A. M., Johnston, C. O., and Cruden, B. A., "Investigation of Non-Equilibrium Radiation for Earth Entry," 2016.

[12] Brandis, A., Johnston, C., Cruden, B., and Prabhu, D., "Equilibrium radiative heating from 9.5 to 15.5 km/s for earth atmospheric entry," *Journal of Thermophysics and Heat Transfer*, Vol. 31, No. 1, 2017, pp. 178–192.

[13] Cruden, B. A., and Brandis, A. M., "Measurement and prediction of radiative non-equilibrium for air shocks between 7-9 km/s," 2017.

[14] Gnoffo, P. A., Weilmuenster, K. J., Hamilton, H. H., Olynick, D. R., and Venkatapathy, E., "Computational aerothermodynamic design issues for hypersonic vehicles," *Journal of Spacecraft and Rockets*, Vol. 36, No. 1, 1999, pp. 21–43.

[15] Brandis, A. M., and Cruden, B. A., "Shock tube radiation measurements in nitrogen," *2018 Joint Thermophysics and Heat Transfer Conference*, 2018, p. 3437.

[16] Cruden, B. A., and Brandis, A. M., "Analysis of shockwave radiation data in nitrogen," *AIAA Aviation 2019 Forum*, 2019, p. 3359.

[17] Tibère-Inglesse, A. C., McGuire, S. D., Mariotto, P., and Laux, C. O., "Validation cases for recombining nitrogen and air plasmas," *Plasma Sources Science and Technology*, Vol. 27, No. 11, 2018, p. 115010.

[18] Panesi, M., Munafò, A., Magin, T., and Jaffe, R., "Nonequilibrium shock-heated nitrogen flows using a rovibrational state-to-state method," *Physical Review E*, Vol. 90, No. 1, 2014, p. 013009.

[19] Grover, M. S., Singh, N., Schwartzentruber, T. E., and Jaffe, R. L., "Dissociation and internal excitation of molecular nitrogen due to N2-N collisions using direct molecular simulation," *55th AIAA Aerospace Sciences Meeting*, 2017, p. 0660.

[20] Macdonald, R. L., Torres, E., Schwartzentruber, T. E., and Panesi, M., "State-to-state and direct molecular simulation study of energy transfer and dissociation of nitrogen mixtures," *AIAA Scitech 2020 Forum*, 2020, p. 1712.

[21] Jaffe, R. L., Grover, M., Venturi, S., Schwenke, D. W., Valentini, P., Schwartzentruber, T. E., and Panesi, M., "Comparison of potential energy surface and computed rate coefficients for N 2 dissociation," *Journal of thermophysics and heat transfer*, Vol. 32, No. 4, 2018, pp. 869–881.

[22] Satchell, M., McGilvray, M., and Di Mare, L., "Analytical Method of Evaluating Nonuniformities in Shock Tube Flows: Theory and Development," *AIAA Journal*, 2021, pp. 1–15.

[23] Satchell, M., Glenn, A., Collen, P., Penty-Garaets, R., McGilvray, M., and di Mare, L., "An Analytical Method of Evaluating Nonuniformities in Shock Tube Flows. Part 2: Application," 2021.

[24] Clarke, J., Collen, P. L., McGilvray, M., and di Mare, L., "Numerical Simulation of a Shock Tube in Thermochemical Non-Equilibrium," *AIAA SCITECH 2023 Forum*, 2023, p. 1797.

[25] Gildfind, D. E., James, C. M., Toniato, P., and Morgan, R. G., "Performance considerations for expansion tube operation with a shock-heated secondary driver," *Journal of Fluid Mechanics*, Vol. 777, 2015, pp. 364–407.

[26] Collen, P. L., Satchell, M., di Mare, L., and McGilvray, M., "Analysis of Shock Deceleration Effects on Radiation Experiments in the NASA Electric Arc Shock Tube," *AIAA SCITECH 2022 Forum*, 2022, p. 0267.

[27] Mirels, H., "Test time in low-pressure shock tubes," *The physics of Fluids*, Vol. 6, No. 9, 1963, pp. 1201–1214.

[28] McBride, B. J., *Computer program for calculation of complex chemical equilibrium compositions and applications*, Vol. 2, NASA Lewis Research Center, 1996.

[29] Cruden, B. A., and Brandis, A. M., "Updates to the NEQAIR radiation solver," *6th International Workshop on Radiation of High Temperature Gases in Atmospheric Entry*, 2014.

[30] Whiting, E. E., Park, C., Liu, Y., Arnold, J. O., and Paterson, J. A., "NEQAIR96, Nonequilibrium and Equilibrium Radiative Transport and Spectra Program: User's Manual," 1996.

Conclusion

Absolute radiation measurements relevant to Low Earth Orbit return trajectories have been made is synthetic air and pure nitrogen gas mixtures, from 5.4 to 7.2 km/s, in the Oxford T6 Stalker Tunnel while operating in Aluminium Shock Tube mode. Equilibrium spectral radiance profiles in both the ultraviolet/visible region and visible/near infrared exceed predictions from CEA- and LASTA-NEQAIR numerical tools. This was present in both gas mixtures and has been identified to not be a result of stray light during the calibrations, nor shock deceleration effects. Remaining theories include contaminants from the tunnel wall, high temperature boundary layer effects, and excess electron number densities, potentially originating from the two former effects. The discrepancy between experiment and simulation was also seen for the test conditions when repeated in the Electric Arc Shock Tube at NASA Ames. Investigation into the origin of the offset in equilibrium spectral radiance is recommended as further work.

Non-equilibrium radiance profiles and metrics have been compared to numerical predictions, using POSHAX and newly developed NESS one-dimensional chemical kinetic solvers, using a variety of chemical rate models. An initial comparison with Park, Huo and Cruden rates shows simulations of the non-equilibrium radiance can be out by up to 76.2% for the nominal synthetic air test case (6.55 km/s, 213.9 Pa fill). This demonstrates the use of the data to extract new rates by further analysis. The offset from the equilibrium region however is likely still present in the non-equilibrium region and will thus complicate the comparison.

Scaling the pure nitrogen data by the mole fraction of N_2 in the synthetic air mixture reveals the influence of oxygen species on the chemistry of nitrogen species to be more important at lower shock speeds. This is due to the higher concentration of NO and NO+ at lower post-shock temperatures, before their dissociation is really promoted. Since NO is a strong radiator in air at these speeds, the resulting total radiance emitted is largely dominated by NO, as well as other molecular species – N_2 and N_2+.

Future work to extend test cases for a broader range of shock speeds and oxygen percentages will reveal if these trends continue, and improve understanding of the role oxygen species play in the shock layer for a Low Earth Orbit return mission.

Acknowledgement

The authors would like to thank the US Air Force for the funding to carry out these experiments via grant FA9550-19-1-7020. As well as their input during the data gathering and analysis.